Title	n型 テルル化鉛-テルル化錫混晶におけるシュブニコフード・ハース効果の研究
Author(s)	高藤, 裕
Citation	大阪大学, 1977, 博士論文
Version Type	VoR
URL	https://hdl.handle.net/11094/1674
rights	
Note	

STUDY ON SHUBNIKOV-DE HAAS EFFECT
IN
N-TYPE $Pb_{1-x}Sn_xTe$ ALLOYS

Yutaka TAKAFUJI

February 1977

Acknowledgements

The author wishes to express his sincere thanks to Professor S. Narita for suggesting this investigation as well as for his continual guidance and encouragement. He would also like to thank to Dr.R.S.Kim for his helpful discussions, and to Mr.Y. Ogawa, Mr. M. Murata, Mr.H. Takada, and to Mr.Y. Tazaki for their assistance in preparing the materials.
Thanks are extended to the members of the laboratory of Prof. Narita for their useful discussions.

He is also indebted to Professor T. Okamoto of Institute of Scientific and Industrial Research, Osaka University, Mr. K. Adachi of Government Industrial Research Institute, Osaka, and Mr. T. Okumura of Japan Electron Optics Laboratory Co., Ltd., for giving him the facilities for the measurements of SnTe-composition.

Abstract

A detailed experimental study on the Shubnikov-de Haas effect of n-type $Pb_{1-x}Sn_xTe$ alloys of x=0 - 0.28 has been made in the temperature range of 1.34 - 4.2 K, using the samples with relatively low carrier concentrations ($n{\sim}10^{16}$- 10^{17} cm^{-3}) prepared by a solution growth method.

The angular dependences of the period of the oscillation are measured for the study of the shape of the Fermi surface. The results indicate that the Fermi surfaces are four prolate [111] ellipsoids whose anisotropy increases with decreasing band gap.

The effective masses and the effective g-values (or the spin splittig factor) of the conduction band have been also obtained as a function of alloy composition. These results are similar to those obtained by Nii, and Melngailis et al. for the p-type materials. The analysis by the two-band non-parabolic model, similar to that presented by Cohen and Blount for Bi, gives the transverse momentum matrix element $4P_{\perp}^2=0.58(1+0.211x)^2$ (au.), and the longitudinal momentum matrix element $4P_{\parallel}^2=0.046(1-0.142x)^2$ (au.), and the energy gap $E_G=183(1-0.35/x)$ meV. These parameters give the fair agreement with the present experimental results.

The spin effects on the oscillatory magnetoresistance have also been studied. The spin effect observed in the transverse and the longitudinal magnetoresistance in $\vec{H}$ // [100] are quite different. In the spin effects, the most striking behavior in the longitudinal magnetoresistance is the complete missing of the corresponding highest field oscillatory peak to the transverse one. This result is in contrast to the well known feature of other several narrow gap materials such as InSb and $Hg_{1-x}Cd_xTe$ in which the two highest field peaks are missing in the longitudinal magnetoresistance.

Above anomalous feature of the longitudinal magnetoresistance is well

interpreted in terms of the selection rules from the spin-flip scattering due to the spin-orbit interaction in the free electron picture which have been taken into account in the study on the Shubnikov-de Haas effect of $Hg_{1-x}Cd_xTe$ by Suizu and Narita. From the analysis, we have concluded that the spin splitting is smaller than the Landau level separation for the samples studied (PbTe-side composition of the crossover). We have also assigned the oscillatory peaks basing on the above conclusion. In this assignment, the features of the transverse and longitudinal magnetoresistances are as follows: both the H_N^- and H_N^+ series of oscillatory peaks are observed in the transverse magnetoresistance though the intensity of the H_N^+ peaks are weak, whereas in the longitudinal one the H_N^+ series including the H_0^+ peak are missing though the H_N^- series are observed.

It is finally concluded that the transitions due to the spin-flip scattering by non-magnetic impurity potential in the band electron picture have also well interpreted the present experimental results.

Contents

I. Introduction

I.1. Historical Survey of Studies on Shubnikov-de Haas Effect

Quantum oscillations in the magnetoresistance were first reported for bismuth crystal by Shubnikov and de Haas[1)] in 1930. This work was followed by a discovery of the oscillatory behavior of the magnetic susceptibility by de Haas and van Alphen[2)] in 1933 also in bismuth. The oscillatory magnetoresistance as well as the susceptibility oscillation known as the de Haas-van Alphen effect was accepted with a sensation at that time. Especially the report of the susceptibility oscillation caused a strong surprise, because it violated the accepted principle predicted by the classical theory that the free electron should not exhibit the diamagnetism.

The theory of the oscillatory susceptibility was first provided by Landau[3)] and Peierls[4)] in their discussions of quantum theory of electrons in solids in the presence of magnetic field. However, in the age, the experimental knowledge was restricted to Bi.

On the other hand, a considerably long period was necessary until the quantum effect in the transport phenomena was well understood. A great progress had been made in the field by Titeica,[5)] who published a theory of electrical conductivity of metals in strong magnetic fields, though the oscillatory behavior had not been discussed. In 1940, an advance in the understanding of the oscillatory magnetoresistance in Bi was made by Davydov and Pomeranchuk.[6)] More detailed theoretical works for the quantum effects of the transverse and longitudinal magnetoresistances have appeared one after another, after the middle of 1950's in articles by Zil'berman,[7)] Lifshitz,[8)] Argyres,[9,10)] Kubo et al.,[11)] Adams and Holstein,[12)] and Kahn and Frederikse.[13)]

In order to understand the quantum effects, we require not only the knowledges of the density of states of the free carrier gas in the presence of the magnetic field, but of the scattering mechanisms of the free carriers and their field dependence. The scattering mechanisms treated in the papers mentioned above are mainly elastic ones, such as the scattering by acoustic phonons and that by ionized impurities. Using either scattering mechanisms of the above two, they could obtain similar results both for the transverse and longitudinal magnetoresistances.

On the other hand, the oscillatory magnetoresistances in the degenerate semiconductors with very high carrier mobility and in metals, for instance, InSb,14,15) InAs,16,17) Zn,18) and so on, were measured and experimental data of the quantum oscillation were analyzed in detail on the basis of the theories by the authors mentioned above. Then, in 1960's, when high quality crystals had become available as a result of the advance in the techniques of preparing crystals, the observations of the oscillatory magnetoresistance, which is often called the Shubnikov-de Haas (SdH) effect, were extended to other semiconductors, semimetals, and metals, such as GaAs,19) grey tin,20) HgSe,21) HgTe,22-25) $Hg_{1-x}Cd_xTe$,26) Mg,27) and so on, and more detailed analyses were carried out on these materials.

At the present, the SdH effect is considered as one of the most powerful tools for investigating the electronic properties of degenerate semiconductors, semimetals, and metals. Various physical parameters of these materials can be obtained by the method: the effective mass, the carrier concentration, the shape and the size of the Fermi surface in k-space, the Dingle temperature,28) and the band parameters such as the momentum matrix element.

The spin splittings of the SdH oscillations were first observed in InAs,29) InSb,30-32) and then in HgTe,33) GaSb,34) $Hg_{1-x}Cd_xTe$,35-37) PbTe,38) and $Pb_{1-x}Sn_xTe$.39,40) We can estimate the effective g-value from the analysis of the spin splittings of the oscillatory peaks.

However, we have few papers in which the spin effect of SdH oscillations is discussed. Gurevich and Ėfros[41)] have presented a theory on the spin splitting in the transverse magnetoresistance(TMR), assuming that the scattering does not give rise to the electron spin flip. Ėfros[42)] has provided an explanation of the vanishing of H_0^+ peak in the longitudinal magnetoresistance(LMR) observed in InSb. He also assumed that the probability of the scattering transitions with spin reversal would be very small. Recently, Suizu and Narita[37,43)] have studied the spin effects on the SdH oscillations in $Hg_{1-x}Cd_xTe$ alloys for the TMR and LMR. They paid their attention to the difference of the spin effects between the TMR and LMR in the alloys with various x-values ranging from the semimetal to the semiconductor side. In their measurements, for the TMR, the spin splitting peaks H_0^+ corresponding to the upper sublevel of N=0 Landau level and H_1^+, H_1^-, H_2^+, H_2^-,---, H_N^+, H_N^-, corresponding to the upper and lower sublevels of N=1, 2,---,N Landau levels, respectively, are observable, while in the LMR, H_0^+ and the series of H_N^- peaks are missing. For the explanation of the above effects, they formulated a theory in which the spin flip scattering due to the spin-orbit interactions was taken into account. As a result, they obtained the selection rules both for the TMR and LMR, and could explain the difference of the spin effects between them and also the changes from semimetal to semiconductor side.

Though we have many theories treating various scattering mechanisms, the author wishes to restrict the review to the papers concerning the present study.

I.2. Historical Survey of Studies on $Pb_{1-x}Sn_xTe$ alloys

During the last ten years, the lead-tin chalcogenides, especially pseudobinary PbTe-SnTe alloy systems have been of much current interests for their attractive physical properties such as the extremely small band gaps,[44] small effective masses,[44] large electronic g-values,[45-47] and large dielectric susceptibilities,[48-51] as well as for their possibilities of applications to devices for infrared light emission[44-47] and detection.[48] In PbTe, the valence and conduction band edges are believed to be located at the L-point of the Brillouin zone, and are designated respectively as L_6^+ and L_6^-. According to the band model proposed by Dimmock et al.,[44] the energy gap of $Pb_{1-x}Sn_xTe$ alloy decreases with increasing SnTe composition, and comes close to zero at some value of x, where the crossover of the valence and conduction bands takes place. Since both the L_6^+ and L_6^- states have only two-fold spin degeneracy, their crossover does not result in a semiconductor-semimetal transition but in a semiconductor-semiconductor transition, in contrast to the case of $Hg_{1-x}Cd_xTe$ alloy system.

Fig.1 is a schematic diagram for the valence and conduction bands of PbTe, $Pb_{1-x}Sn_xTe$ (at $E_G=0$), and SnTe, in the vicinity of the L-point of the Brillouin zone.

The band inversion model has been confirmed by measurements of the temperature dependence of the electrical conductivity in alloys with compositions near the crossover point,[52] and also by the measurements of the Hall effect under high pressures.[53]

Experimental studies of the Fermi surface of PbTe have been done through the measurements of the de Haas-van Alphen effect,[54] the SdH effect,[38,55] Azbel'-Kaner cyclotron resonance,[56,57] the magnetoacoustic attenuation,[58] the magnetoelastic effect.[59] The conduction band g-factors of PbTe have been determined by the measurements of electron spin-flip Raman scattering,[60] the SdH effect,[38,55] and the laser emission under the magnetic field.[61]

Though less informations are available for the $Pb_{1-x}Sn_xTe$ alloys, the experimental studies of the Fermi surface and the band edge structures have also been carried out upon the alloy system, by SdH effect,[39,40,62,63] interband magneto-absorption,[64] far infrared cyclotron resonance,[65] and infrared laser emission under the magnetic field.[45-47]

From the results described above, the shape of the Fermi surface of holes in PbTe and $Pb_{1-x}Sn_xTe$ with relatively small x-value, is believed to be almost perfect [111] ellipsoid, however the shape of the Fermi surface of SnTe still remains somewhat uncertain.[66-69]

To date, we have had the data of the band edge parameters of $Pb_{1-x}Sn_xTe$ alloys obtained only from the measurements of SdH effect,[39,55,63] and the measurements of the Knight-shift.[70,71] However, these measurements and hence the knowledges are restricted almost only to the valence band, because preparing the n-type materials has been difficult. Therefore the structure of the conduction band edge has still remained obscure.

Recently, SnTe, and $Pb_{1-x}Sn_xTe$ have attracted great interest on their softening of TO-phonon[49,50,72-76] and the relating carrier concentration dependent temperature induced phase transition from NaCl to the ferroelectric phase GeTe type crystal structure.[72-75] In addition, by the author, the pressure induced phase transition from NaCl to the orthorhombic crystal structure were observed in $Pb_{1-x}Sn_xTe$ and SnTe.[53]

On the other hand, the theoretical studies of the band structure had been carried out for the lead chalcogenides and lead-tin chalcogenides. The band structures of PbTe and SnTe had been calculated by the APW,[77] OPW,[78] pseudopotential,[79-81] KKR,[82] and the $\vec{k}\cdot\vec{p}$ perturbation method.[68,69,83] These band structure calculations also indicate that the valence and conduction band extrema of PbTe to be located at the L-point and to have the

L_6^+ and L_6^- symmetries, respectively. All the band structure calculations so far performed on SnTe[69, 79-81] have well agreed with the band inversion model. However, we have had no direct calculation on the band structure of the lead-tin chalcogenides. Recently, the band structure calculations of the $Pb_{1-x}Sn_xTe$ alloys were carried out basing on the band inversion model using the $\vec{k}\cdot\vec{p}$ perturbation theory.[84, 85] These results have showed considerably good agreement with the experimental results in p-type PbTe, and $Pb_{1-x}Sn_xTe$ alloys at the PbTe-rich side of the crossover.

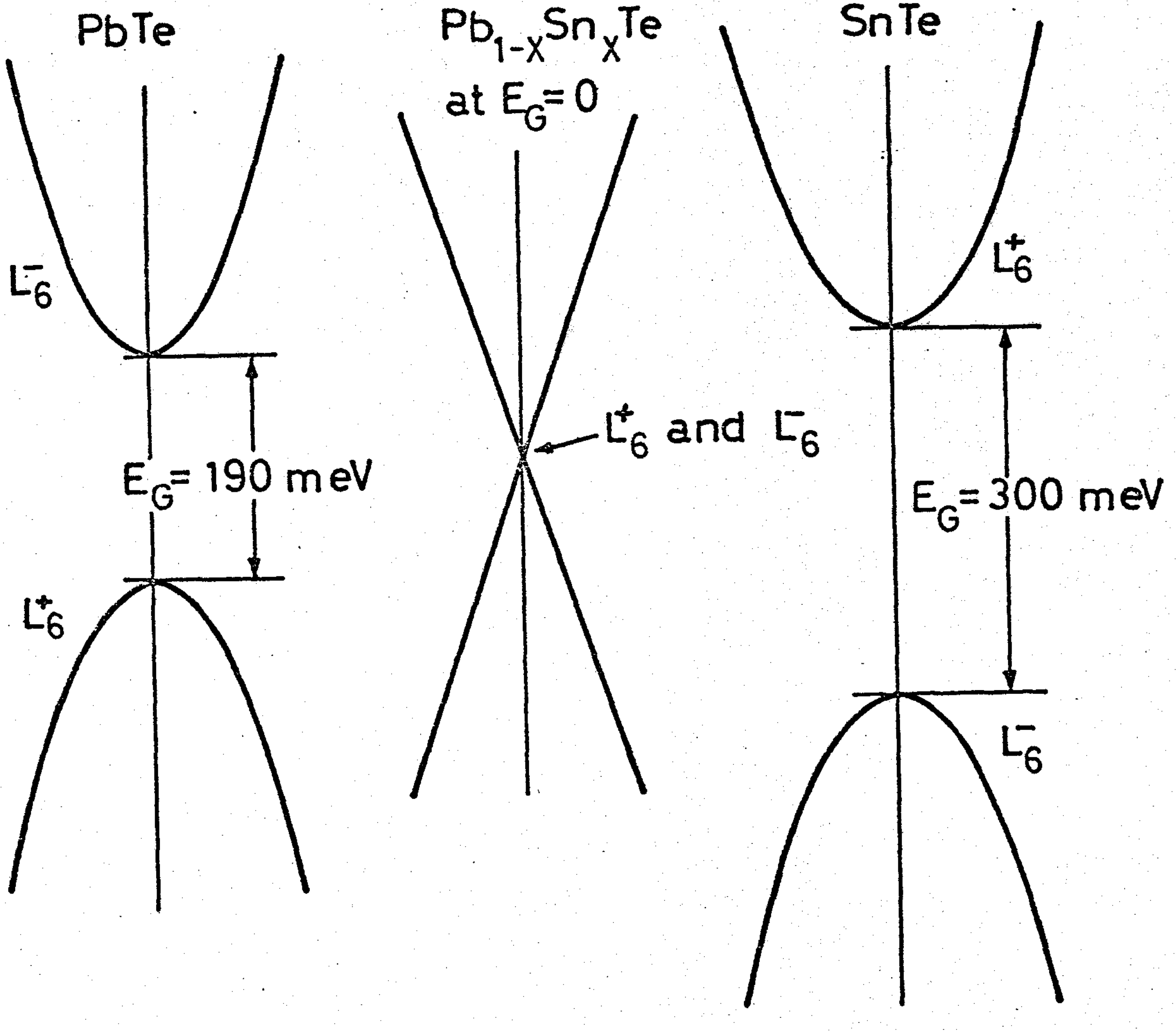

Fig.1 Schematic diagram for the valence and conduction bands of PbTe, $Pb_{1-x}Sn_xTe$(at $E_G=0$), and SnTe, in the vicinity of the L-point in the Brilloin zone.

II. Theory of Shubnikov-de Haas Effect

II.1. General Theory

The SdH effect can occur under the conditions that the Fermi energy ζ is much greater than the thermal energy kT (degenerate statistics), $\zeta \gg kT$, and that a number of oscillator states are occupied, $\zeta > \hbar\omega_c$, and that the cyclotron motions are well defined, $\omega_c\tau \gg 1$.

When electrons are moving in a steady magnetic field, the energies of the electrons are quantized into the harmonic oscillator states and the uniform distribution of the quantum states in k-space are replaced by a series of inter-locking Landau cylinders with the cross sections A_N perpendicular to $\vec{H}$, which is given by

$$A_N = \frac{2\pi eH}{c\hbar}(N+1/2) , \qquad (II.1)$$

if the spin is omitted. The discrete nature of the Landau cylinders is smeared out unless $\hbar\omega_c \gg kT$, which is an additional requirement for the quantum effects to be observed. Onsager87) showed that the eq.(II.1) is valid for the Fermi surfaces of arbitrary shapes.

For an electron moving along a closed orbit perpendicular to $\vec{H}(0,0,H)$ upon the Fermi surface, the cyclotron frequency ω_c is given by the equation

$$\omega_c = 2\pi[\oint dt]^{-1} = \frac{2\pi eH}{c\hbar^2} [\frac{\partial A(E,k_z)}{\partial E}]^{-1}, \qquad (II.2)$$

where $A(E,k_z)$ is an area enclosed by the orbit. The cyclotron effective mass m_c^*, related to the Landau level separation $\hbar\omega_c$, is connected to a cross section of the Fermi surface as

$$m_c^* = \frac{\hbar^2}{2\pi} \frac{\partial A(E,k_z)}{\partial E} . \qquad (II.3)$$

If the energy levels are filled up to the Fermi level ζ with electrons, and if $\zeta \gg \hbar\omega_c$, $\omega_c\tau \gg 1$, and $\hbar\omega_c \gg kT$, the maxima in the scattering which result in maxima in resistivity, will occur in the magnetoresistance whenever the Fermi level coinsides with the Landau levels, as the scattering probability increases because of the singularity at the bottom of the Landau levels. If the Fermi level stays constant (classical limit), the oscillations of the magnetoresistance are periodic against 1/H. The period both in the TMR and LMR is[13)]

$$P = \Delta(1/H) = \frac{2\pi e}{c\hbar} \frac{1}{A(\zeta,k_z)} \quad . \qquad (\text{ II.4 })$$

Though the cross sectional area, in general, is a function of k_z and hence the cross sections at different k_z give different periods, the dominant contribution comes from cross sections whose periods are stationary with respect to small change in k_z. The area enclosed by such an orbit is called the extremal cross section. Thus the period is given as

$$P = \Delta(1/H) = \frac{2\pi e}{c\hbar} \frac{1}{A_{ex}} \quad , \qquad (\text{ II.5 })$$

where A_{ex} is the extremal area of the Fermi surface perpendicular to the magnetic field.

For the TMR and LMR, the explicit formulae of the quantum oscillations have been deribed. According to Roth and Argyres,[88)] the LMR is given, assuming an isotropic scattering and $kT \ll \hbar\omega_c$, by

$$\rho_{\parallel}^{-1} = \rho_0^{-1} \frac{4\zeta_0^{1/2}}{n\hbar\omega_c} \sum_{\pm} \frac{n_{\pm}}{\sum_N [\, \zeta - (N+1/2 \pm \nu/2)\hbar\omega_c]^{-1/2}} \quad , \qquad (\text{ II.6 })$$

where $\rho_0 = m/ne^2\tau_0(\zeta_0)$ is the resistivity without magnetic field, and $n_{\pm}$ is the density of electrons with spin up(+) and spin down(-), N is the Landau quantum number, and $\nu = m_c^* g/2m$ is the spin splitting factor. In the above expression, the spin splittings of the Landau levels are taken into account through the density of states. The above expression is a little complicated, because the resistivities for two spin should be coupled in parallel. For $\zeta \gg \hbar\omega_c$, the relaxation times can be approximated by taking simple average for the two spins. For arbitrary $kT/\hbar\omega_c$, the oscillatory resistivity can be expressed explicitly, using the Poisson's summation formula89)

$$\rho_{\parallel} = \rho_0 [\ 1 + \sum_{r=1}^{\infty} b_r \cos\left(\frac{2\pi\zeta}{\hbar\omega_c} r - \frac{\pi}{4} \right)] \ , \qquad (\text{ II.7,a })$$

where

$$b_r = \frac{(-1)^r}{r^{-1/2}} \left(\frac{\hbar\omega_c}{2\zeta} \right)^{1/2} \frac{2\pi^2 rkT/\hbar\omega_c}{\sinh(2\pi^2 rkT/\hbar\omega_c)} \cos(\pi\nu r) e^{-2\pi\Gamma r/\hbar\omega_c} \ . \qquad (\text{ II.7,b })$$

Moreover, for the TMR at 0 K is given by

$$\rho_{\perp} = \rho_0 \frac{3(\hbar\omega_c)^3}{16\zeta_0^2} \sum_{N,N',\pm} \frac{N+1/2}{[\zeta - (N+1/2 \pm \nu/2)\hbar\omega_c]^{1/2}} \frac{1}{[\zeta - (N'+1/2 \pm \nu/2)\hbar\omega_c]^{1/2}} \ . \qquad (\text{ II.8 })$$

Again, for finite temperature

$$\rho_{\perp} = \rho_0 \ [\ 1 + \frac{5}{2} \sum_{r=1}^{\infty} b_r \cos\left(\frac{2\pi\zeta}{\hbar\omega_c} r - \frac{\pi}{4} \right) + R\ ] \ , \qquad (\text{ II.9,a })$$

and

$$R = \frac{3}{4} \frac{\hbar\omega_c}{2\zeta} \{ \sum_{r=1}^{\infty} b_r (\alpha_r \cos(2\pi\zeta r/\hbar\omega_c) + \beta_r \sin(2\pi\zeta r/\hbar\omega_c)) - \ln(\ 1 - 4\pi\Gamma/\hbar\omega_c) \} \ , \qquad (\text{ II.9,b })$$

where b_r is given by eq.(II.7,b) and

$$\alpha_r = 2r^{1/2} \sum_{s=1}^{\infty} \frac{1}{[s(r+s)]^{1/2}} e^{-4\pi s\Gamma/\hbar\omega_c} \ , \qquad (\text{ II.9,c })$$

and

$$\beta_r = r^{1/2} \sum_{s=1}^{r-1} \frac{1}{[s(r-s)]^{1/2}} \ . \qquad (\text{ II.9,d })$$

In the above expressions Γ represents collision broadning or the broadning coming from inhomogeneity of carrier density in the crystal, and can be expressed by $\Gamma=\hbar/\tau=\pi kT_D$, where T_D, the broadning temperature, is called the Dingle temperature.28) In eq.(II.9,a), the second term is the contribution to the oscillatory part of the TMR due to the transitions changing the quantum number N. R represents the contribution of the transitions which do not change N. In practice R would be unimportant when the collisions are frequent enough to damp out r>1 harmonics. This conclusion was reached by Adams and Holstein12) on the basis that the divergent term is quadratic in the oscillatory part of ρ. Comparing eq.(II.6) with eq.(II.8), it is seen that the divergence of eq.(II.6) is not so sharp as that of eq.(II.8) at $\zeta=(N+1/2\pm\nu/2)\hbar\omega_c$. Therefore in experiments, clear spin splittings can be expected for the TMR compared to the longitudinal one. However, the results of the present study on $Pb_{1-x}Sn_xTe$ as well as the results on $Hg_{1-x}Cd_xTe$37) could not be explained by this theory where the effects of the spin up and down states upon the amplitude are equivalent, whereas the experimental results indicate that they are not.

For the spin splitting peaks in the TMR, the peak positions are given by the following formulae given by Gurevich and Éfros;41)

$$H_N^+ = \frac{2\hbar c}{e}\left(\frac{\pi^2}{2}\right)^{2/3} n^{2/3}\left[\sum_{s=0}^{N} \sqrt{s}+\sqrt{s-|g|m^*/2m}\,\right]^{-2/3}, \qquad (\text{ II.10,a })$$

$$H_N^- = \frac{2\hbar c}{e}\left(\frac{\pi^2}{2}\right)^{2/3} n^{2/3} \sum_{s=1}^{N} \sqrt{s}-\sqrt{s-|g|m^*/2m}\,]^{-2/3}. \qquad (\text{ II.10,b })$$

In the above calculations, they assumed that the scattering does not flip the electron spin.

II.2. Theory of Ellipsoidal Fermi Surface

For the ellipsoidal Fermi surface, and for oscillatory component of the TMR, we will able to use the following expression which is slightly modified the expression given by Roth and Argyres,88)

$$\rho = C\rho_o \sum_{r=1}^{\infty} b_r \cos[\ 2\pi(rc\hbar A_{ex}/2\pi e)H^{-1} - 2\pi\gamma - \pi/4\ ]\ , \qquad (\ II.11,a\ )$$

where

$$b_r = \left(\frac{\hbar\omega_c}{2r\zeta}\right)^{1/2} \frac{2\pi^2 rkT/\hbar\omega_c}{\sinh(2\pi^2 rkT/\hbar\omega_c)} \exp[-2\pi^2 rkT_D/\hbar\omega_c]\ \cos(\pi\nu r)\ . \qquad (\ II.11,b\ )$$

In the above expression, ρ_o is the zero field resistivity, C is a constant which depends upon the orientation of the magnetic field relative to the current direction, and A_{ex} is the extremal cross sectional area of the Fermi surface in k-space perpendicular to the field. The remaining symbols have their usual meanings.

For the LMR, similar expression can be used.

If there exists only one extremal area, the period of the fundamental oscillation is

$$P = (2\pi e/c\hbar)A_{ex}^{-1} = 9.55 \times 10^{-7}\ A_{ex}^{-1}\ , \qquad (\ II.12\ )$$

where the unit of A_{ex} is cm^{-2} , and P is in Oe^{-1}. If the Fermi surface has an additional extremal area, or as in the case of $Pb_{1-x}Sn_xTe$, if there are certain number of extremal areas, the summation over the additional extremal cross sections should be simply included.

For an ellipsoid of revolution, eq.(II.12) becomes

$$P = (2\pi e/c\hbar)(3\pi^2 n')^{-2/3}K^{-1/6}[\ 1+(K-1)\cos^2\alpha\ ]^{1/2}$$
$$= 3.18\ \ 10^{-6}(n'/10^{18})^{-2/3}K^{-1/6}[\ 1+(K-1)\cos^2\alpha\ ]^{1/2}\ , \qquad (\ II.13\ )$$

where n' is the number of carriers enclosed in an ellipsoid, and related to the total carrier density n as $n=4n'$, and α is the angle between the direction of the magnetic field and the major axix of the ellipsoid, and K is the anisotropy constant defined by the ratio of the maximum-to-minimum cross sectional area.

III. Material Preparation

Lead and tin combined with tellurium are known as PbTe and SnTe. By mixing these two materials, we obtain pseudo-binary alloy system $Pb_{1-x}Sn_xTe$ which exhibits cubic rocksalt crystal structure for all x-values ($0 \le x \le 1$). Single crystals of $Pb_{1-x}Sn_xTe$ have been prepared by several techniques: the Bridgman-,[48,90] Czochralski-,[48,91] and closed tube vapor transport-techniques[48,90,92] The temperature-composition phase diagram for $Pb_{1-x}Sn_xTe$ alloys[93] through out the composition range is shown in Fig.2. Scince the separation of liquidus and solidus line is not so wide, crystals with considerably homogeneous composition x have been able to grow by Bridgman or Czochralski technique. The crystals with more homogeneous composition have been prepared by the vapor transport method. However, as-grown crystals by above methods always exhibit p-type conduction and have very high carrier concentrations, 10^{19}-10^{21} cm^{-3}. It has been suggested that the predominant native defects in lead chalcogenides are Pb and nonmetal vacancies.[94-96] It is now confirmed that the origin of very large number of holes[48,90] mentioned above is the metal lattice vacancies which act as acceptors, and generally these vacancies form predominant native lattice point defects in all the IV-VI compounds.

The temperature-composition phase diagram for PbTe[90] is shown in the upper part of Fig.3. The lower part is a schematic representation of the phase diagram for PbTe and $Pb_{0.87}Sn_{0.13}Te$[90] on a greatly magnified scale in the vicinity of stoichiometric composition. As one can see in the lower part of Fig.3, solidus line of PbTe touches its liquidus line at the maximum melting point, where the composition deviates about 9×10^{18} cm^{-3} atoms from the stoichiometric composition to the Te rich side. Therefore the crystals grown by above methods contain very large number of holes. Though the Te-saturated solidus line approaches the stoichiometric composition with decreasing temperature, it never cross the stoichiometric line, whereas the metal-saturated solidus line crossover the stoichiometric composition line. at considerably low temperature, below which the chemical composition of the crystal becomes metal rich, ie. the crystal contains less metal vacancies than Te vacancies which act as donors, as is seen in the lower part of Fig.3. The above crossing temperature decreases with increasing SnTe composition. This property is common to the most of IV-VI compounds. In the vicinity of these temperatures the chemical composition of the crystal is nearly stoichiometric. In addition, since the equilibrium concentration of a particular lattice point defect such as a vacancy or an interstitial can be expressed by the equation48) $N=N_0\exp[-E/kT]$, it is more preferable to grow crystals at lower temperature, where N is the density of the defects, N_0 is the constant proportional to the lattice site, and E is the formation energy for the defect.

As the crystals grown by above methods have very large number of holes, the mobilities of the free carriers in the crystals are usually very small even at low temperatures due to the scatterings by ionized lattice vacancies. In order to reduce the hole concentration, or to convert as-grown crystals into n-type, annealing of the crystals for an extremely long period at low temperature48,90) is required. However a difficulty still remains for obtaining high quality crystals, especially the crystals with holes less than 10^{16} cm^{-3}, and in practice, it is almost impossible to convert into n-type by annealing.

Considering the fact mentioned above, we attempted another entirely different method for the present crystal growth: single crystal growth by molten metal solution, a kind of flux growth method in which molten metals are the flux. By this method, single crystals can be grown at considerably low temperatures, near or lower than the temperature where the metal saturated solidus line cross the stoichiometric composition line. In this method, single crystals of n-type $Pb_{1-x}Sn_xTe$ alloy were prepared from strongly non-stoichiometric melts. This melt contains less than 10 atomic percent of Te, typically 5-8 atomic percent of Te. The upper part of Fig.3 shows that the solubility of Te in the melt is about 5 atomic percent of Te, and when the temperature is lowered crossing 600°C, the melt becomes supersaturated with Te, and then PbTe begins to crystallize in the melt. The as-grown PbTe crystal has the composition corresponding to the metal-saturated solidus line for PbTe near 600°C. This method can also be applied to PbTe-SnTe system, though the corresponding temperature is quite different. Thus the crystals with nearly stoichiometric composition, and especially n-type crystals, can be easily grown. Moreover, the present crystal growth method has an additional merit that the temperature of crystal growth is considerably low, so that the lattice point defects can be minimized, because the equilibrium concentration of the lattice point defects decreases exponentially with decreasing temperature.

For the preparation of the samples, possble commercially available high purity elements: lead, tin, and tellurium of 99.9999 %, were used. High purity Pb, Sn, and Te of non-stoichiometric composition were enclosed in an evacuated quartz ampoule, the inside wall of which is coated with a thin layer of graphite produced by pyrolysis of acetone to prevent the elements from reacting with quartz ampoule. Two different process for the crystal growth were employed: (1) the ampoule was fixed in a furnace and the temperature of the furnace was slowly decreased at the rate of about 4 °C/hour or (2) the ampoule was slowly pulled down at the rate of about 0.1 mm/hour in a furnace having temperature gradient. After above processes were completed, the grown crystals in the ampoule were separated from the melt, by raising the temperature again to about 350°C. The temperature profile of the furnace used is given in Fig.4. Cube, slab, or bar shaped single crystals with smooth (100) surface were obtained. Sometimes crystals with large (100) surface were grown. Fig.5 shows the photographs of the typical crystals grown by the present method. SnTe compositions of these crystals were about the half of those in the initial melts, as shown in Fig.6.

$Pb_{1-x}Sn_xTe$ alloys, thus obtained, have exhibited useful properties for the SdH measurements, such as the very high electron mobility, the good homogeneity of the carrier concentration and the alloy composition x, and the sufficiently low carrier concentration, and in addition, these crystals were always n-type. The homogeneity of carrier concentration is especially necessary for the SdH study, because the inhomogeneity smears the SdH signal seriously. Moreover, our main interests for the alloys are the band edge properties such as the extremely small effective mass and large g-value of carriers in the conduction band, it is preferable to use low carrier n-type materials in the experiment, because the Fermi level of high carrier material lies far from the band edge due to the strong nonparabolicity of the conduction band.

The x values of the crystals were determined by an X-ray Microanalyser within a few percent error.

In order to measure the magnetoresistance and the Hall effect, the obtained crystals were cut into oriented specimens with a typical dimmension of $1\times4\times0.25\ mm^3$, the long axes of which are parallel to the [100] or the [110] crystalline axes. These orientations were necessary for the study of these alloys with highly anisotropic Fermi surface. The samples were then etched to remove the surface contaminations and damages, and then the electrodes for the measurements were soldered to the samples by indium.

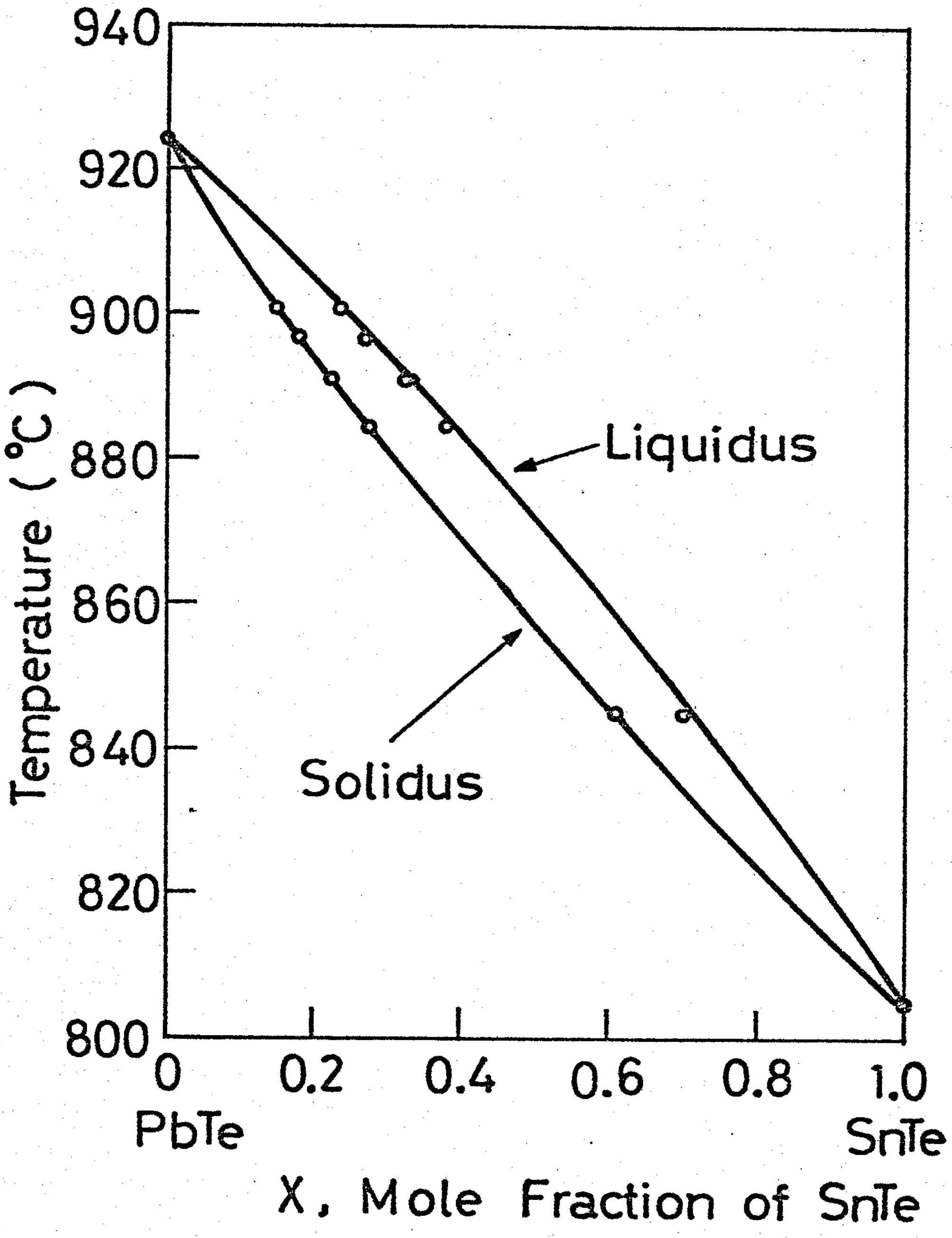

Fig.2 The temperature-composition pseudo-binary phase diagram for $Pb_{1-x}Sn_xTe$ alloys, according to Calawa et al.[94)]

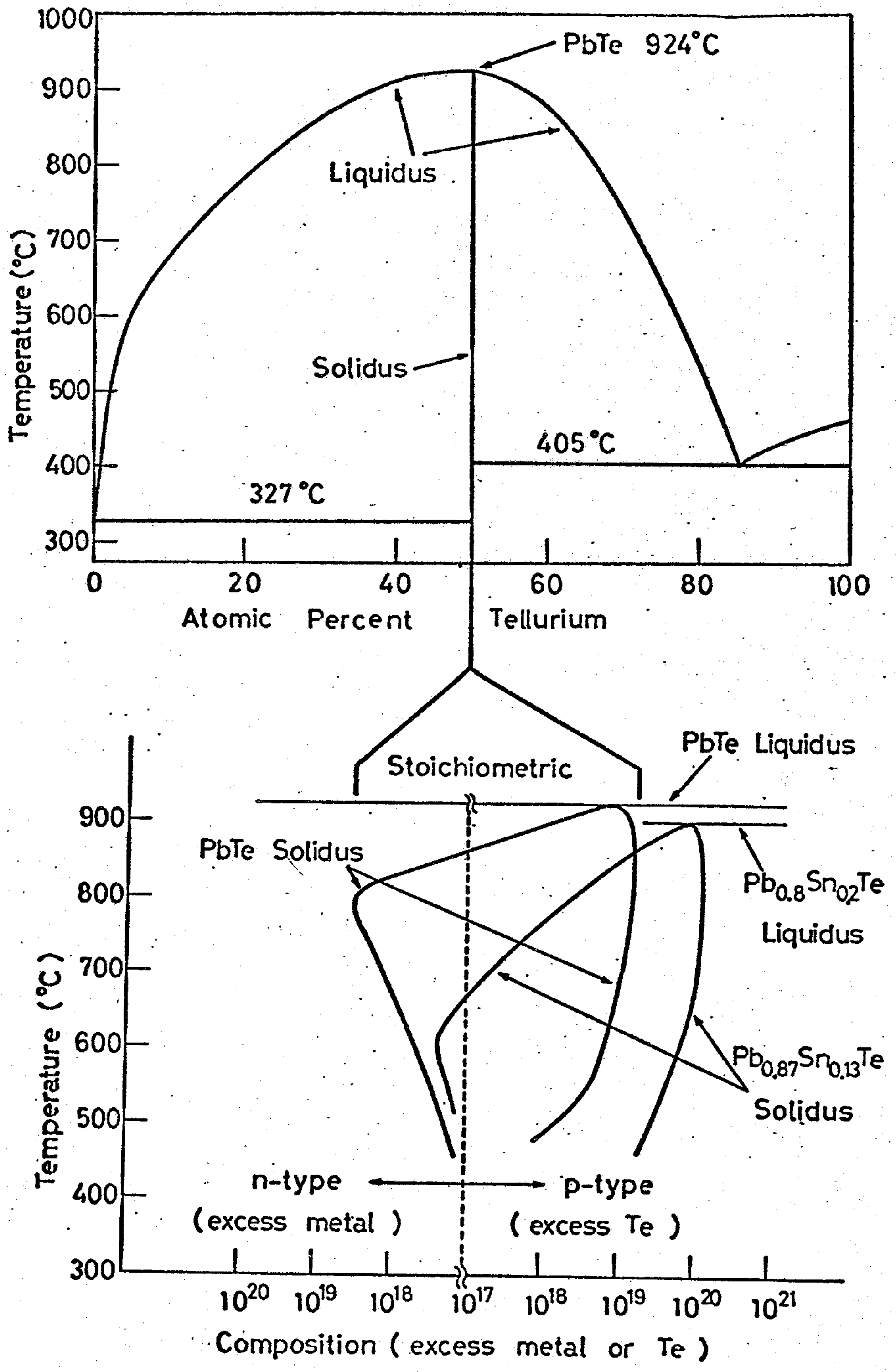

Fig.3 The upper part is the temperature-composition binary phase diagram of Pb and Te. The lower part is a schematic representation of the phase diagram for PbTe and $Pb_{0.87}Sn_{0.13}Te$ in the vicinity of the stoichiometric composition. The horizontal axis is greatly magnified. After Harman.[90)]

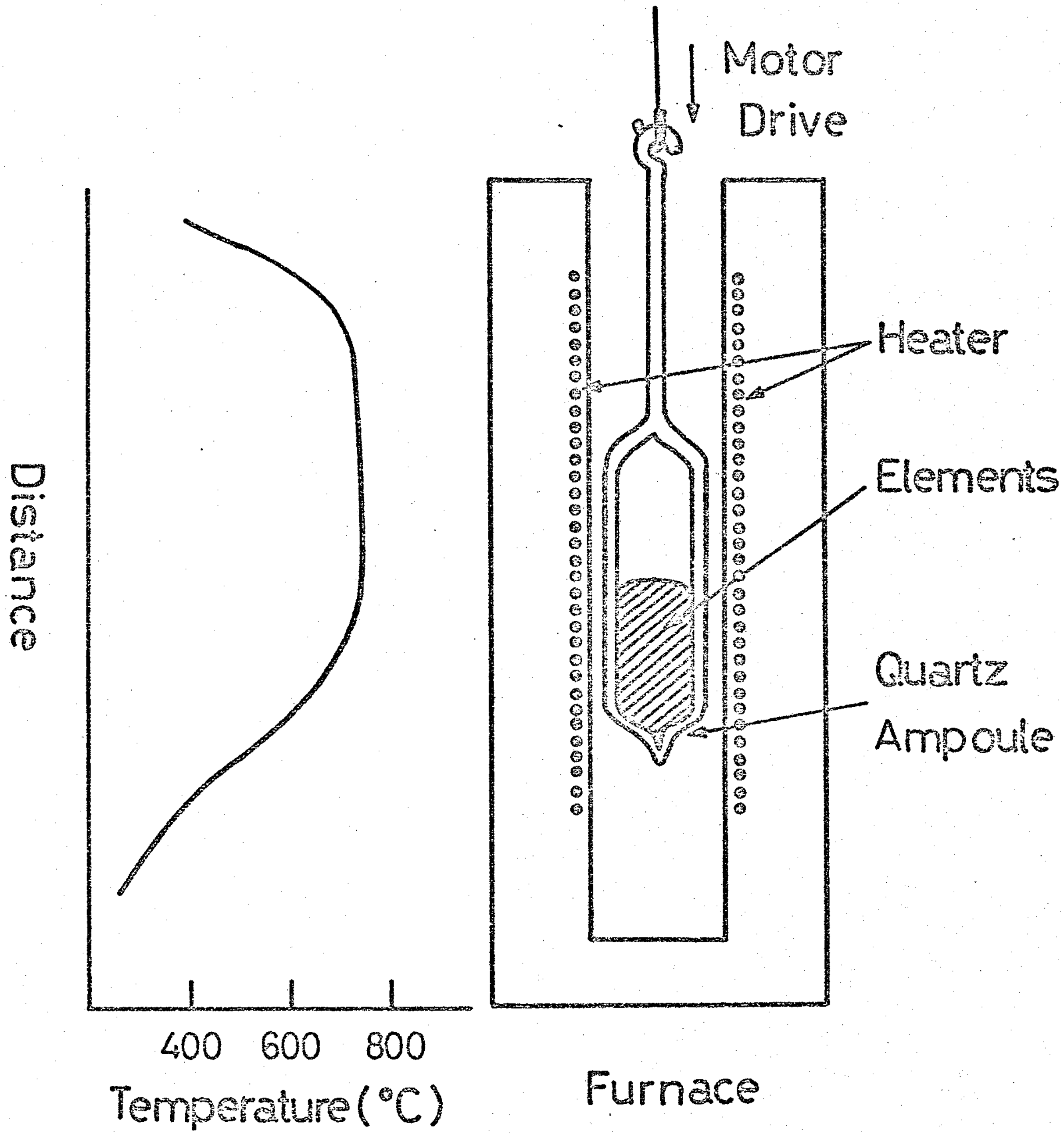

Fig. 4 Schematic diagram for the crystal growing apparatus used for the synthesis of $Pb_{1-x}Sn_xTe$ alloys and a typical temperature profile of the furnace.

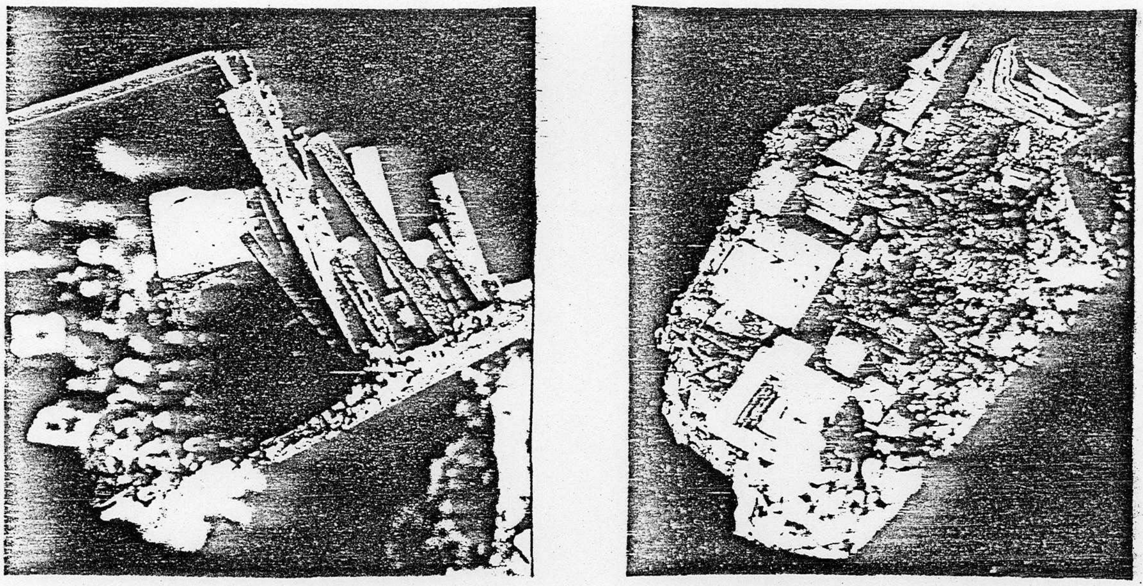

Fig.5 The photographs of typical as-grown $Pb_{1-x}Sn_xTe$ alloy crystals. The composition x of the right hand side is approximately 0.05, and that of the left hand side is approximately 0.2. The smooth (100) surface are seen in both the photographs.

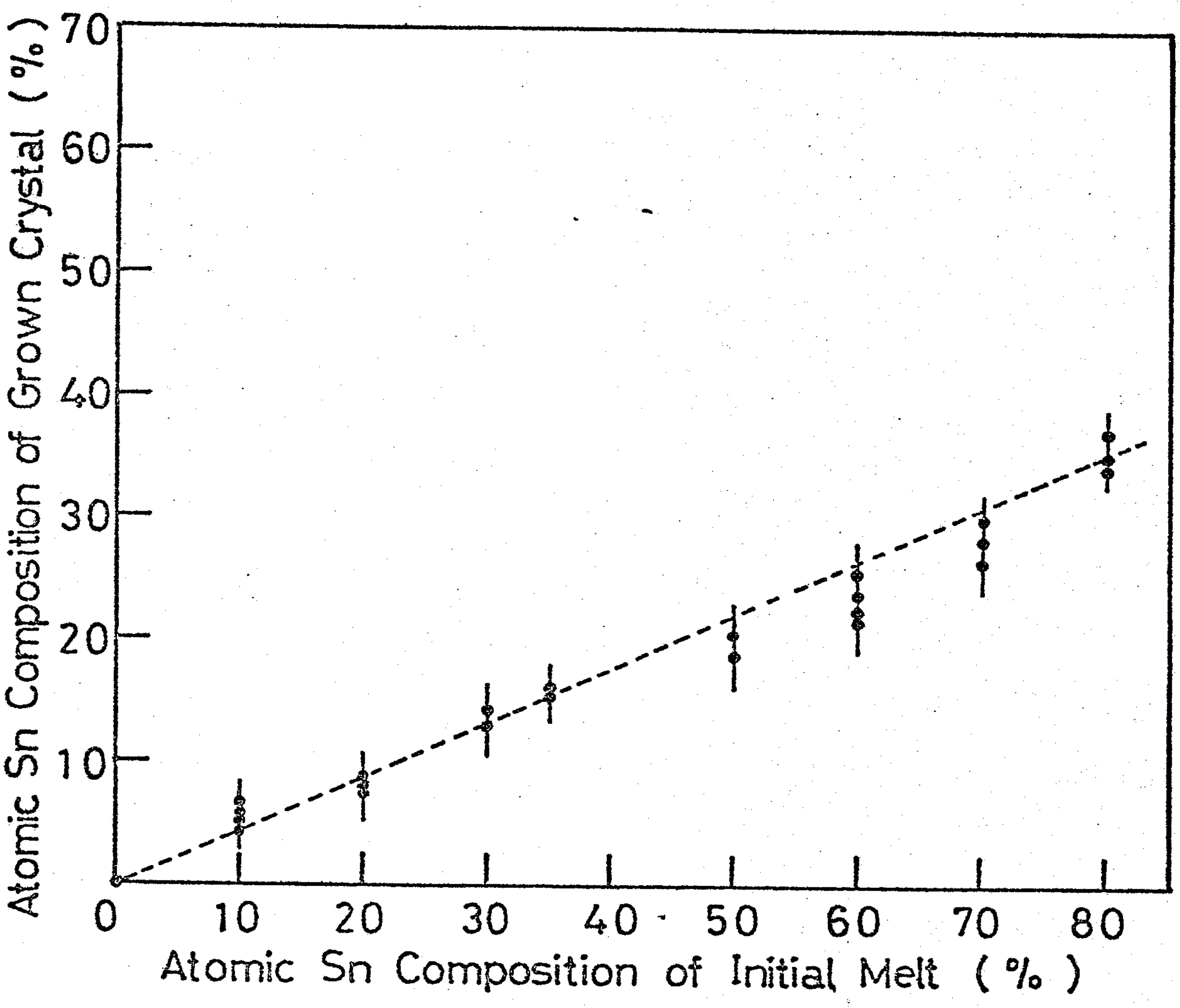

Fig.6 A diagram for the SnTe composition of grown crystal versus atomic Sn composition of the initial melt.

IV. Experimental procedure

Measurements of the SdH oscillation were carried out in the temperature range, 1.32-4.2 K. The samples were directly immersed in the liquid helium in a glass Dewar, as is illustrated in Fig.7. The samples were mounted on the specially prepared sample holders in order to set the crystalline axis in various desired directions with respect to the magnetic field, or on a single axis rotating sample holder shown in Fig.8 for the study of anisotropy of the Fermi surface.

Temperatures below 4.2 K were obtained by pumping the helium vapor, and were measured by vapor pressures using a calibrated pressure gauge.

Quasi static magnetic field was applied to the sample by using a superconducting magnet. The magnetic field was slowly swept by the aid of a constant current power supply at the sweep rate of 2.8 A/min.-0.3 A/min..

The scanning of the magnetic field was purely electronic so that the current could be varied automatically up to 50 A, which was stabilized within few milliampere fluctuation during sweeping. Such a stability was necessary for the measurements of high S/N ratio.

The oscillatory magnetoresistance signals were measured by means of conventional DC bucking technique or field modulation technique.

The upper and the lower parts of Fig.9 show block diagrams of the apparatus. In the DC measurements, signals of oscillatory magnetoresistance from the voltage probes on samples were amplified by a DC amplifier.†) When monotonous background magnetoresistance was large compared with the oscillatory component which was in general approximately linear in magnetic field, the bucking voltage was used to cancel the background magnetoresistance, before amplifying the oscillatory magnetoresistance signal. Thus the SdH signal could be obseved with sufficient sensitivity.

On the other hand, the field modulation technique was also employed to obtain the field derivatives of the SdH signals so as to observe fine structures due to small spin splittings and high field oscillations with small amplitude with high resolution and higher S/N ratio. In this case, the magnetic field was modulated at 14-40 Hz with the amplitude of about 50-120 Oe, by using an extra modulation coil. The voltage across the sample was fed to a phase sensitive lock-in amplifier[††)] detecting at the modulation frequency. The modulation coil was drived by a power amplifier which amplified the reference signal from the lock-in amplifier.

In both measurements, the out put signals from the DC amplifier or the lock-in amplifier were recorded as the Y-components of an X-Y recorder, while the X-components represent the magnetic field strength.

During the measurements, the current through the sample was maintained constant, at eg. 15 mA, by using a battery.

---

†) OHKURA ELECTRIC MODEL AM-1001 MICROVOLT METER containing a high grade DC amplifier.

††) P.A.R. MODEL HR-8.

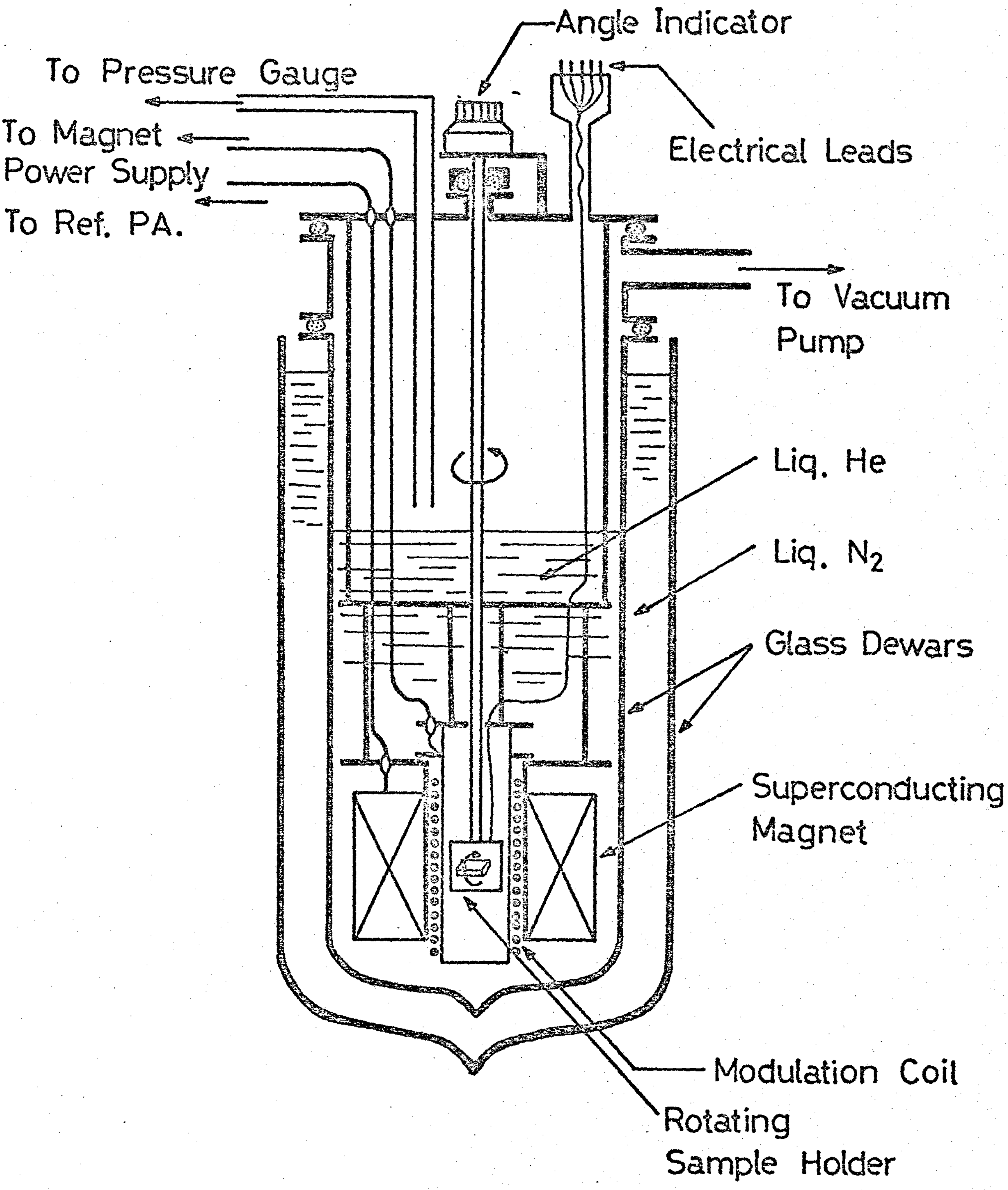

Fig.7 A schematic representation of the cryogenic apparatus for measuring the SdH effect.

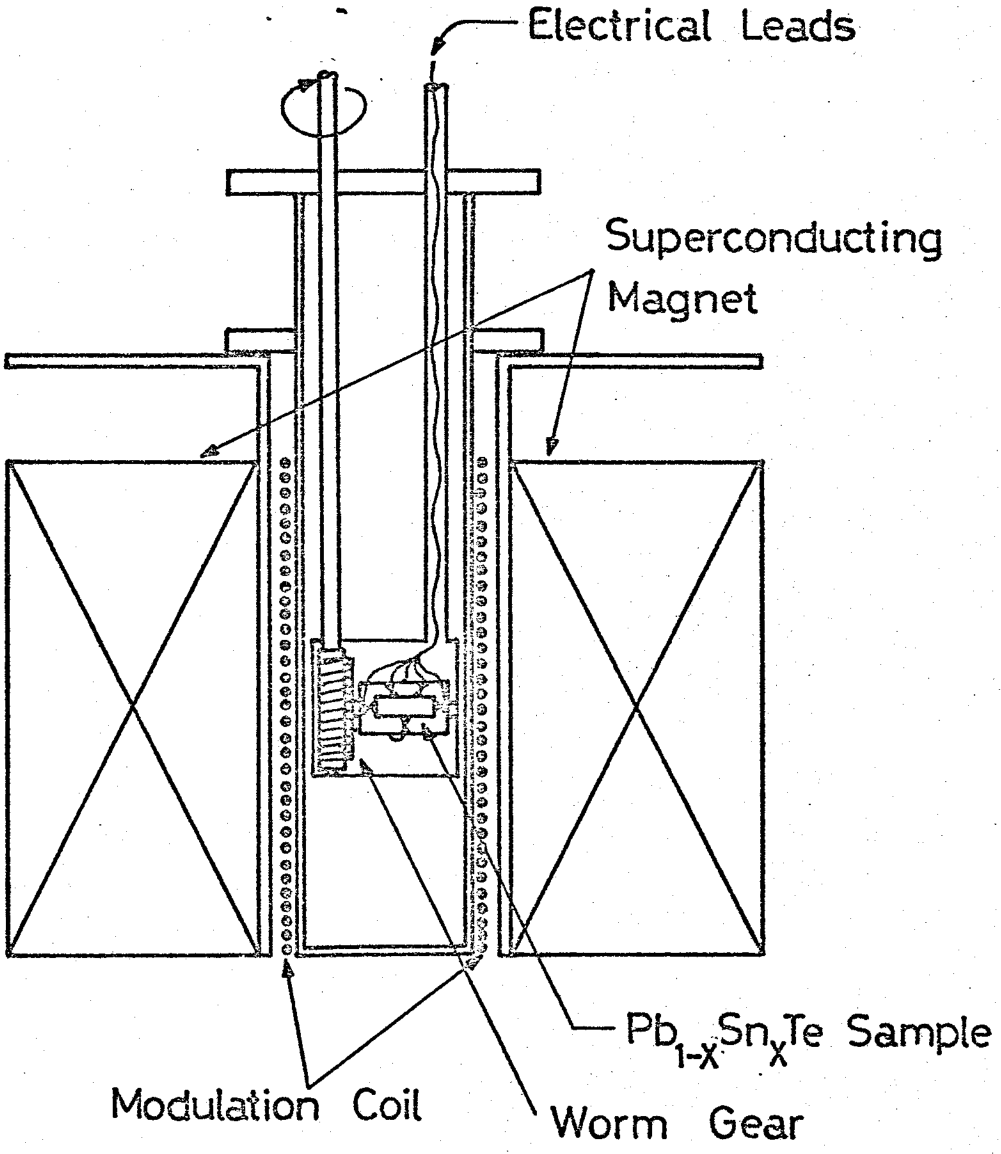

Fig.8 An enlarged illustration of the rotating sample holder. The sample holder can be rotated as precisely as an error of 0.5 degree, by using a set of worm gear.

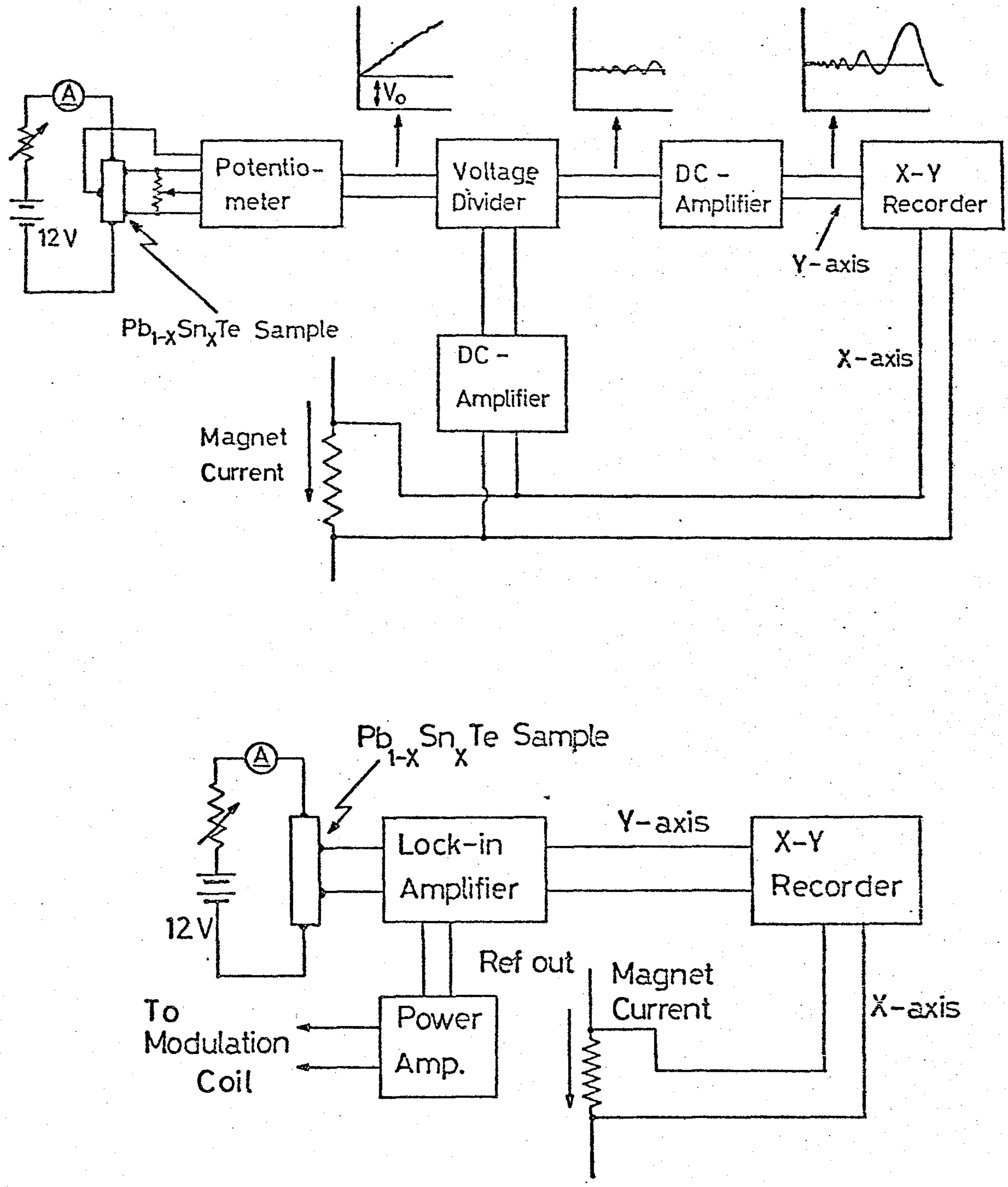

Fig.9 The upper part of the figure represents the block diagram of the apparatus used for the measurements of SdH signal by means of DC bucking technique. The lower part represents the block diagram of the apparatus used for the measurements of SdH signal by means of field modulation technique.

V. Experimental Results

As we have described in chapter I, the Fermi surface of holes and electrons in $Pb_{1-x}Sn_xTe$ alloys are believed to be the [111] ellipsoids. Hence the SdH signal in the magnetic field not parallel to the [100] direction must be quite complicated, because in an arbitrary field direction, we have several different size extremal cross sections for $Pb_{1-x}Sn_xTe$ which result in complicated oscillatory signals being composed of several different period oscillations.

Therefore, in the SdH measurements of $Pb_{1-x}Sn_xTe$ alloys, we chose the [100] axis as the field direction, in order to study the difference between the TMR and LMR, especially in the spin effect of SdH oscillation.

In order to study the shape of the Fermi surfaces, we used various samples in the measurements of TMR, having the axes parallel to various crystalline axes or we rotated the sample with respect to the magnetic field. In all the measurements, the accuracy of the sample orientation was as good as an error of few degree, which was confirmed by the observation of no beat signal in the SdH oscillations, when the magnetic field is directed to the [100] or the [110] crystalline axes.

The upper and the lower parts of Figs.10-14 show the recorder traces of the transverse and longitudinal oscillatory magnetoresistance signals as a function of the magnetic field, respectively, in the case of the magnetic field parallel to the [100] axis. In general, as in the case of InSb, and $Hg_{1-x}Cd_xTe$, the monotonous background magnetoresistance in $Pb_{1-x}Sn_xTe$ sample was very small in the longitudinal magnetoresistance and relatively large in the transverse one. Moreover, in the [100] field direction, only single period of oscillation in 1/H could be observed both in the TMR and LMR.

In the TMR, though the spin splittings of the oscillatory peaks were not clear, doubling of oscillatory peaks which we assigned the H_0^+ and H_1^-, respectively the peak positions corresponding to he up spin sublevel of N=0 Landau level and the down spin sublevel of N=1 Landau level, were almost always observed. We have the case $Pb_{1-x}Sn_xTe$ (x=0.186) when even the doubling of H_0^+ and H_1^- oscillatory peaks were not resolved, as shown in Fig.14.

On the other hand, in the LMR, contrary to the TMR, H_0^+ oscillatory peak which is the highest field peak in the TMR, was completely missing for all the samples studied, in contrast to the case of many other narrow gap materials such as InSb, HgTe, and $Hg_{1-x}Cd_xTe$ in the LMR: we observed the missing of only the highest field oscillatory peak in n-type $Pb_{1-x}Sn_xTe$ (PbTe-side of the crossover) in contrast to the case of InSb,36) HgTe,98) and $Hg_{1-x}Cd_xTe$,37,43,95) in which the two highest field oscillatory peaks are missing. According to our peak assignment, which is discussed in detail in chapter VII, the H_0^+ peak and perhaps the series of the H_N^+ peaks are missing in n-type $Pb_{1-x}Sn_xTe$, but the most striking difference is the appearance of the H_1^- peak in the LMR, in contrast to the case of InSb, HgTe, and $Hg_{1-x}Cd_xTe$.

Moreover, the doubling of the oscillatory peaks due to the spin splittings becomes inaccurate with increasing x-value.

In Fig.15, the recorder traces of the TMR signal versus magnetic field for PbTe are given. The upper part represents the SdH signal when $\vec{H}$ // [100], whereas the lower part represents the one when $\vec{H}$ // [110]. In both field directions, the clear spin splittings can be observed up to N=3.

Figs.16-17 show the recorder traces of the field derivatives of the TMR signal versus magnetic field which represent the angular dependence of the

SdH signals, when the samples were rotated in the (100) or (110) plane. It can be noticed in Fig.16 (x=0.066) that the spin splitting of H_0^+ and H_1^- is greater when $\vec{H}$//[111] than when $\vec{H}$//[110]. In Fig.17 it can easily be seen that the pairs of the spin splitting peaks H_0^+, H_1^- due to smaller cross sections and $H_0^{+'}$, and $H_1^{-'}$ due to larger cross sections approaches each other as θ approaches the right angle ($\vec{H}$//[100]).

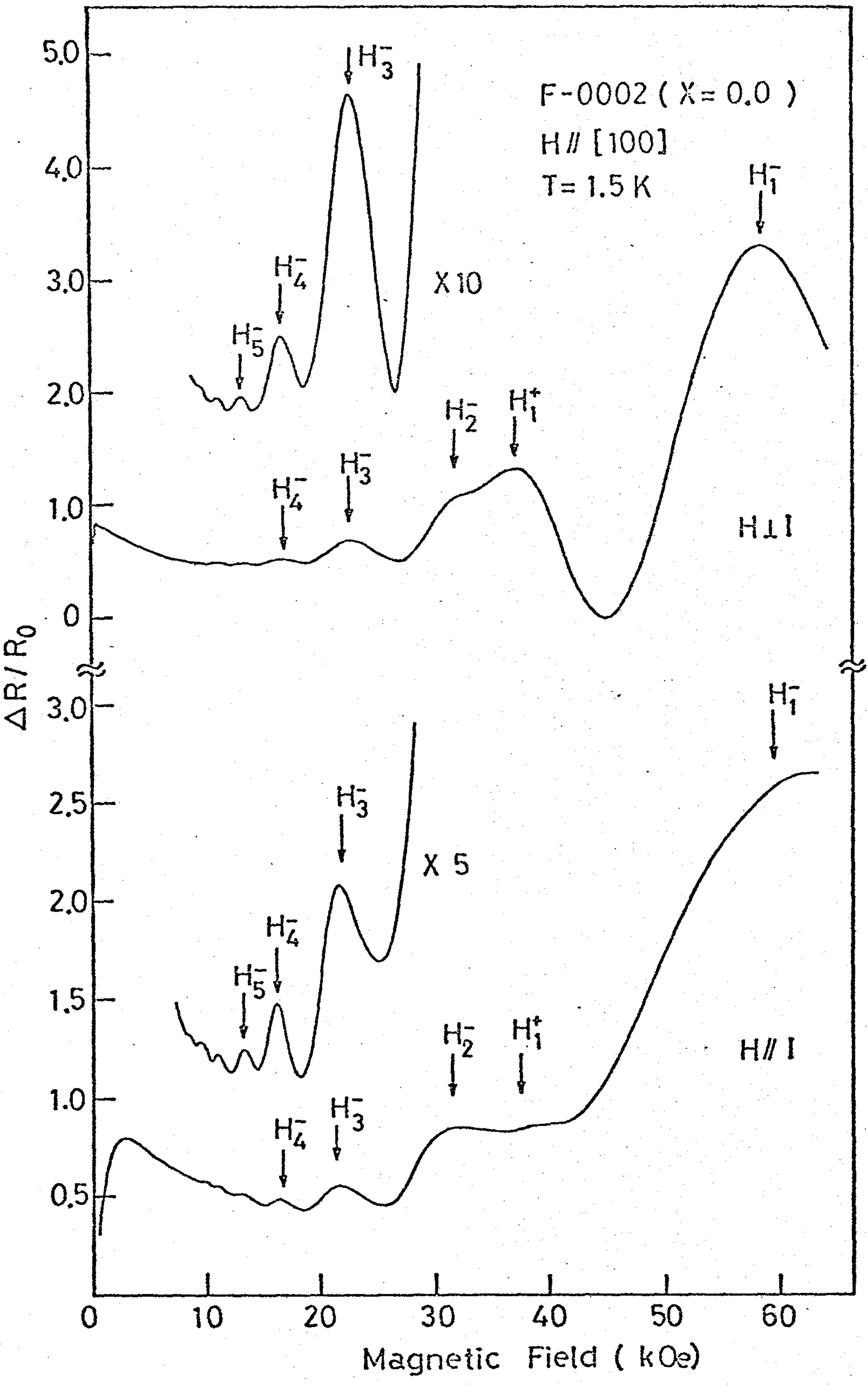

Fig.10 Recorder traces of transverse (upper part) and longitudinal (lower part) oscillatory magnetoresistance signal of PbTe as a function of magnetic fields. Applied fields are parallel to the [100] axis. Spin splitting peaks are indicated by the arrows.

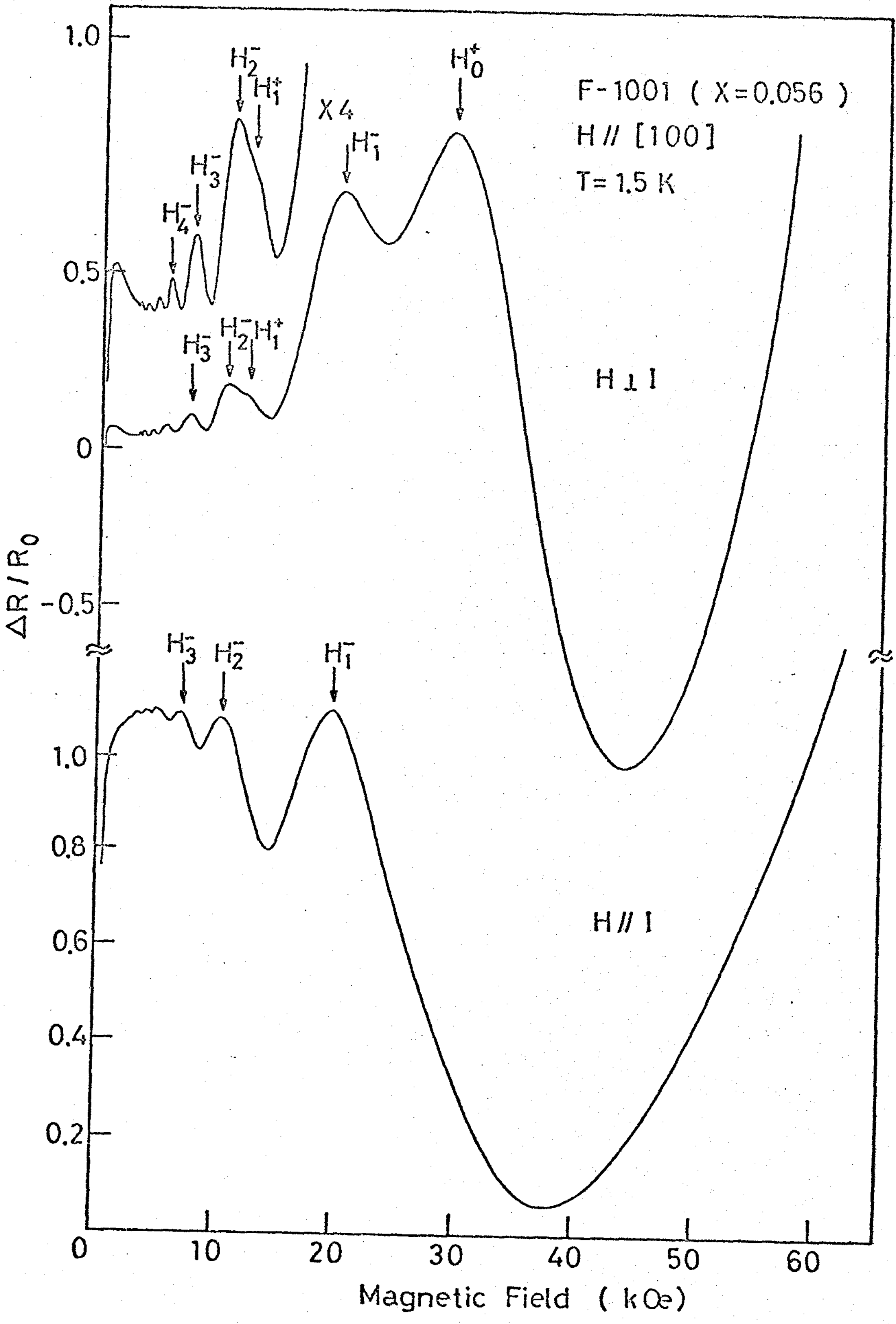

Fig.11 Recorder traces of transverse (upper part) and longitudinal (lower part) oscillatory magnetoresistance signal of $Pb_{1-x}Sn_xTe$ (x=0.056) as a function of magnetic fields. Applied fields are parallel to the [100] axis. Spin splitting peaks are indicated by the arrows.

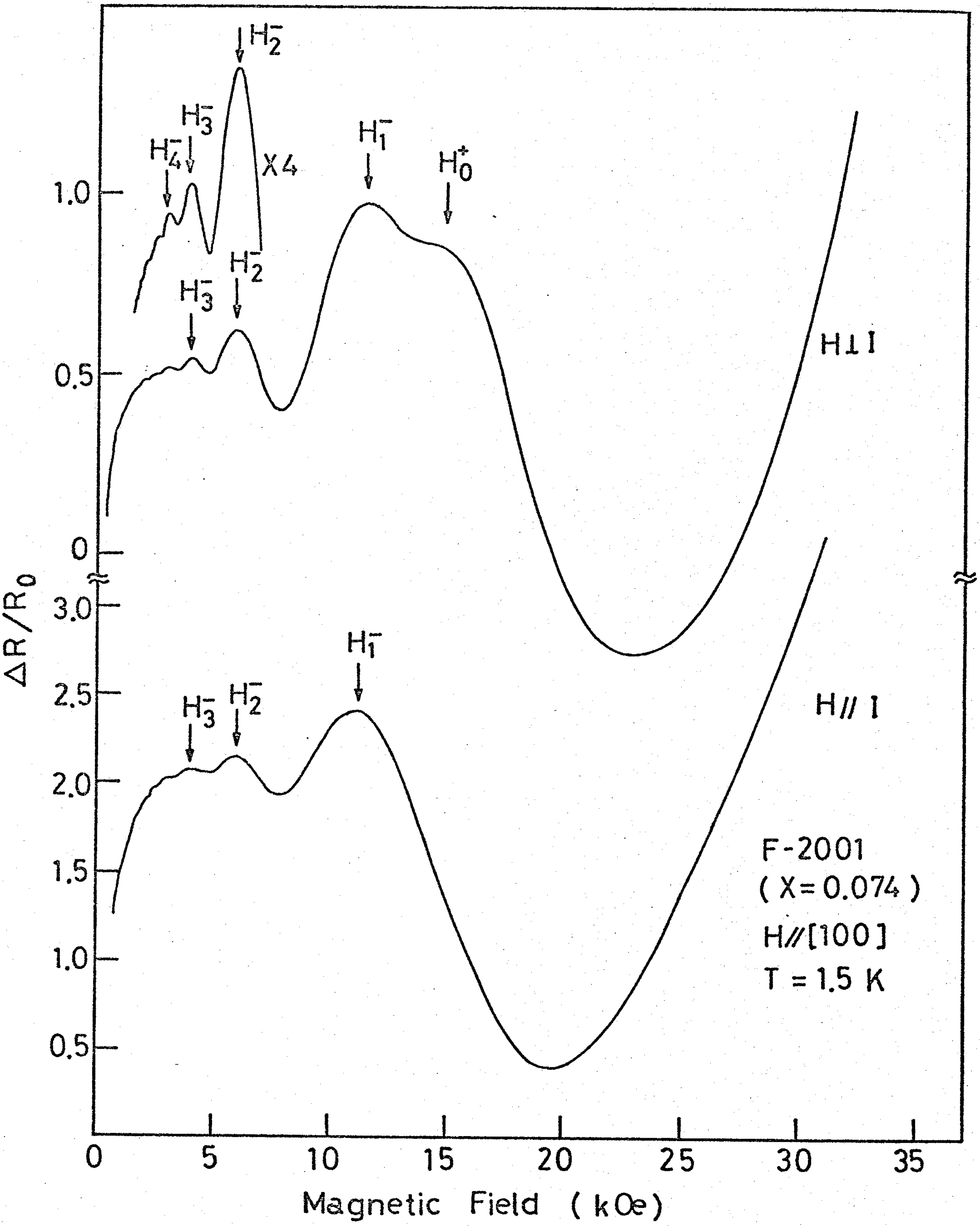

Fig.12 Recorder traces of transverse (upper part) and longitudinal (lower part) oscillatory magnetoresistance signal of $Pb_{1-x}Sn_xTe$ (x=0.074) as a function of magnetic fields. Applied magnetic fields are parallel to the [100] axis. Spin splitting peaks are indicated by the arrows.

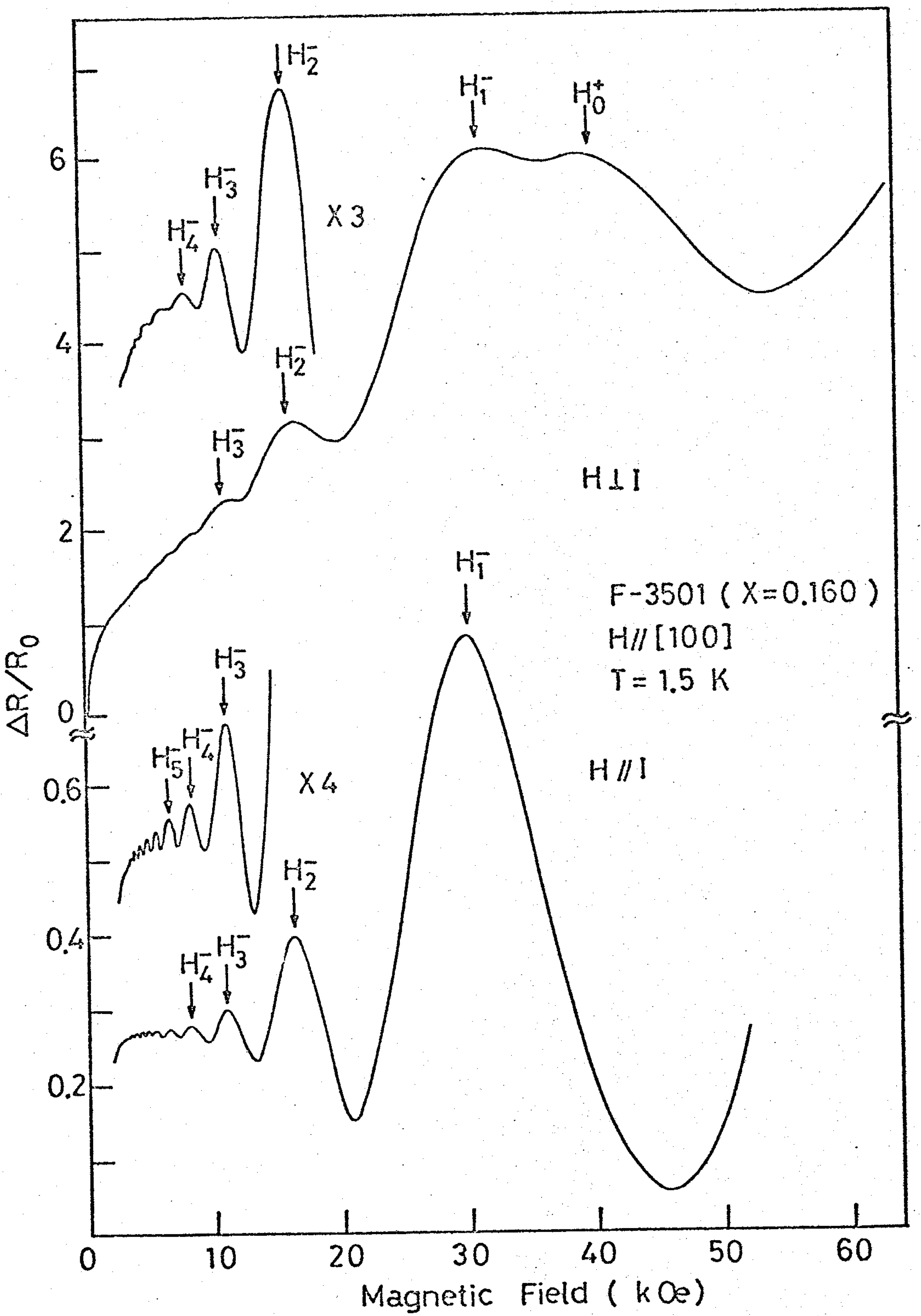

Fig.13 Recorder traces of transverse (upper part) and longitudinal (lower part) oscillatory magnetoresistance signal of $Pb_{1-x}Sn_xTe$ (x=0.160) as a function of magnetic fields. Applied fields are parallel to the [100] axis. Spin splitting peaks are indicated by the arrows.

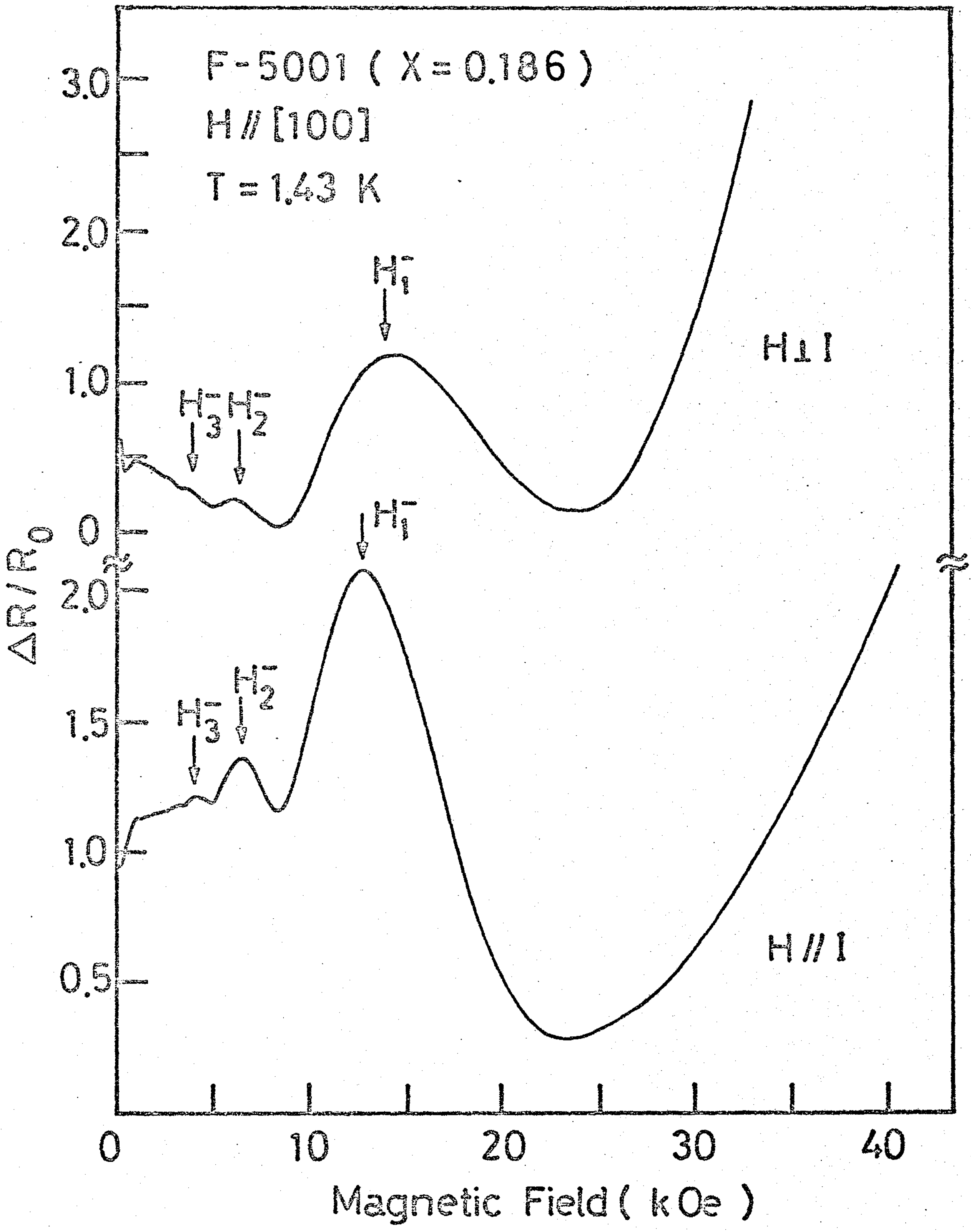

Fig.14 Recorder traces of transverse (upper part) and longitudinal (lower part) oscillatory magnetoresistance signal of $Pb_{1-x}Sn_xTe$ (x=0.186) as a function of magnetic fields. Applied fields are parallel to the [100] axis. Spin splitting peaks are indicated by the arrws.

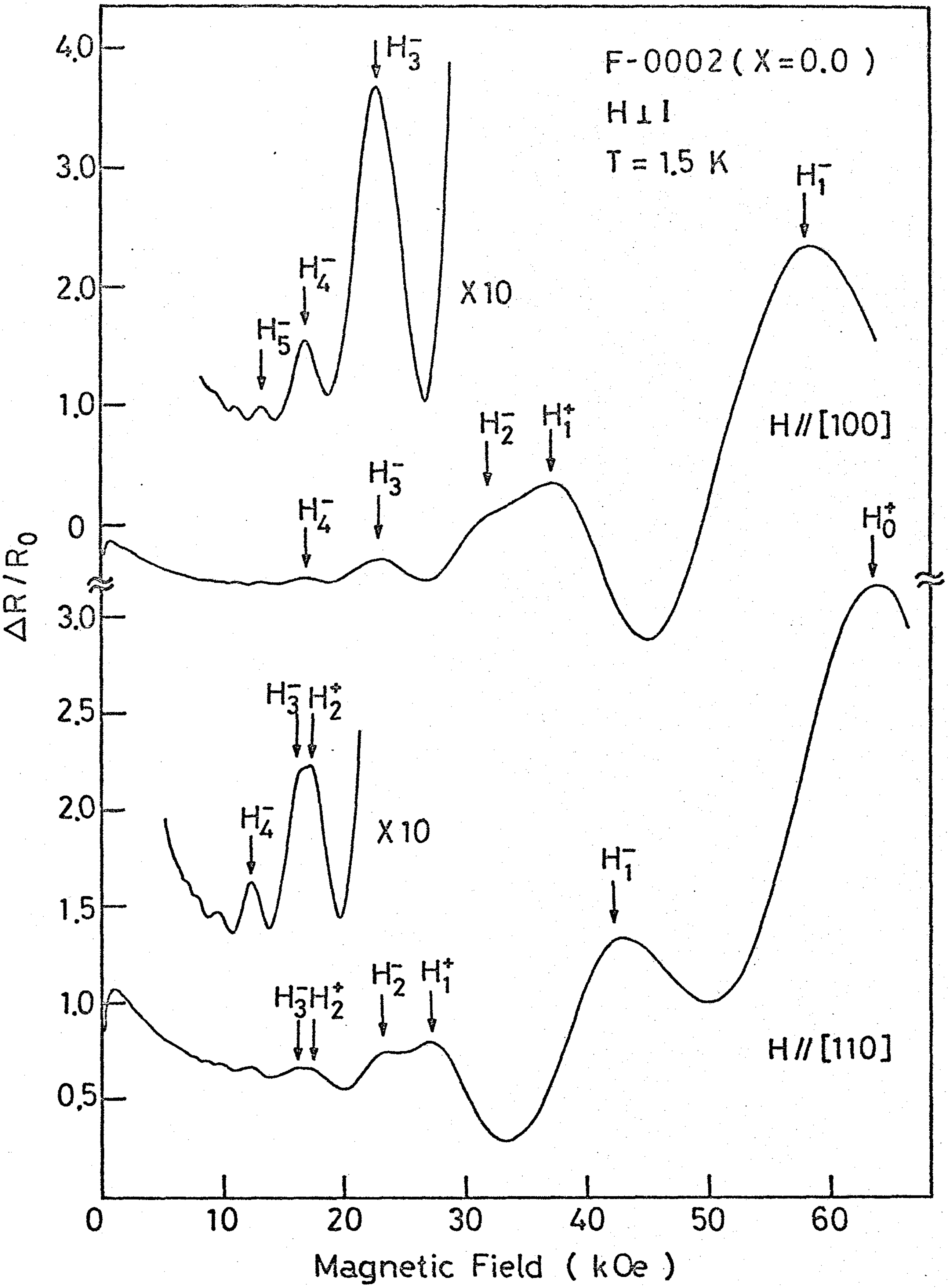

Fig.15 Recorder traces of transverse oscillatory magnetoresistance signal of PbTe as a function of magnetic fields. Applied fields are parallel to the [100] axis (upper part) and the [110] axis (lower part). Spin splitting peaks are indicated by the arrows.

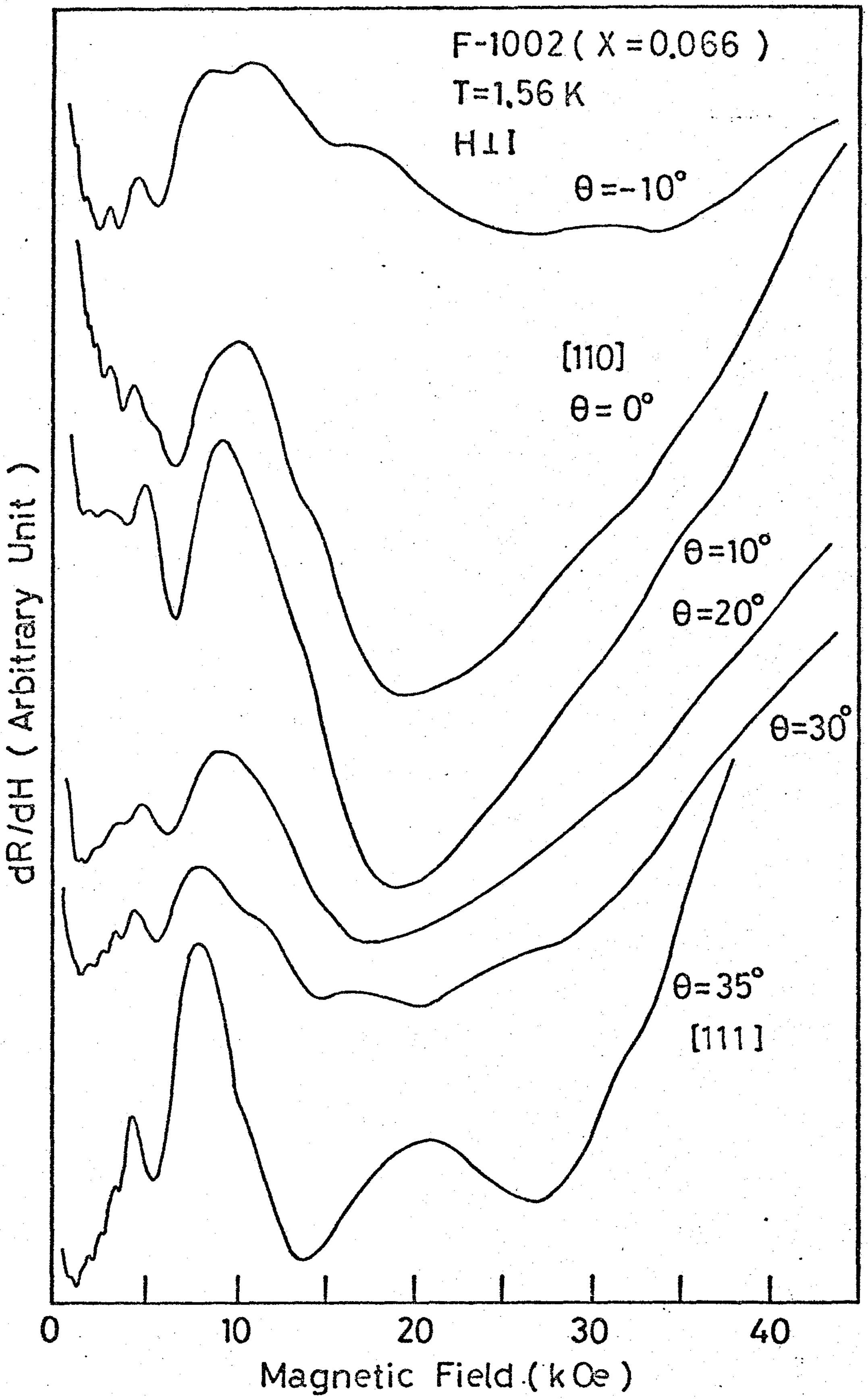

Fig.16,a Recorder traces of field derivatives of transverse oscilatory magnetoresistance signal for $Pb_{1-x}Sn_xTe$ (x=0.066) as a function of magnetic fields. Rotation plane is (110), and θ represents the rotation angle from the [110] direction.

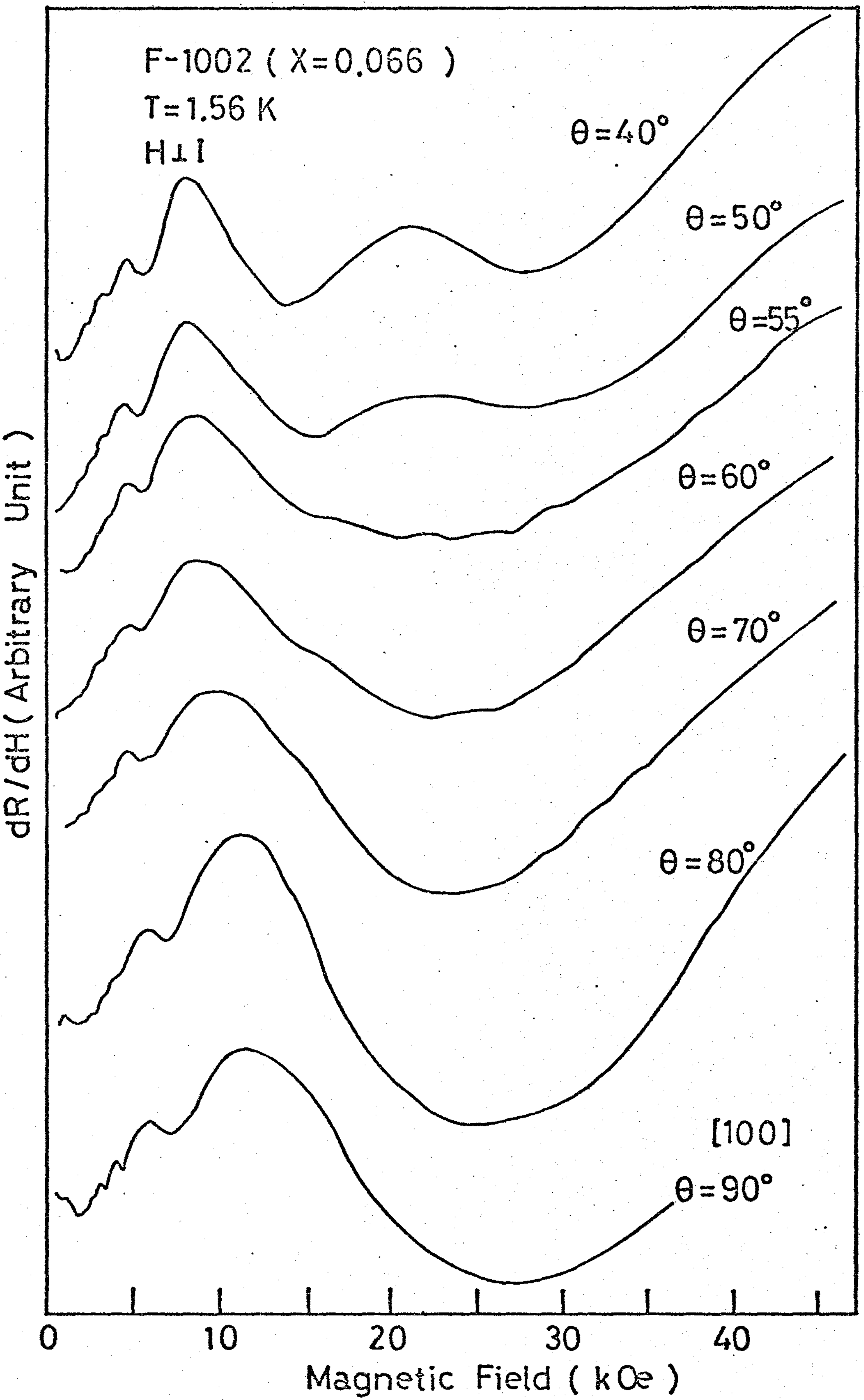

Fig.16,b Recorder traces of field derivatives of transverse oscillatory magnetoresistance signal for $Pb_{1-x}Sn_xTe$ (x=0.066) as a function of magnetic fields. Rotation plane is (110), and θ represents the rotation angle from the [110] direction.

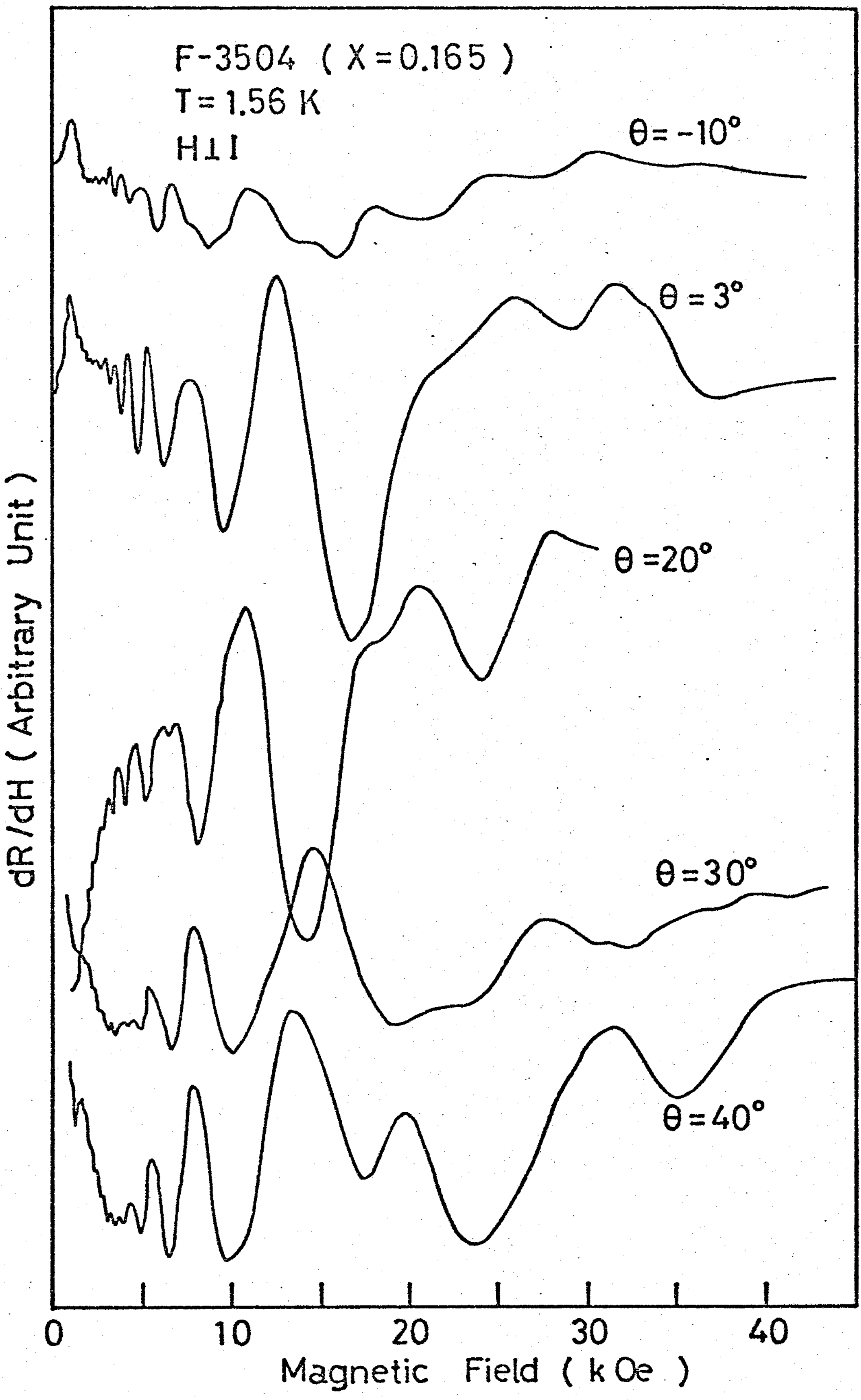

Fig.17,a Recorder traces of field derivatives of transverse oscillatory magnetoresistance signal for $Pb_{1-x}Sn_xTe$ (x=0.165) as a function of magnetic fields. Rotation plane is (100), and θ represents the rotation angle from the [100] direction.

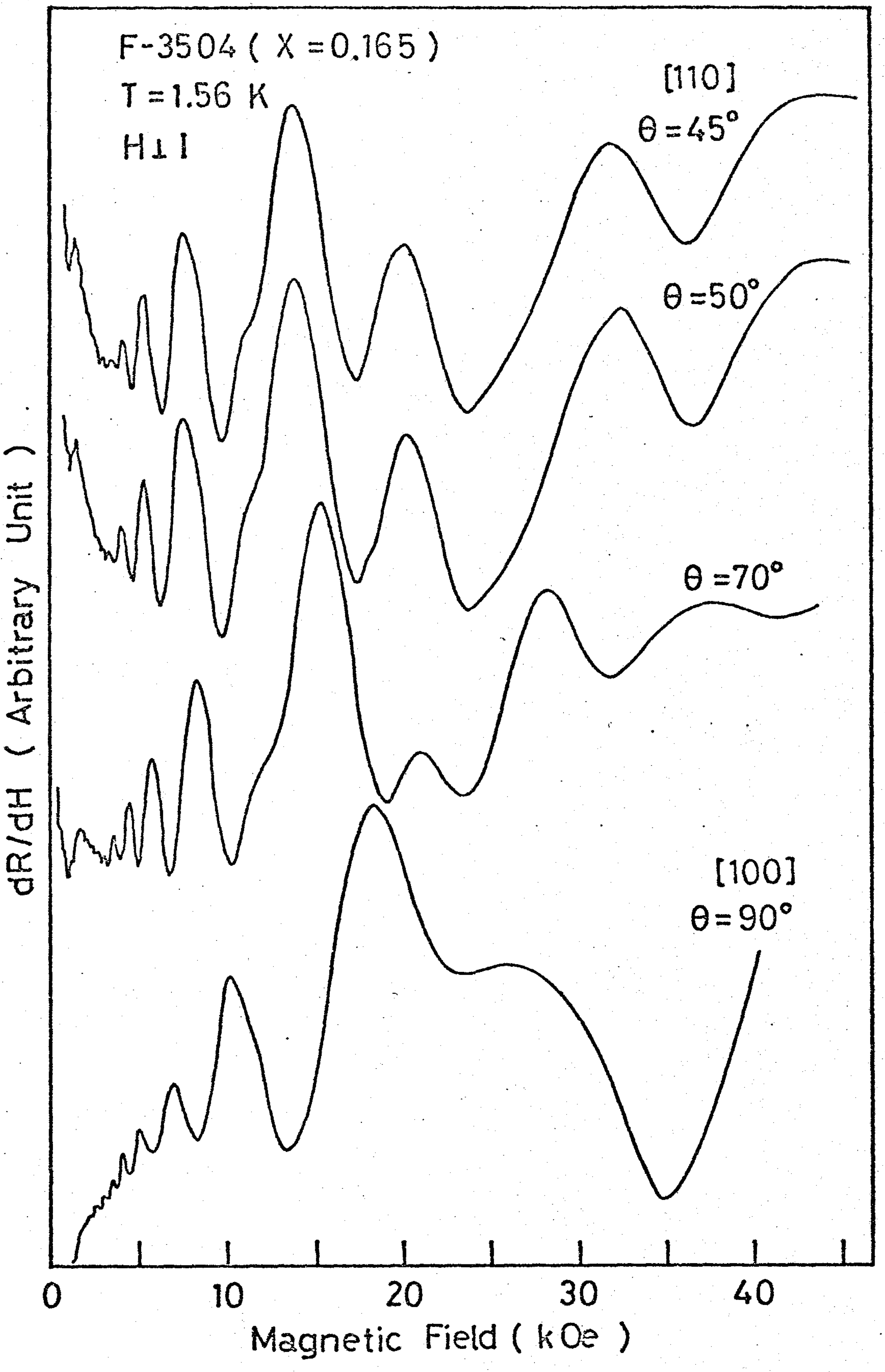

Fig.17,b Recorder traces of field derivatives of transverse oscillatory magnetoresistance signal for $Pb_{1-x}Sn_xTe$ (x=0.165) as a function of magnetic fields. Rotation plane is (100), and θ represents the rotation angle from the [100] direction.

VI. Analysis of Experimental Results

VI.1. Amplitude, Period, and Phase

From the expression in the last chapter, the amplitude of the oscillation at the fundamental frequency ($r=1$) at temperature T_1 is related to that at temperature T_2 by

$$\frac{A(T_1)}{A(T_2)} = \frac{T_1}{T_2} \cdot \frac{\sinh(2\pi^2 kT_2/\hbar\omega_c)}{\sinh(2\pi^2 kT_1/\hbar\omega_c)} \quad , \qquad \text{(VI.1,a)}$$

where $\omega_c = eH/m_c^* c$. Using eq.(VI.1,a), the cyclotron effective mass at the Fermi level can be obtained from the temperature and the field dependence of the envelope where the oscillations are sinsoidal. When $h\omega_c$ is small, the ratio of sinh functions can be approximated by exponential. However, in the present case, as $\hbar\omega_c$ is not sufficiently small, exact form of eq.(VI.1,a) is required. Eq.(VI.1,a) can be written as

$$\frac{A(T_1)}{A(T_2)} = y\,\frac{\sinh(X)}{\sinh(yX)} \quad , \qquad \text{(VI.1,b)}$$

where $X=2\pi^2 kT_2/\hbar\omega_c$, and $y=T_1/T_2$. For any fixed values of T_1 and T_2, the amplitude ratio $A(T_1)/A(T_2)$ can be calculated as a function of the magnetic field H. Taking the inversion of eq.(VI.1,b), we get X as a function of H. By plotting the experimentally obtained values of X as a function of 1/H, and drawing a best fit line passing through the origin, we can obtain the cyclotron effective mass from the slope which is proportional to the effective mass as follows,

$$m_c^* = \frac{e\hbar}{c}\,\frac{1}{2\pi^2 kT_2}\,\frac{X}{1/H} \; . \qquad \text{(VI.2)}$$

A typical example of the analysis is given in Fig.18. The excellent fit of the experimental points indicates that the sample is exactly parallel to the [100] direction, because deviations of points due to beats are not detected.

The spin splitting factor $\nu = m_c^* g/2m$ can be obtained from the spin splittings of the oscillatory peaks using the following equation,

$$\frac{m_c^* g}{2m} = \frac{(1/H)_{N+} - (1/H)_{N-}}{(1/H)_{N+} - (1/H)_{(N-1)+}} \quad ; \qquad (\text{ VI.3 })$$

where $(1/H)_{N\pm}$ means the peak positions corresponding to the $N\uparrow$ and $N\downarrow$ states. However, it is also possible to estimate ν independently from the field dependence of the amplitude of the TMR, by the use of the expression given by Roth and Argyres,[88] as follows:

$$A = \frac{\Delta\rho}{\rho_0} \frac{1}{\left(\frac{\hbar\omega_c}{\zeta_0}\right)^{1/2} \frac{X}{\sinh X}} = -\frac{1}{\sqrt{2}} \cos\left(\frac{2\pi\zeta}{\hbar\omega_c} - \frac{\pi}{4}\right) \cos(\pi\nu)\, e^{-2\pi^2 kT_D/\hbar\omega_c} \quad , \qquad (\text{ VI.4,a })$$

where $X = 2\pi^2 kT/\hbar\omega_c$. Taking the logarithums of eq.(VI.4,a), we get

$$\ln A' = \ln[-2\cos(\pi\nu)/\sqrt{2}] - 2\pi^2 kT_D/\hbar\omega_c \quad , \qquad (\text{ VI.4,b })$$

where A' is the envelope of A. The plots of $\ln A'$ against 1/H falls on a line whose spole gives the Dingle temperature and whose vertical intersept gives the value of $\cos(\pi\nu)$.

A typical example is shown in Fig.19. This method is applicable to the case when the spin splittings of oscillatory peaks are not remarkable. The values of ν obtained from above method closely coinside with those obtained from the spin splittings of oscillatory peaks. This fact seems to indicate that the doubling of the oscillatory peaks observed in the TMR comes from the spin-Zeeman splitting of the Landau levels. The values of ν thus obtained are close to unity and moreover more closely approach unity with decreasing E_G. This indicates that the interactions between the conduction and the remote bands are second order compared with the direct conduction and valence band interaction. Therefore the system can be approximated by the two-band model, where the spin splitting $g\mu_B H$

is equal to the Landau level separation $\hbar\omega_c$,[85)] if the free electron contribution is ignored.

Typical examples of the analysis for the SdH period and the spin splitting are given in Fig.20. The lower part is the SdH signal of PbTe as a function of 1/H, when $\vec{H}$ // [110]. The spin splitting peaks are indicated by the arrows according to the assignment that the spin splitting factor ν is greater than unity. The upper part represents the 1/H positions of the spin splitting peaks versus the Landau quantum number, taken from the lower part of the figure. The period is given by the slope, whereas the spin splitting is given by the vertical separation of both the H_N^+ and H_N^- series.

The values of ν experimentally obtained are shown in Fig.21 as a function of the alloy composition.

The evidence of the large g-factor is given by the analysis of the background phase shift of the oscillation. For band electrons, eq.(II.9,a) and (II.9,b) becomes

$$\rho = \rho_o \left[1 + \sum_{r=1}^{\infty} b_r \cos(rc\hbar A_{ex} H^{-1}/e - 2\pi\gamma r - \pi/4) \right] , \qquad (\text{VI.5,a})$$

where

$$b_r = \frac{1}{r^{1/2}} \left(\frac{\hbar\omega_c}{2\zeta} \right)^{1/2} \frac{2\pi^2 rkT/\hbar\omega_c}{\sinh(2\pi^2 rkT/\hbar\omega_c)} e^{-2\pi^2 rkT_D/\hbar\omega_c} \cos(\pi\nu r) , \qquad (\text{VI.5,b})$$

A_{ex} is the extremal cross section, and γ is a constant phase factor which is 1/2 for free electrons. The cosine functions in the above expressions are

$$\cos(rc\hbar A_{ex} H^{-1}/e - \phi) , \qquad (\text{VI.6,a})$$

and the phase is

$$\phi = 2\pi\gamma r + \pi/4 + \delta , \qquad (\text{VI.6,b})$$

where δ is the back ground phase shift of the oscillation. When the back ground phase shift δ is assumed to be either 0 or π, which is determined by the term $\cos(\pi\nu r)$ in eq.(VI.5,b) and thus influenced by the size of the g factor. From eq.(VI.6,a), the positions of maxima and minima of the SdH oscillation are

$$1/PH - \phi/2\pi = j \qquad (\text{ maxima }) , \qquad (\text{ VI.7,a })$$

and

$$1/PH - \phi/2\pi = j + 1/2 \quad (\text{ minima }) , \qquad (\text{ VI.7,b })$$

where j is the integer and $P^{-1}= c\hbar r A_{ex}/e$. When γ is 1/2, the term $2\pi\gamma r$ in eq.(VI.5,a) is omitted, and $(-1)^r$ is introduced in front of eq.(VI.5,b). Plotting the integral multiples of one-half against the 1/H positions of the both extrema, and then fitting j, we obtain the value of $\phi/2\pi$, comparing which value of δ gives the γ closest to 1/2, when δ is assumed to be either 0 or π, using eqs.(VI.6,b), (VI.7,a), and (VI.7,b). In other words, we search δ which is assumed to be either 0 or π, that gives the γ closest to 1/2, varying the integer j. An example of the analysis is given in Fig.22 for the sample F3504 when $\vec{H} \,//\, \vec{I}$ (LMR). The best fit value is $\delta=\pi$ and $\gamma=0.515$. If we assume $\delta=0$ in this case, the same analysis gives $\gamma=1.015$, and letting j instead of j+1 gives $\gamma=0.015$ for $\delta=0$, or $\gamma=-0.485$ for $\delta=\pi$. Similar analysis for other samples also give the nearly π phase shift, as in Bi.(99) Thus, this analysis also indicates the large g-value of $Pb_{1-x}Sn_xTe$.

VI.2. Angular Dependence of Extremal Cross Sections

For the study of the anisotropy of the electron Fermi surface of $Pb_{1-x}Sn_xTe$, the transverse oscillatory magnetoresistance were measured rotating the samples in the (100) or (110) plane, as described in the last chapter. The upper and lower part of Fig.23 show respectively the rotation plane relative to the (100) and (110) planes, and θ represents the rotation angle of the samples from [110] and [110] directions, respectively. Let α be the angle between the magnetic field direction and the [111] direction. For the [111] ellipsoids, the relations of α to θ, and of the period to θ are given in Appendix A. The upper and lower part of Fig. 24 respectively show the experimentally obtained periods as a function of θ. If the shape of the Fermi surface is nearly ellipsoidal whose major axis is in the [111] direction, the maximum cross section appears at θ=0° or 55° when the sample is rotated in the (110) plane, and θ=45° when the sample is rotated in the (100) plane.

For the accurate determination of the shape of the Fermi surface or the correct determination of the carrier number contained in the ellipsoids, the maximum cross section is required which gives rise to the oscillation of small amplitude and short period, so that we employ the field modulation technique for the accurate measurements of the largest cross section.

When the sample is rotated in the (110) plane, three different cross sections are observed, and these are given as A, B, and C in the upper part of Fig. 24, and when the sample is rotated in the (100) plane, two different cross sections are observed and are given as A, and B in the lower part of Fig. 24. In Fig. 25, the polar plots of the reciprocal of the period, which is proportional to the extremal area and hence proportional to diameter of the ellipsoidal Fermi surface, are given for several samples as a function of θ, the angle between $\vec{H}$ and [111] direction. The solid curves in the figures represent the perfect ellipsoidal surface with the best fit values of n and K. The very good fit of the experimental points to the solid curve indicates that the Fermi surface of electrons in $Pb_{1-x}Sn_xTe$ with relatively small x-value and low carrier density, is [111] ellipsoid, and no deviation from the perfect ellipsoid is appreciable, if we take the experimental error into account. The results also indicate that the anisotropy K becomes large with increasing x-value, as in the hole surface.[38,62] However, the dependence of K upon the carrier concentration is not accurate. In addition, the carrier concentration has also been determined from the high field Hall coefficient. The carrier concentration thus determined closely coinsides with that determined from the volume of the ellipsoids, and this indicates that there are four ellipsoids.

VI.3. Band Parameters

The band parameters such as the effective masses, K's, the spin splitting factor ν's, or the electronic g-factors as a function of alloy composition were obtained by the above methods. These values are listed in Table I.

From these values, we can determine the momentum matrix elements or the energy gaps which describe the energy band structure near the band edge by fitting the experimentally obtained values to the band theory. The detailed procedure is given in the next chapter.

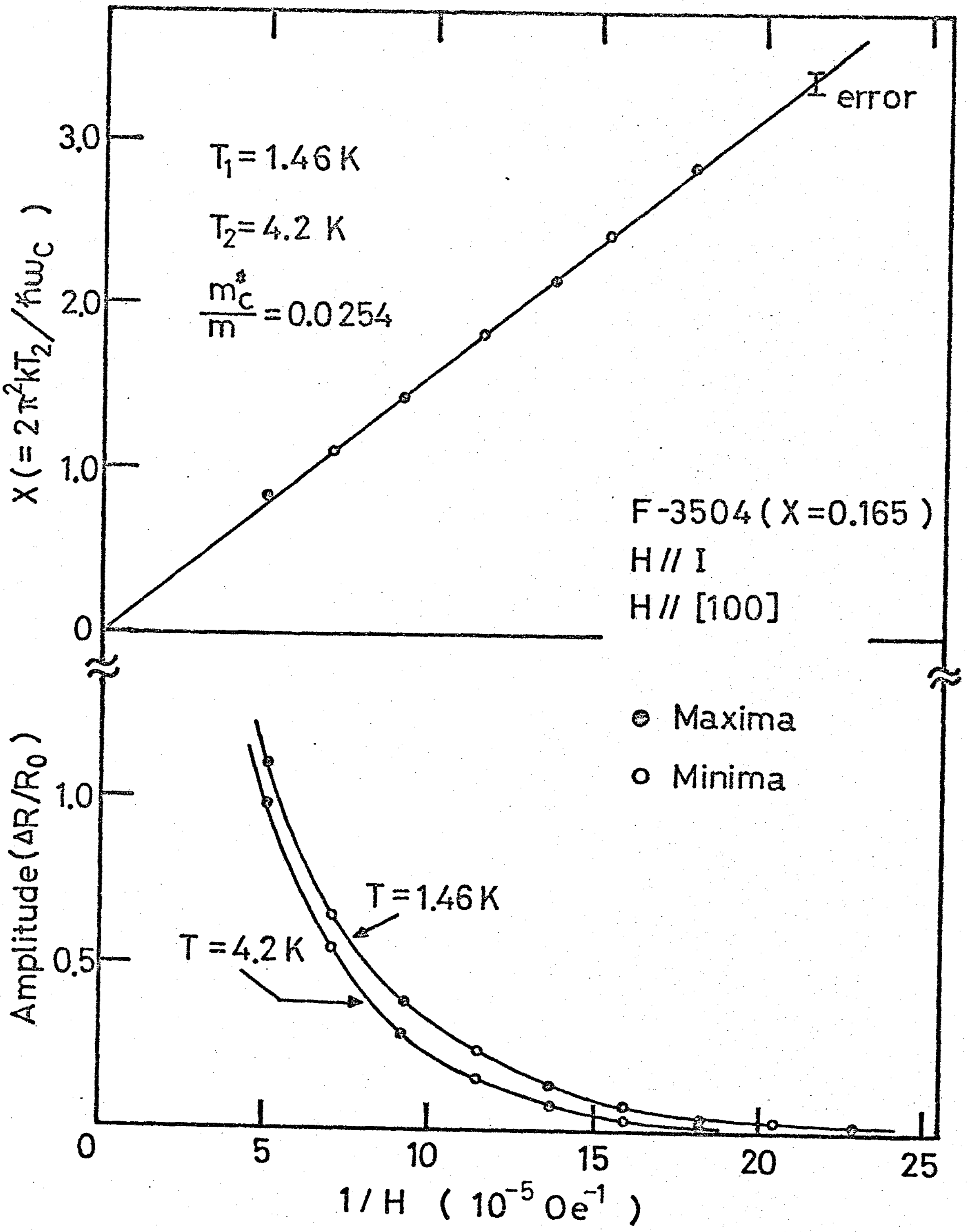

Fig.18 The lower part represents the amplitude (envelope) of longitudinal oscillatory magnetoresistance of $Pb_{1-x}Sn_xTe$ (x=0.165), as a function of 1/H, at temperatures 4.2 K and 1.46 K, when $\vec{H}$ // [100]. The upper part represents the values of $X(=2\pi^2 kT_2/\hbar\omega_c)$ obtained from the lower part of the figure, as a function of 1/H.

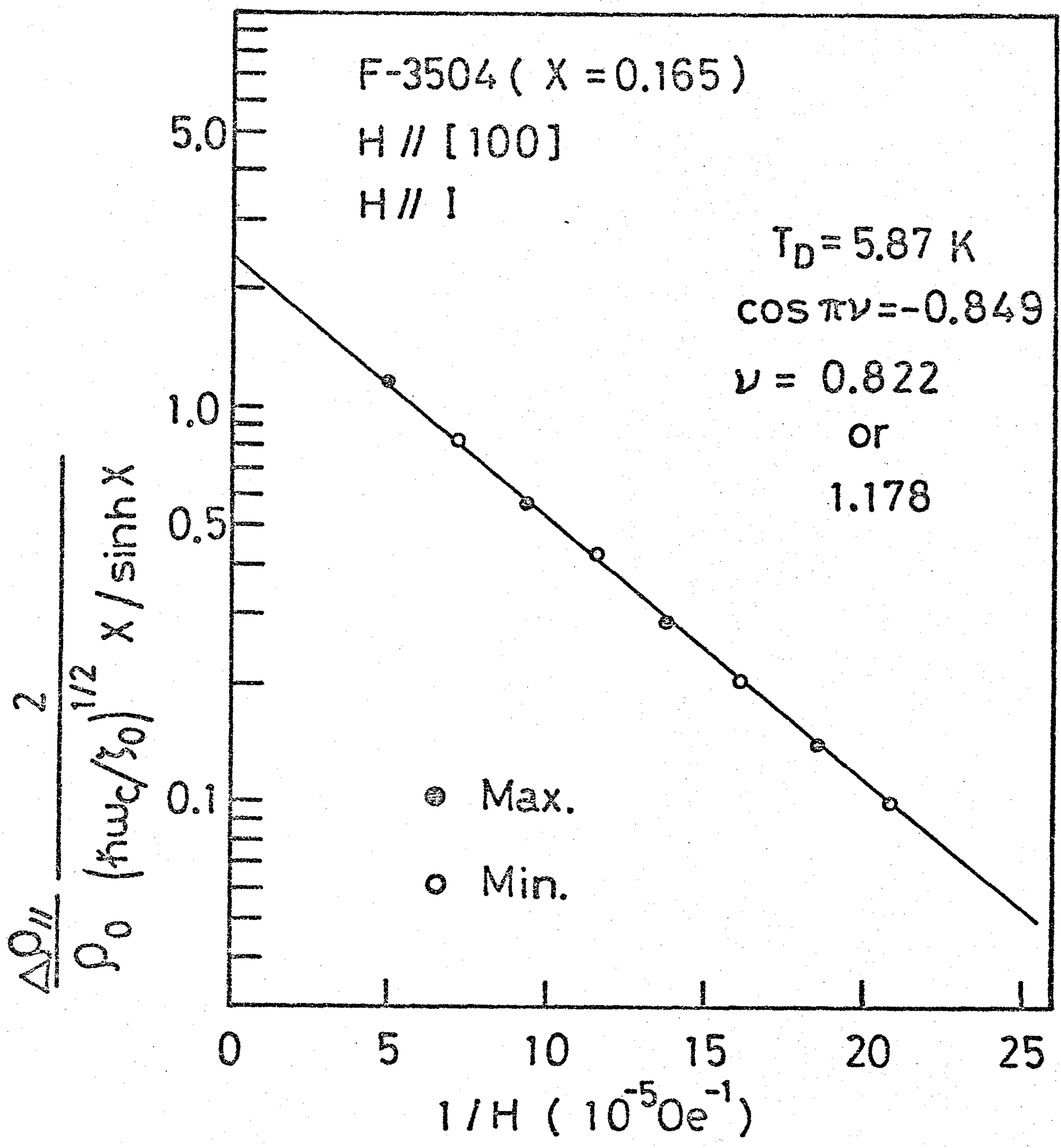

Fig.19 $\frac{2\Delta\rho}{\rho_0}(\hbar\omega_c/\zeta_0)^{-1/2}\frac{X}{\sinh X}$ as a function of 1/H for $Pb_{1-x}Sn_xTe$(x=0.165), when $\vec{H}$ // [100]. The slope gives the Dingle temperature T_D=5.87 K, and the vertical intercept gives cos(πν)=-0.849.

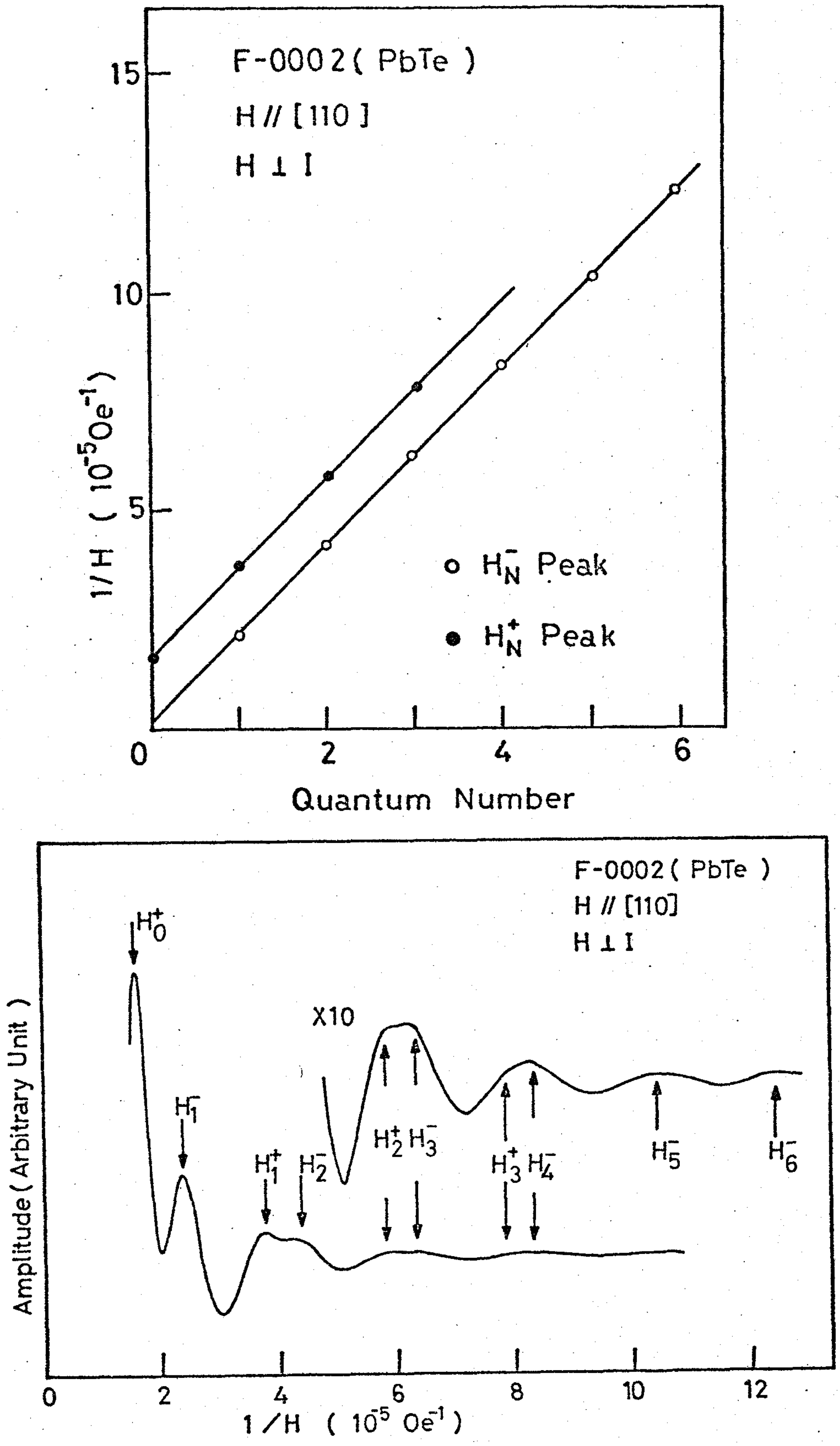

Fig.20 The lower part is the SdH signal of PbTe as a function of 1/H, when $\vec{H}$ // [100]. The spin splitting peaks are indicated by the arrows. The upper part is the 1/H peak positions versus Landau quantum number, taken from the lower part of the figure.

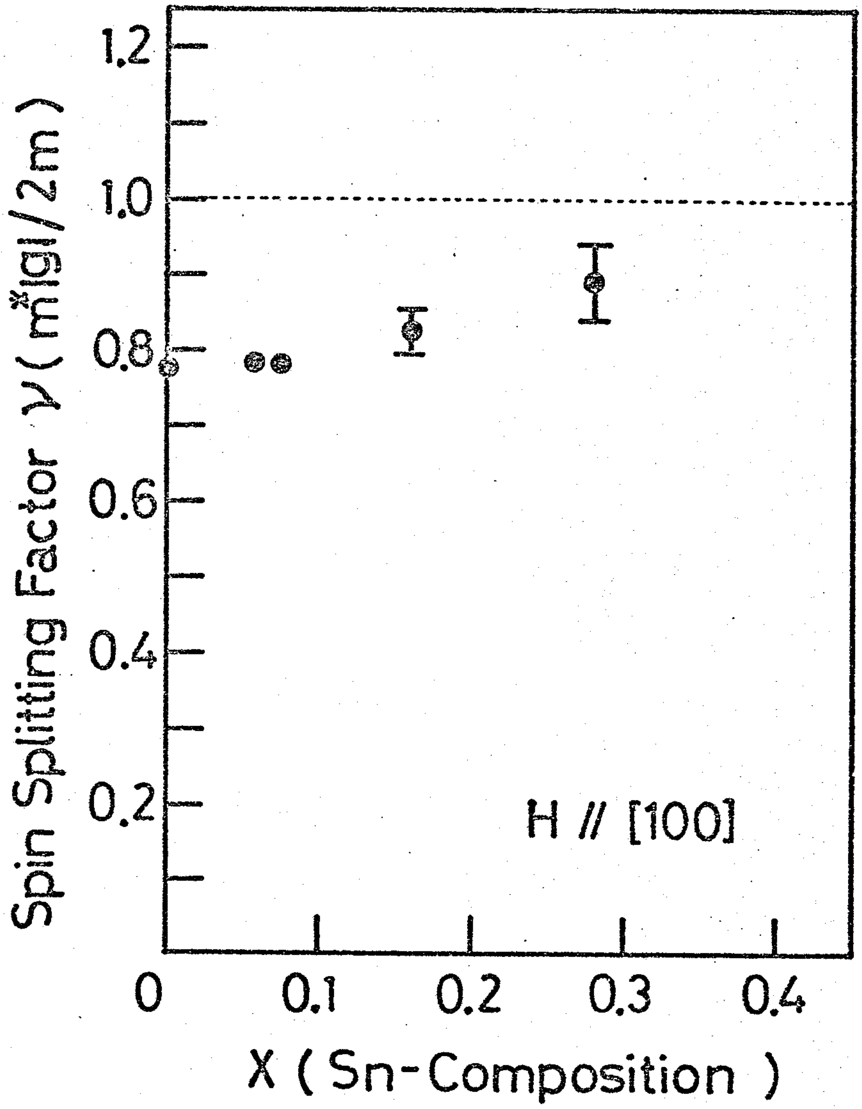

Fig.21 Spin splitting factor $\nu(= m_c^*|g|/2m)$ obtained from the oscillatory peaks of the spin splittings in the TMR, as a function of alloy composition x. The magnetic field is parallel to the [100] direction.

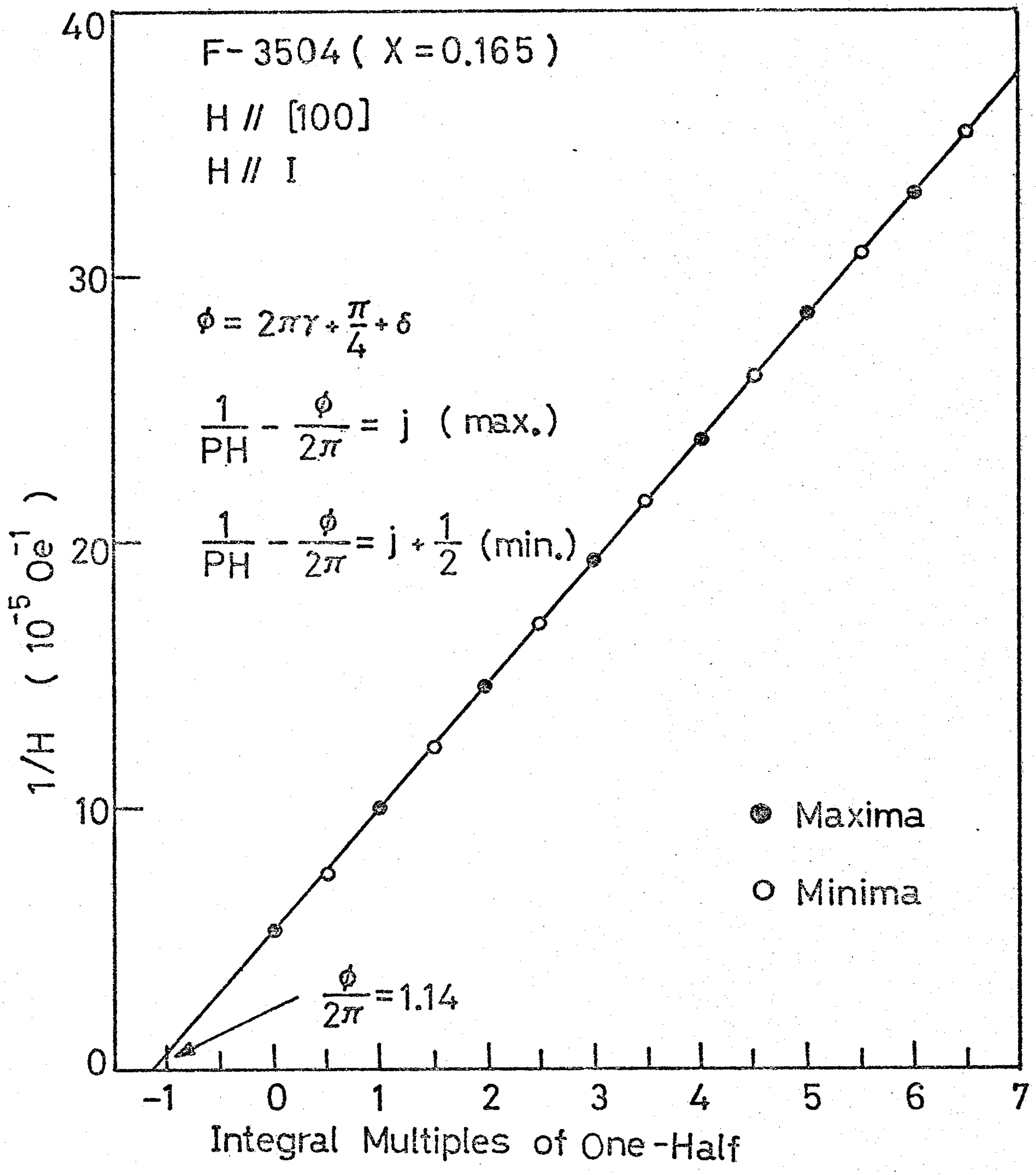

Fig.22 Integral multiples of one-half versus 1/H positions of maxima and minima of LMR of $Pb_{1-x}Sn_xTe$(x=0.165). Assuming that the phase shift γ=0 or π, and labeling the ordinate to obtain an intercept which gives the γ closest to 1/2: its *free-electron* value. In this case δ and γ becomes, δ=π, and γ=0.515.

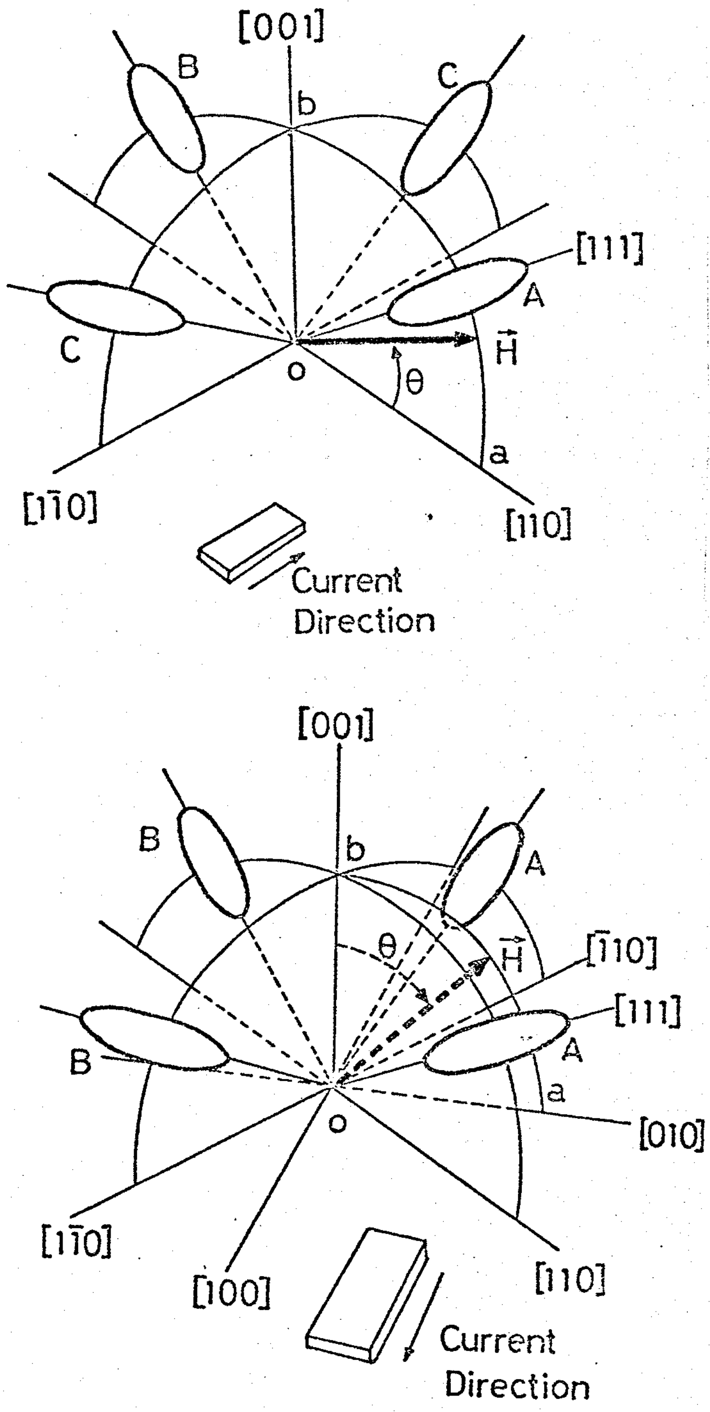

Fig.23 Four [111] ellipsoidal pockets of $Pb_{1-x}Sn_xTe$. The upper part represents the configuration when the magnetic field is rotated in the (110) plane. The lower part represent the configuration when the magnetic field is rotated in the (100) plane.

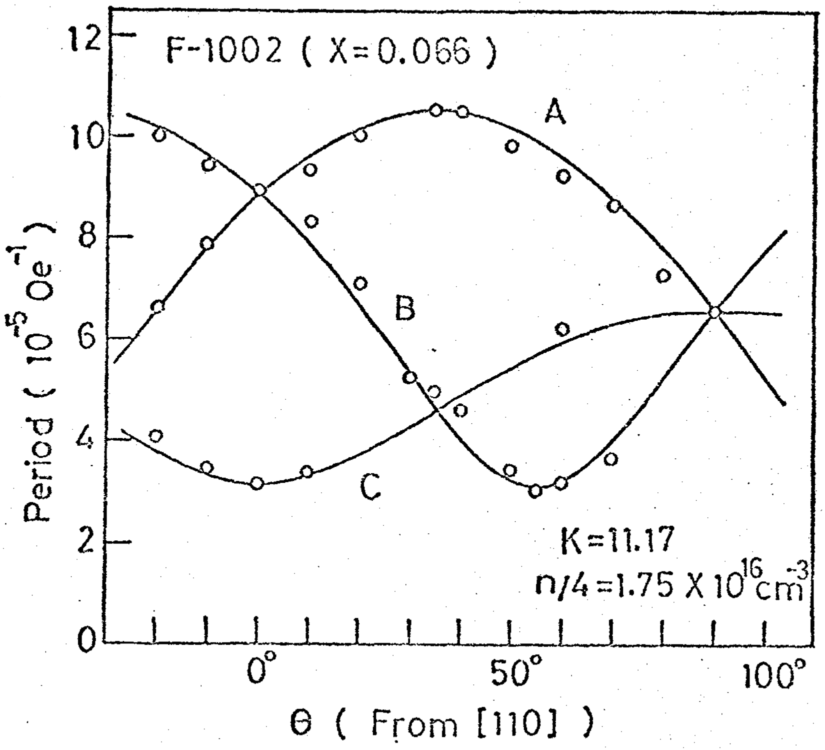

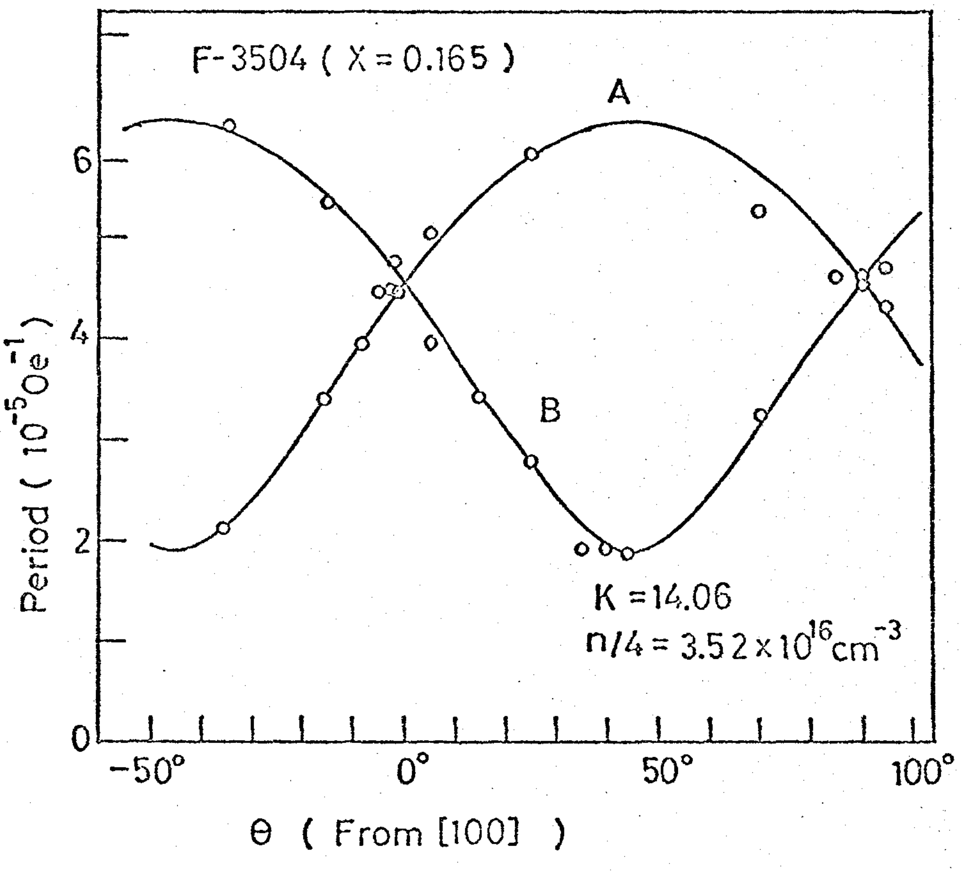

Fig. 24 Plots of angular dependence of SdH period (open circles) for $Pb_{1-x}Sn_xTe$ (x=0.066), when the magnetic field is rotated in the (110) plane (upper part), and for $Pb_{1-x}Sn_xTe$(x=0.165), when the magnetic field is rotated in the (100) plane (lower part). The solid curves represent the best fit ellipsoids.

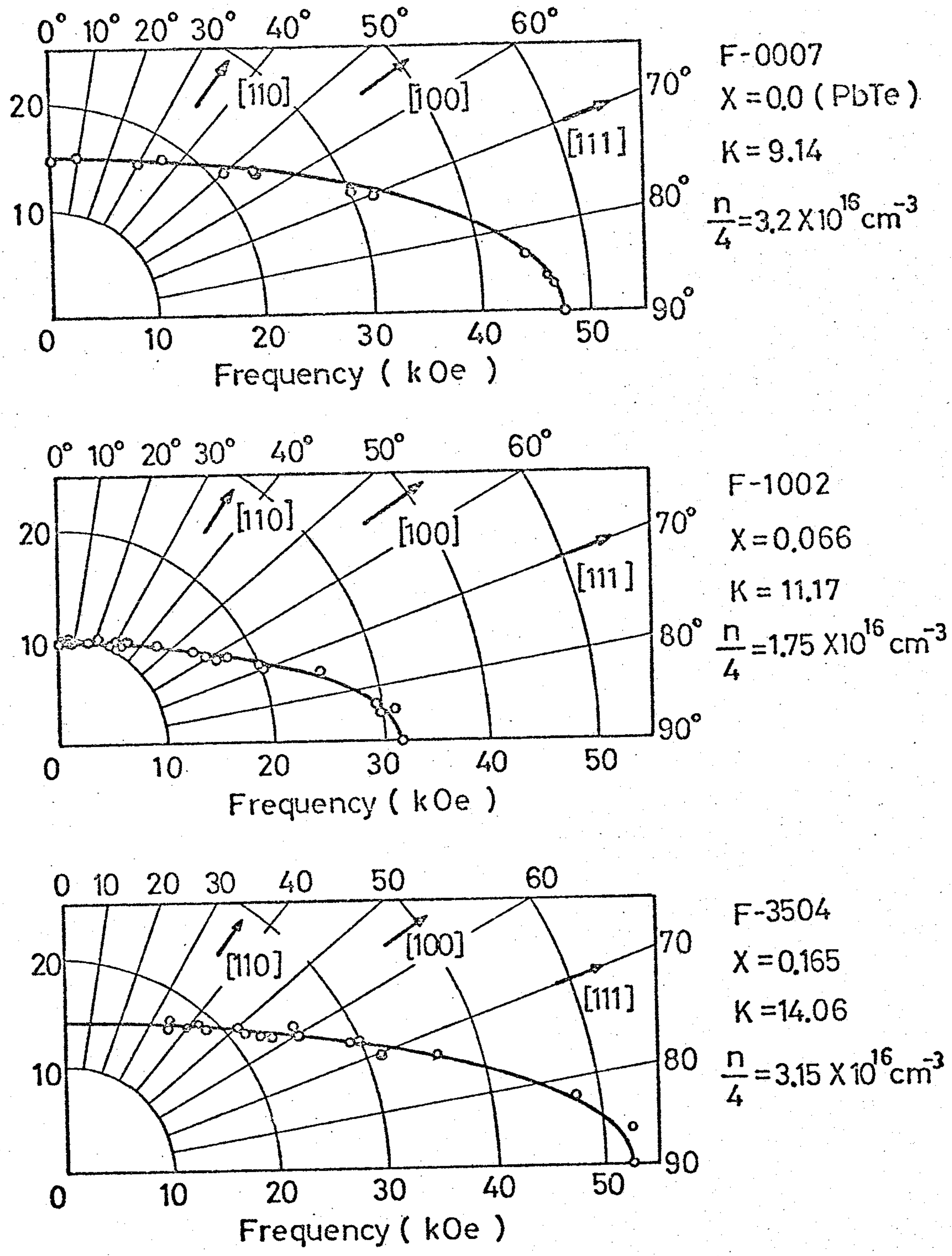

Fig. 25 Polar plots of frequencies (period^{-1}) of SdH oscillation for $Pb_{1-x}Sn_xTe$ alloys, x=0.0 (upper), x=0.066 (middle), and x=0.165 (lower). The open circles represent the experimental data, whereas the solid curves represent the best fit ellipsoids. These shpes are proportional to the shape of the Fermi surface.

Table I. The experimentally obtained band parameters of n-type $Pb_{1-x}Sn_xTe$ alloys.

Sample #	x-value	n (cm^{-3})	K	.Effective Mass	ν (g-value)
F0002	0.0	5.6×10^{17}	9.16	[100] 0.0430 [110] 0.0328 [111] 0.0275	[100] 0.774 (36) [110] 0.720 (44)
F0007	0.0	1.28×10^{17}	9.14	[111] 0.0244	--
F1001	0.056	1.18×10^{17}	10.46	[100] 0.0291 [111] 0.0183	[100] 0.78 (53.6) [110] 0.762 (52.5)
F1002	0.066	7.01×10^{16}	11.17	[110] 0.0213 [111] 0.0175	[100] 0.77 (72)
F2001	0.074	7.24×10^{16}	10.5	[100] 0.0270 [111] 0.0170	
F3501	0.160	2.48×10^{17}	12.5	[100] 0.0281 [110] 0.0213 [111] 0.0178	
F3504	0.165	1.41×10^{17}	14.06	[100] 0.0254 [111] 0.0157	[100] 0.822 (64.7)
F5001	0.186	7.20×10^{16}	14	[100] 0.0194 [111] 0.0120	
F7001	0.278	9.9×10^{17}	--	[100] 0.0279	[100] 0.89 (63.8)

VII. Theoretical Consideration

VII.1. $\vec{k}\cdot\vec{p}$ Band Models

As we have mentioned previously, both conduction and valence band extrema of $Pb_{1-x}Sn_xTe$ are located at the L-point and their separation in energy is very small, and varies with SnTe composition. This behavior is understood from Fig.26 as a relativistic effect of heavy element lead. In $Pb_{1-x}Sn_xTe$, six doubly degenerate bands are piled up around the Fermi level and three of which are the conduction, and remaining three are the valence bands. The other remote bands are well separated at the L-point. From the results of pseudo-potential calculation by Bernick and Kleinman[79] upon PbTe and SnTe, the energy variation with SnTe composition of these six bands are represented schematicly in Fig.27, assuming a linear variation of energy with composition. It can be easily noticed that the conduction and valence band are separated by an extremely small forbidden gap and the other four bands are largely separated.

Thus at first, we consider the two band model: we consider only a pair of bands.

A. Two Band Model

The wave functions which diagonarize the Hamiltonian including the spin-orbit interaction were given by Mitchel and Wallis.[83] After the notation of Mitchel and Wallis, the wave functions describing the L_6^- and L_6^+ levels are

$$
\begin{aligned}
|L_6^-\downarrow> &= \cos\theta^-\ Z\downarrow + \sin\theta^-\ X_-\uparrow ,\\
|L_6^-\uparrow> &= \cos\theta^-\ Z\uparrow - \sin\theta^-\ X_+\downarrow ,\\
|L_6^+\downarrow> &= i\ \cos\theta^+\ R\downarrow + \sin\theta^+\ S_-\uparrow ,\\
|L_6^+\uparrow> &= -i\ \cos\theta^+\ R\downarrow - \sin\theta^+\ S_+\uparrow ,
\end{aligned}
\qquad (\text{VII.1})
$$

where

$$X_{\pm} = (X \pm iY)/\sqrt{2} \quad ,$$

$$S_{\pm} = (S_X \pm iS_Y)/\sqrt{2} \quad .$$

In the above expression, the spin functions ↑ and ↓ refer to the eigenstates of s_z in the coordinate system with z along [111] axis, x along $[\bar{1}\bar{1}2]$, and y along $[1\bar{1}0]$. The spatial parts have the following transformation properties about the site of metal nucleus: R is s-like, $X_{\pm}$ and Z are p-like, and $S_{\pm}$ transform like atomic d-functions with $m_z=\pm 1$, and $\cos\theta^{\pm}$ and $\sin\theta^{\pm}$ are thespin-orbit mixing parameters.

The band structure in the vicinity of L-point can be calculated by $\vec{k}\cdot\vec{p}$ perturbation theory. Assuming that the wave functions and the energy at the L-point are exactly known, for usual one-electron Hamiltonian

$$H = \frac{1}{2m}(\vec{p} + e\vec{A}/c)^2 + V(\vec{r}) + \frac{\hbar}{m}\vec{k}\cdot\vec{p} + \mu_B\vec{H}\cdot\vec{\sigma} \ , \qquad (\text{VII.2})$$

the effective Hamiltonian operator describing the quasi-degenerate conduction and valence bands can be written as a 4x4 matrix as follows,

$$\hat{H}_{\mathrm{eff}} = \begin{array}{cccc}
|L_6^-\uparrow > & |L_6^-\downarrow > & |L_6^+\uparrow > & |L_6^+\downarrow > \\
\left(\begin{array}{c} \frac{E_G}{2} + \frac{\hbar^2}{2m}(k_x^2+k_y^2+k_z^2) \\ +\mu_B H_z(\cos^2\theta-\sin^2\theta^-) \end{array}\right. & \mu_B\cos^2\theta^-(H_x-iH_y) & \frac{\hbar}{m}P_{\parallel}k_z & \left.\frac{\hbar}{m}P_{\perp}(k_x-ik_y)\right) \\
\left(\mu_B\cos^2\theta^-(H_x+iH_y)\right. & \begin{array}{c} \frac{E_G}{2m} + \frac{\hbar^2}{2m}(k_x^2+k_y^2+k_z^2) \\ -\mu_B H_z(\cos^2\theta^- -\sin^2\theta^-) \end{array} & \frac{\hbar}{m}P_{\perp}(k_x+ik_y) & \left.-\frac{\hbar}{m}P_{\parallel}k_z\right) \\
\left(\frac{\hbar}{m}P_{\parallel}k_z\right. & \frac{\hbar}{m}P_{\perp}(k_x-ik_y) & \begin{array}{c} -\frac{E_G}{2} + \frac{\hbar^2}{2m}(k_x^2+k_y^2+k_z^2) \\ +\mu_B H_z(\cos^2\theta^+-\sin^2\theta^+) \end{array} & \left.-\mu_B\cos^2\theta^+(H_x-iH_y)\right) \\
\left(\frac{\hbar}{m}P_{\perp}(k_x+ik_y)\right. & -\frac{\hbar}{m}P_{\parallel}k_z & -\mu_B\cos^2\theta^+(H_x+iH_y) & \left.\begin{array}{c} -\frac{E_G}{2} + \frac{\hbar^2}{2m}(K_x^2+K_y^2+K_z^2) \\ -\mu_B H_z(\cos^2\theta^+-\sin^2\theta^+) \end{array}\right)
\end{array} ,$$

$$(\text{VII.3})$$

where $\vec{k}=\frac{1}{\hbar}(\vec{p}+e\vec{A}/c)$, $\vec{p}=-i\hbar\vec{\nabla}$, $\vec{A}=\frac{1}{2}(\vec{H}\times\vec{r})$, $\mu_B=\frac{e\hbar}{2mc}$, and m is the free electron mass. The zero of energy is taken at the center of the energy gap $E_G=E(L_6^-)-E(L_6^+)$, which is positive at the PbTe side of the crossover. The transverse and longitudinal momentum matrix elements $P_\perp$ and $P_\parallel$, respectively are

$$P_\perp = -\frac{i}{\sqrt{2}}\sin\theta^-\cos\theta^+ < X|\vec{p}|R > = -\frac{i}{\sqrt{2}}\sin\theta^-\cos\theta^+ < Y|\vec{p}|R > ,$$

$$P_\parallel = -i\cos\theta^-\cos\theta^+ < Z|\vec{p}|R > . \qquad (\text{VII.4})$$

When H=0 in eq.(VII.3), we can obtain the dispersion relation describing the conduction and valence bands, by making the secular equation

$$\det|\hat{H}_{\text{eff}} - E\hat{I}|=0 , \qquad (\text{VII.5})$$

where $\hat{I}$ is the 4×4 unit matrix. When H=0, $\vec{k}=-i\hbar\vec{\nabla}$, and the dispersion relation is given by

$$\left\{\frac{E_G}{2} + \frac{\hbar^2}{2m}(k_x^2+k_y^2+k_z^2) - E\right\}\left\{-\frac{E_G}{2} + \frac{\hbar^2}{2m}(k_x^2+k_y^2+k_z^2) - E\right\}$$

$$= \left(\frac{\hbar}{m}\right)^2\left\{P_\perp^2(k_x^2+k_y^2) + P_\parallel^2 k_z^2\right\} . \qquad (\text{VII.6})$$

Thus the energy of the conduction and valence bands are

$$E^\pm = \frac{\hbar^2}{2m}(k_x^2+k_y^2+k_z^2) \pm \frac{1}{2}\sqrt{E_G^2 + \frac{4\hbar^2}{m}\left[P_\perp^2(k_x^2+k_y^2) + P_\parallel^2 k_z^2\right]} , \qquad (\text{VII.7})$$

where ± signs refer to the energy of $E(L_6^-)$ and $E(L_6^+)$, respectively. If there are four ellipsoids as in the present case, the carrier concentration is

$$n = \frac{4}{3\pi^2}(k_t^2 k_1) , \qquad (\text{VII.8,a})$$

where

$$k_t^2 = \frac{2m}{\hbar^2}\left\{(E+P_\perp^2/m) - \sqrt{(E+P_\perp^2/m)^2 - (E^2-E_G^2/4)}\right\} , \qquad (\text{VII.8,b})$$

and

$$k_l^2 = \frac{2m}{\hbar^2}\left\{(E+P_{\parallel}^2/m) - \sqrt{(E+P_{\parallel}^2/m)^2 - (E^2-E_G^2/4)}\right\} \quad . \qquad (\text{ VII.8,c })$$

The subscripts t and l represent the transverse and longitudinal component with respect to the major axis of the ellipsoid, and $k_l=k_z$, $k_t=k_x=k_y$.

The anisotropy of the Fermi surface, K, at the Fermi level, which is equal to the mass anisotropy in the parabolic band, is defined as

$$K|_{k=k_F} = k_l^2/k_t^2|_{k=k_F} \quad , \qquad (\text{ VII.9,a })$$

which is given by the equation

$$K = \frac{(mE+P_{\parallel}^2) - \sqrt{(mE+P_{\parallel}^2)^2 + m^2(E_G^2/4-E^2)}}{(mE+P_{\perp}^2) - \sqrt{(mE+P_{\perp}^2)^2 + m^2(E_G^2/4-E^2)}} \quad . \qquad (\text{ VII.9,b })$$

The cyclotron effective mass at the Fermi level is given by the following equations,

$$m_t^* = \frac{\hbar^2}{2\pi}\frac{\partial A_t}{\partial E} = \frac{1}{2}\,\frac{2E - \frac{\hbar^2}{m^2}\frac{A_t}{\pi}}{\frac{P_{\perp}^2}{m^2} + \frac{E}{m} - \frac{\hbar^2}{2m^2}\frac{A_t}{\pi}} \quad , \qquad (\text{ VII.10,a })$$

and

$$m_l^* = \frac{\hbar^2}{2\pi}\frac{\partial A_l}{\partial E} = \frac{1}{2}\,\frac{2E - \frac{\hbar^2}{m^2}\frac{A_l}{\pi}}{\frac{P_{\parallel}^2}{m^2} + \frac{E}{m} - \frac{\hbar^2}{2m^2}\frac{A_l}{\pi}} \quad , \qquad (\text{ VII.10,b })$$

where $A_t=\pi k_t^2$, $A_l=\pi k_l^2$.

The mass anisotropy at the Fermi level K' which is defined as $K' = m_l^*/m_t^*|_{E=E_F}$ is

$$K' = \frac{(\ 2E - \hbar^2 k_l^2/m^2\ )\ (\ P_{\parallel}^2/m + E - \hbar^2 k_l^2/2m\ )}{(\ 2E - \hbar^2 k_t^2/m^2\ )\ (\ P_{\perp}^2/m + E - \hbar^2 k_t^2/2m\ )} \quad . \qquad (\text{ VII.11,a })$$

At the band edge ($E_F=0$), the above relation becomes

$$K'_{edge} = \frac{E + P_{\perp}^2/m}{E + P_{\parallel}^2/m} \quad , \qquad (\text{ VII.11,b })$$

which is equal to the anisotropy of the Fermi surface at the band edge. However at finite Fermi level, K' is slightly smaller than K.

From eq.(VII.8,a),

$$k_t^2 = \frac{n^{2/3}}{(4/3\pi^2)^{2/3}K^{1/3}} \quad . \qquad (\text{VII.12})$$

Letting $k_y=k_z=0$, the energy of the conduction band becomes,

$$E^C = k_x^2 + \frac{1}{2}\sqrt{E_G^2 + 16P_\perp^2 k_x^2} \quad . \qquad (\text{VII.13})$$

Above equation is written in the atomic units (au.). The atomic units are employed instead of the CGS units through out the followings. If otherwise, the units are noted. The cyclotron effective mass at the Fermi level is,

$$M_t^- = \frac{m_t^*}{m} = (E - 2k_x^2)/(2P_\perp^2 + E + k_x^2) \quad . \qquad (\text{VII.10,c})$$

With eqs.(VII.10,c) and (VII.13), we have for small $\vec{k}$

$$(M_t)^{-1} = 1 + 4P_\perp^2(E_G^2 + 16P_\perp^2 k_x^2)^{-1/2} \quad . \qquad (\text{VII.14})$$

Using eq.(VII.12), we have

$$\left(\frac{M_t^-}{1-M_t^-}\right)^2 = \frac{E_G}{16P_\perp^4} + \frac{n^{2/3}}{P_\perp^2(4/3\pi^2)^{2/3}K^{1/3}} \quad . \qquad (\text{VII.15})$$

Another definition of the effective mass $m^{-1} = \frac{1}{k}\frac{\partial E}{\partial k}$ also gives the same result.

If we plot the experimentally obtained $[M_t/(1-M_t)]^2$ against $\frac{n^{2/3}}{(4/3\pi^2)^{2/3}K^{1/3}}$, the eq.(VII.15) represents a straight line whose slope and the vertical intersection give the transverse momentum matrix element $P_\perp$ and the energy gap E_G, respectively. This relation for n-type PbTe is given in Fig.28. As the results of the analysis, we have the E_G=183 meV and $4P_\perp^2$=0.58 (au.) for PbTe. Using the transverse momentum matrix element $P_\perp$ determined for PbTe, we may obtain the energy gap for the alloy system, assuming that the transverse momentum matrix element $P_\perp$

varies linearly with the alloy composition, scince $P_\perp$ is proportional to $\sin\theta^-\cos\theta^+$. We assume that $4P_\perp^2=0.58(1 + 0.211x)^2$ (au.) using a result of pseudo-potential calculation by Bernick and Kleinman.79) They reported that $\sin\theta^- = -0.493$ and $\cos\theta^+=0.978$ for PbTe, and $\sin\theta^- = -0.695$ and $\cos\theta^+=0.987$ for SnTe. The energy gaps, thus obtained for the alloy system, are given in Fig.29 as a function of alloy composition. Using the result of Bernick and Kleinman, we can also assume that $4P_\parallel^2=4P_\parallel^2{}_{[\mathrm{PbTe}]}(1 - 0.142x)^2$, scince $P_\parallel$ is proportional to $\cos\theta^-\cos\theta^+$ Then we can determine the best fit value with the experimentally obtained anisotropy K's and the [100] effective masses. The best fit value of the longitudinal momentum matrix element is $4P_\parallel^2=0.046(1- 0.142x)^2$ (au.).

Though the six-band model is better approximation, too many parameters make the physical meanings and the behavior of the band edge structure obscure. To determine many parameters for PbTe is a meaningful work, however to calculate the band structure of alloys using the fixed parameters at PbTe is far from a meaningful approximation for the alloy system, because they do vary across the alloy composition. Thus we have considered composition dependence of the parameters in the two-band model.

Figs.30-32 show the values of K and the effective mass as a function of the alloy composition together with their band edge values.

When $\vec{H}=0$, eq.(VII.3) becomes complicated and cannot be solved easily. However, when $\vec{H}$ // [111] and $k_z=0$, eq.(VII.3) can be decoupled into two 2×2 matrix. In this case, the eigen value of the Hamiltonian (VII.3) can be obtained analytically by solving 2×2 resultant equations.

Thus the energy of the conduction band is given by the following equation

$$E^C_{N,\sigma}= \hbar\tilde{\omega}_c(N+\frac{1}{2}) + \mu_B(\cos^2\theta^- -\sin^2\theta^- -\cos^2\theta^+ +\sin^2\theta^+)sH_z$$
$$+\sqrt{[\frac{E_G}{2} + \mu_B(\cos^2\theta^- -\sin^2\theta^- +\cos^2\theta^+ -\sin^2\theta^+)sH_z]^2+\left(\frac{\hbar}{m}\right)^2 P_\perp^2\frac{2m\tilde{\omega}_c}{\hbar}[(N+\frac{1}{2})+s]} \quad , \qquad (\text{VII.16})$$

where $s=\frac{1}{2}$ for $\sigma=\uparrow$, $s=-\frac{1}{2}$ for $\sigma=\downarrow$, N is the Landau quantum number, and $\tilde{\omega}_c=eH_z/mc$. When H_z is very small, the conduction band edge g-factor for H // [111] can be calculated, in CGS units,

$$g_1^c = 2[(\cos^2\theta^- - \sin^2\theta^-) + \frac{2P_\perp^2}{mE_G}] . \qquad (\text{VII.17})$$

The detailed procedure is given in Appendix B.

B. Six Band Model

In the two band approximation described above, which is closely similar to the case of Bi,[100] the spin splitting of the Landau level $g\mu_B H$ is equal to the Landau level separation $\hbar\omega_c$ when the free electron contribution is neglected. However, if there are interactions with the remote bands, the size of the spin splitting changes from the Landau level separation. The size of the effective g-value at the Fermi level is mainly determined by the size of the effective mass at the Fermi level. Thus, the ratio of the spin splitting to the Landau level separation $\nu=m_c^*g/2m$ is a more sensitive parameter than the effective g value itself to see the effect of the remote bands. The spin splittings in such materials as PbTe, $Pb_{1-x}Sn_xTe$, and Bi arise from the difference between the cyclotron effective mass m_c^* which determines the Landau level separation and the effective spin mass m_s^* which determines the spin splitting.

Because the spin splittings in these materials are the second order effect, we have to take the interactions with the remote bands into account, when the spin splitting is concerned.

Adler et al.[85] calculated the Fermi surface, the Landau levels, and the effective g-value for $Pb_{1-x}Sn_xTe$ based on the band scheme shown in Fig.33, treating the $\vec{k}\cdot\vec{p}$ couplings with the remote bands to the second order perturbation theory according to the method of Luttinger and Kohn.[101]

According to Senturia et al., the longitudinal effective g-value ($\vec{H}$ parallel to the longitudinal axis of the ellipsoid) at the band edge is given by the equation (in au.),

$$g^{\pm} = \frac{\mp 8|P_{\perp}|^{2}}{E_{G}} \mp g_{1}^{\pm} , \qquad \text{(VII.18,a)}$$

where

$$g_{1}^{\pm} = 2[(\cos^{2}\theta^{\pm} - \sin^{2}\theta^{\pm}) \mp \frac{4|P_{t,\pm1}|}{E_{\pm1}} \pm \frac{4|P_{t,\pm2}|^{2}}{E_{\pm2}}] . \qquad \text{(VII.18,b)}$$

In the above equation, ± signs refer to the $L_{6}^{\pm}$ bands, $g_{1}^{\pm}$ is the free electron and the remote band contributions to the g-value, $E_{\pm1}$, $E_{\pm2}$ is the energy of the remote bands measured from the center of the energy gap, and $P_{t,\pm1}$, $P_{t,\pm2}$ are the transverse components of the momentum matrix elements between the conduction (or the valence) band and the remote bands. These quantities are also given in Fig.33.

They also calculated the transverse effective mass ratio at the band edge:

$$\left(\frac{m_{c}^{\pm}}{m}\right)^{-1} = \frac{4P_{\perp}^{2}}{E_{G}} + \frac{1}{m_{t}^{\pm}} , \qquad \text{(VII.19,a)}$$

where

$$(m_{t}^{\pm})^{-1} = \mp 1 + \frac{4|P_{t,\pm1}|^{2}}{E_{\pm1}} + \frac{8|P_{t,\pm2}|^{2}}{E_{\pm2}} . \qquad \text{(VII.19,b)}$$

The effective spin mass m_{s}^{*} is defined as

$$(m_{s}^{*\pm})^{-1} = | g^{\pm} |/2m_{(CGS)} = | g^{\pm} | . \qquad \text{(VII.20)}$$

When $(m_{c}^{\pm})^{-1} > (m_{s}^{\pm})^{-1}$, the Landau level separation is larger than spin splitting, where $m_{c}^{\pm}$ is the transverse cyclotron mass, and when $(m_{c}^{\pm})^{-1} < (m_{s}^{\pm})^{-1}$, vice versa.

Substituting eq.(VII.20) in eq.(VII.19,a) and (VII.19,b), $(m_{s}^{\pm})^{-1}$ becomes

$$(m_s^{\pm})^{-1} = | g^{\pm} | . \qquad \text{(VII.21)}$$

If we compare eq.(VII.21) with eqs.(VII.19,a) and (VII.19,b), we have

$$(m_c^{\pm})^{-1} > (m_s^{\pm})^{-1},$$

for the band scheme given in Fig.33. However, if the band ordering is different, ie. the parity of the upper two and lower two bands are interchanged, then

$$(m_c^{\pm})^{-1} < (m_s^{\pm})^{-1}.$$

This means that the spin splitting is larger than the Landau level separation.

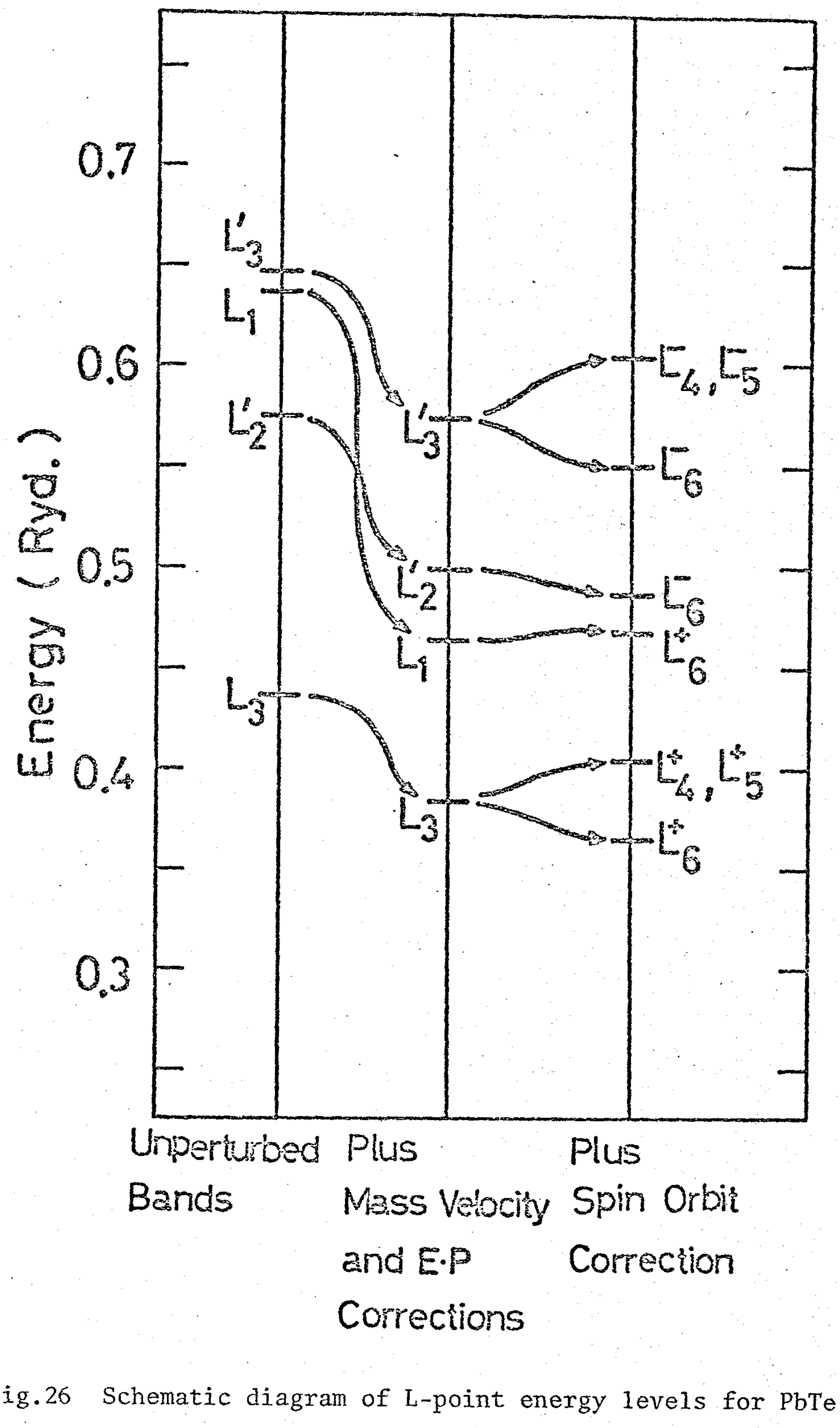

Fig.26 Schematic diagram of L-point energy levels for PbTe near the energy gap. Energy shifts due to the relativistic corrections and the spin-orbit correction are illustrated. After Pratt and Ferreira.[102)]

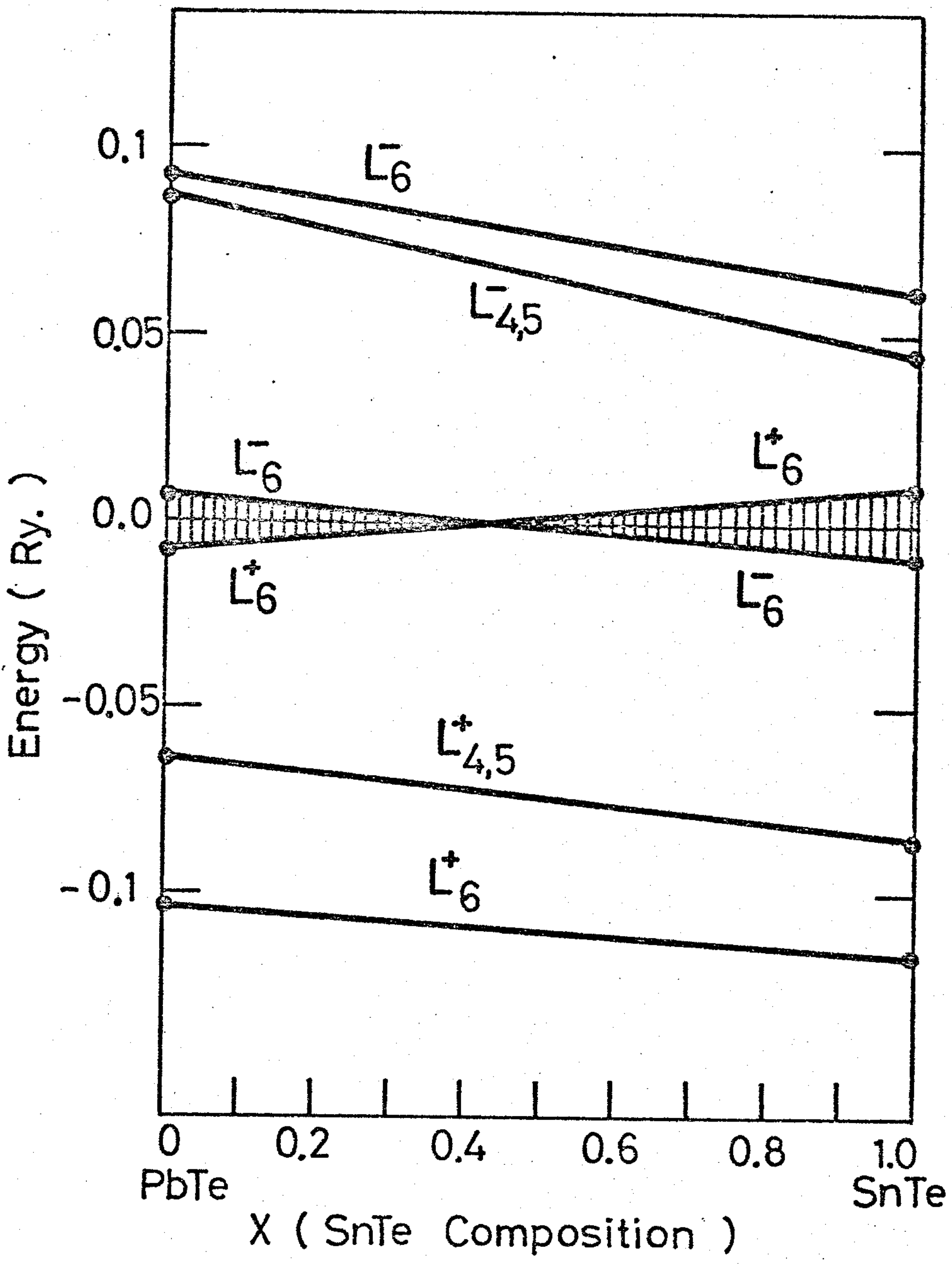

Fig.27 Approximate variation of six energy levels around the energy gap at the L-point as a function of alloy composition. End points are taken from the result of Bernick and Kleinman.[79)]

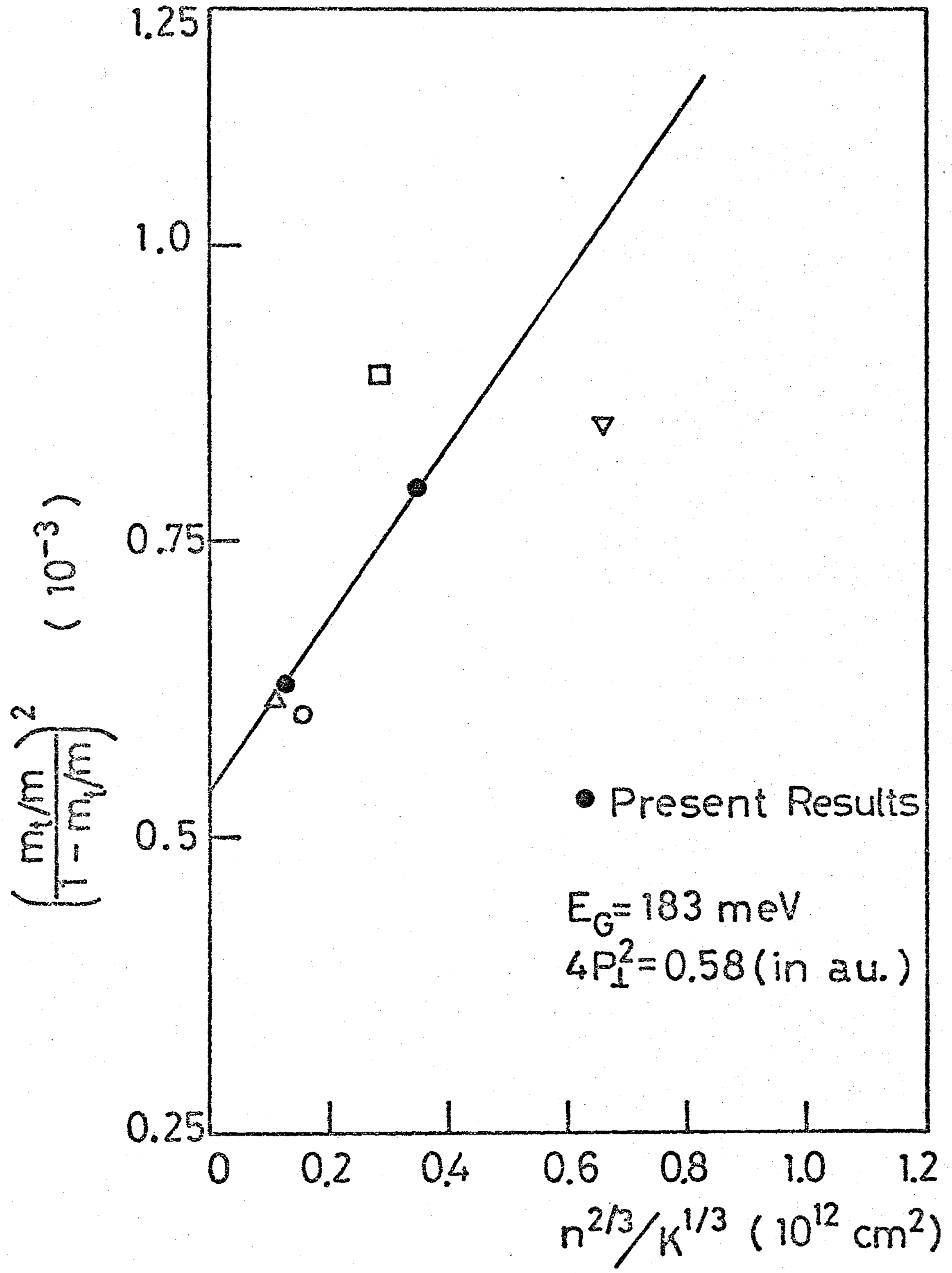

Fig.28 Plots of $\left(\frac{m_t^*/m}{1-m_t^*/m}\right)^2$ as a function of $n^{2/3}/K^{1/3}$ for n-type PbTe with various carrier concentrations: Figure references: ☐ -Cuff et al.[55)]; △ - Saleh and Fan[103)]; ▽ - Nishikawa et al.[104)]; ○ - Nii.[57)]

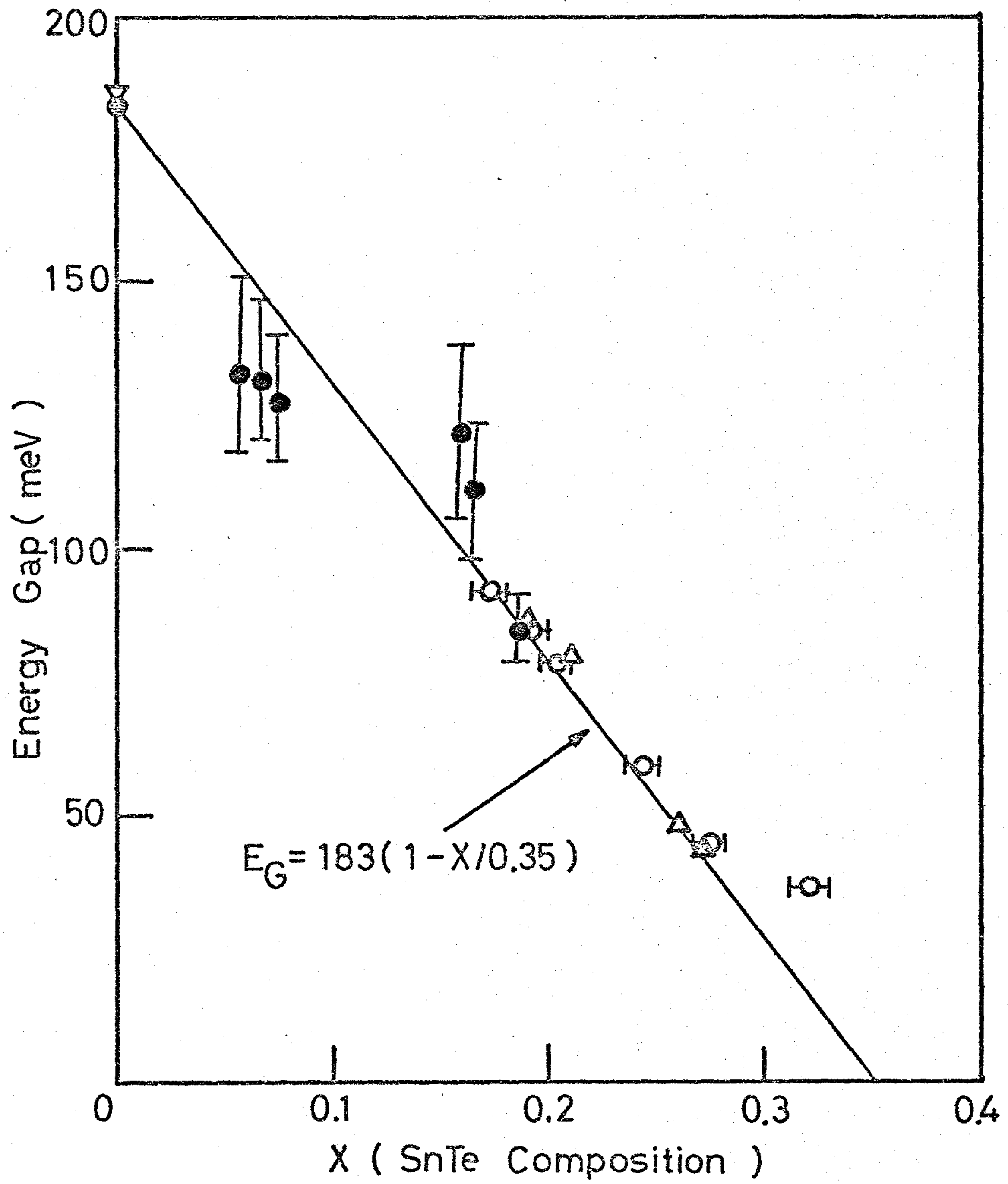

Fig.29 Energy gap variation with alloy composition. The plots in the figure represent: ● - present results; ○ - Harman[47)]; ▽ - Butler and Calawa[61)]; △ - Butler.[45)]

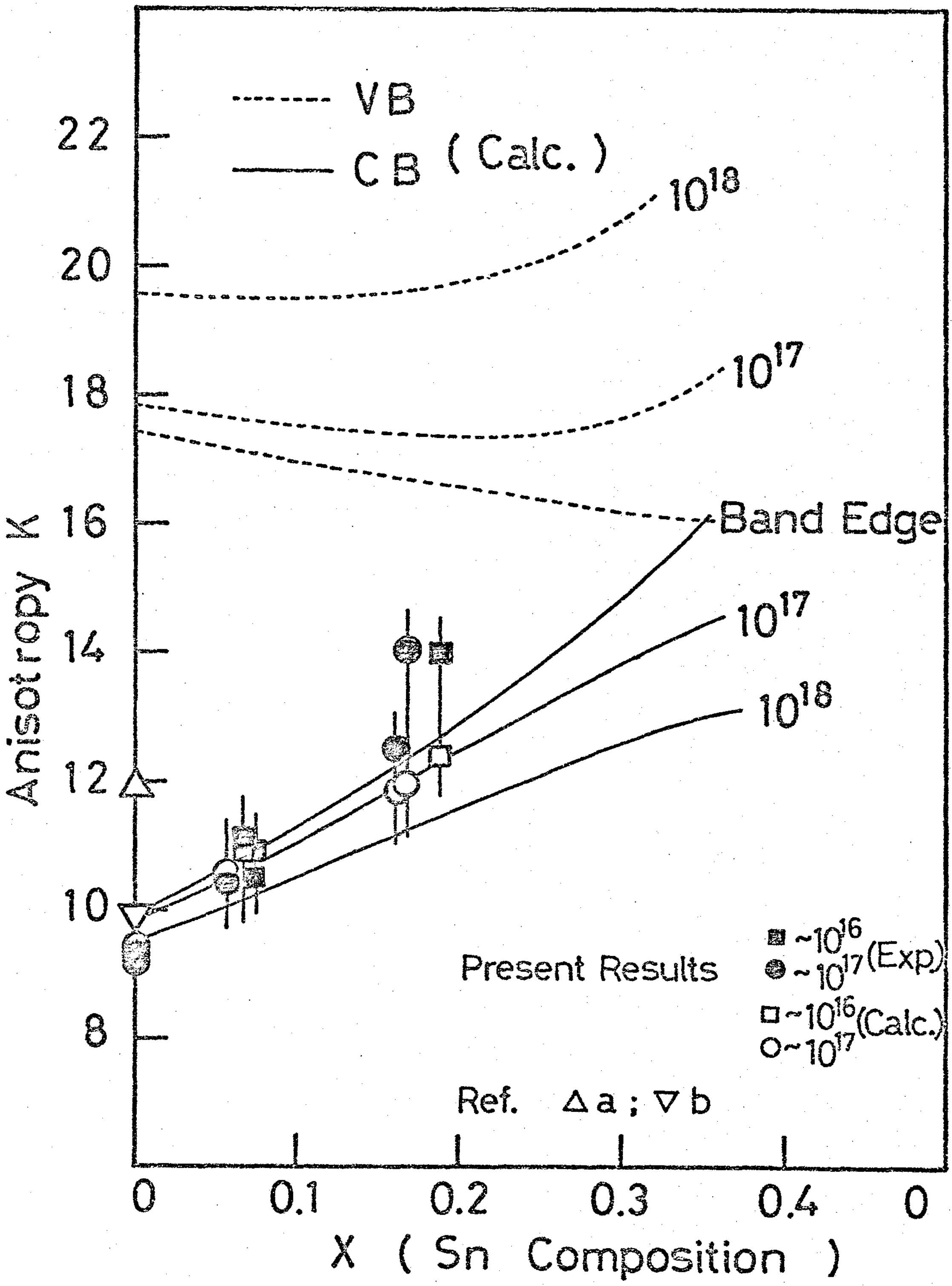

Fig.30 Variation of anisotropy K as a function of alloy composition. Calculated curves and the points (open symbols) by the two-band model with the best fit parameters are given. Figure references: a) Nii[57), b) Schilz.[58)

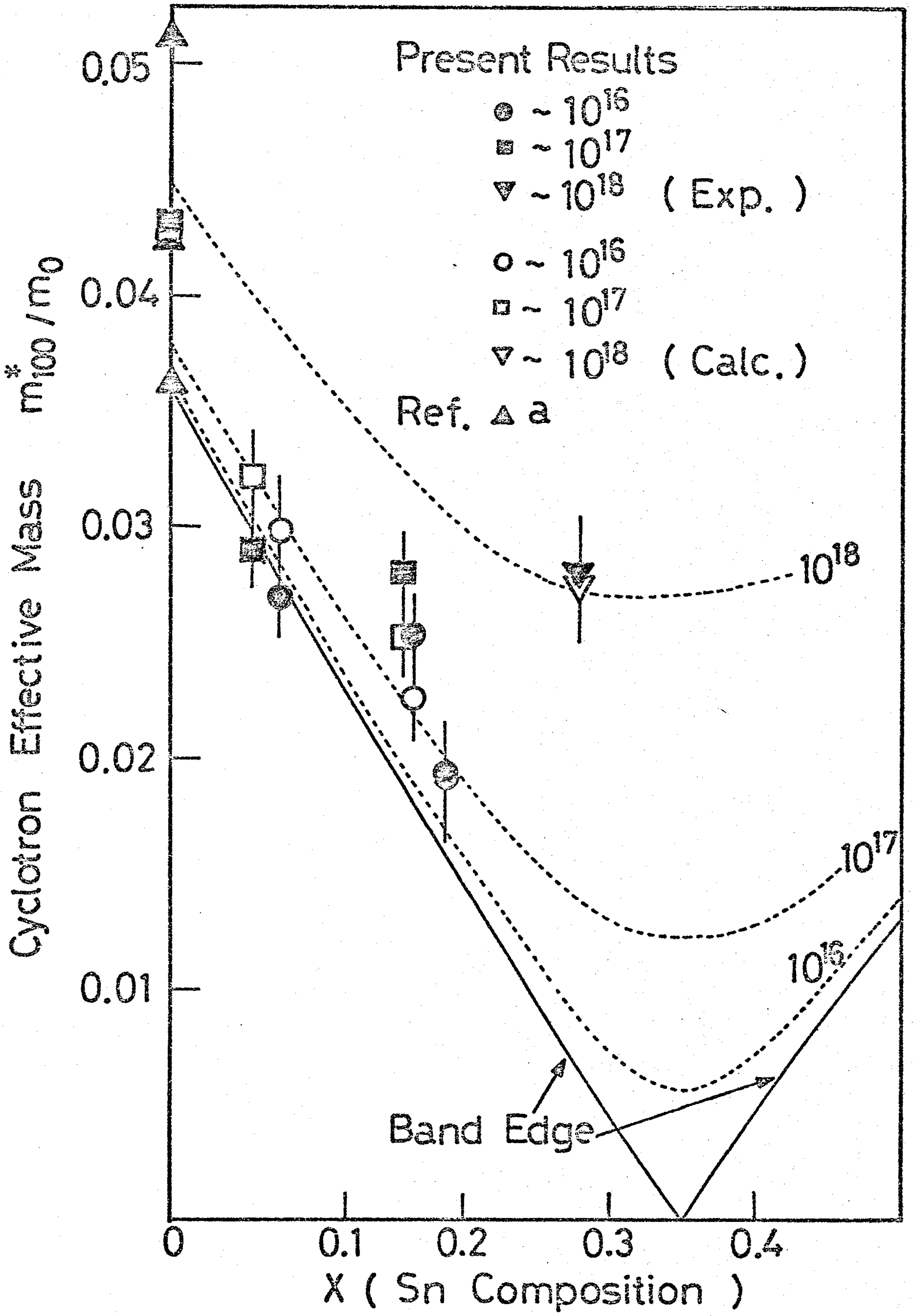

Fig.31 Variation of [100] cyclotron effective mass as a function of alloy composition. Calculated curves and the points(open symbols) by the two-band model with the best fit parameters are given. Figure reference: a) Cuff et al.[55)]

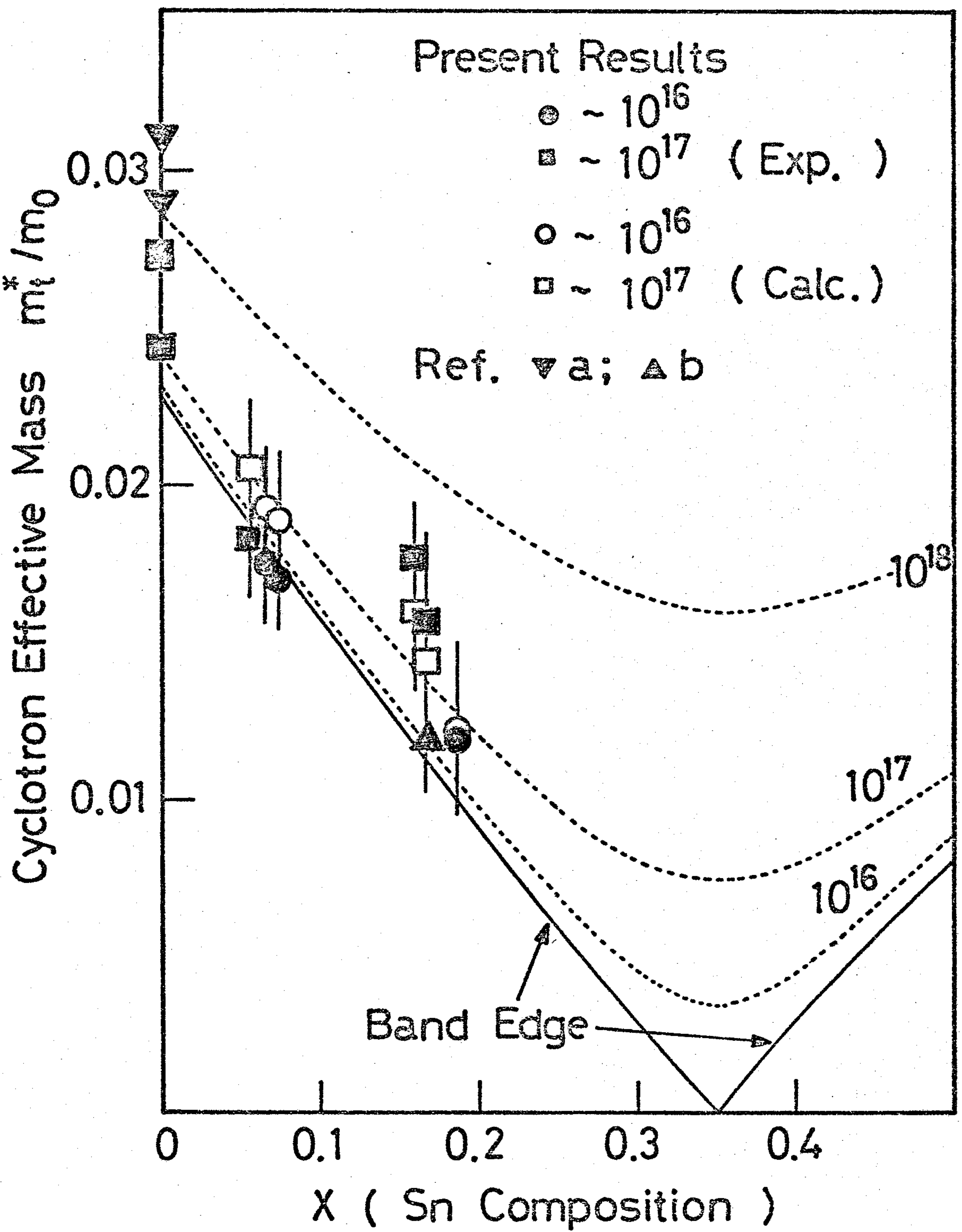

Fig.32 Variation of [111] cyclotron effective mass as a function of alloy composition. Calculated curves and points (open symbols) by the two-band model with the best fit parameter are given. Figure references: a) Cuff et al.[55)], b) Melngailis et al.[39)].

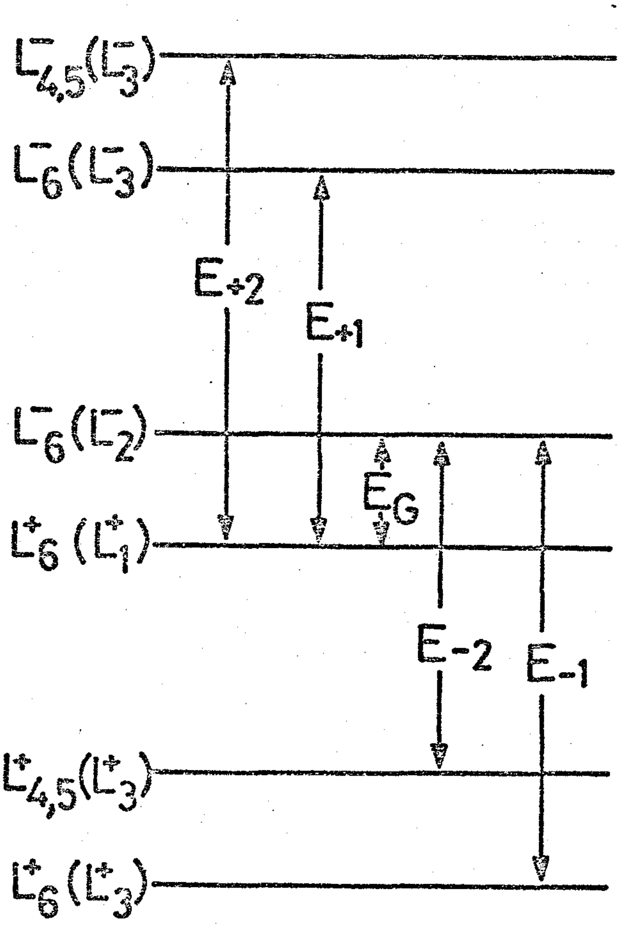

Momentum Matrix Elements

Energy Gap	Longitudinal	Transverse
E_G	$P_{\parallel}$	$P_{\perp}$
$E_{\pm 1}$	$P_{1,\pm 1}$	$P_{t,\pm 1}$
$E_{\pm 2}$	$P_{1,\pm 2}$	$P_{t,\pm 2}$

So far accepted band ordering

Fig.33 Schematic diagram for the six L-point energy levels and the impotant momentum matrix elements which couple them. The band ordering is so far accepted one which is appropriate to the PbTe-side of the crossover.

VII.2. Spin Effect

As one of our primary interests is the spin effect in the oscillatory magnetoresistance of $Pb_{1-x}Sn_xTe$ alloys, we have to concern the theoretical treatment in which the spin effects upon the transport properties are correctly taken into account. In chapter V, we have mentioned that the TMR differs remarkably from the LMR, and that this, we considered, is originated in the spin effect. If we refer to the previous experimental results on other materials which accurately exhibit the spin effect, the materials seem to be divided into the following categories according to the difference of the spin effect between the TMR and the LMR.

(i) Both H_N^+ and H_N^- peaks including the H_0^+ peak appear in the TMR, and H_N^- peaks and also the H_0^+ peak are missing or very small in the LMR. (InSb,36) HgTe,98) $Hg_{1-x}Cd_xTe$37,95))

(ii) H_0^+ spin splitting peak appears both in the TMR and the LMR. (GaAs19))

(iii) Both H_N^+ and H_N^- peaks appear in the TMR, and H_N^+ peaks are missing but H_N^- peak appears in the LMR. (n-type PbTe,40) $Pb_{1-x}Sn_xTe$40); PbTe side)

The theory have to bear the test whether discrepancy to the facts listed above arises or not. However, we have few articles in which the theory of the quantum oscillation in resistivity is treated with the spin effects taken into account, as we have mentioned in chapter I.

As far as we know, these are the articles by Gurevich and Éfros,41) Roth and Argyres,88) Éfros,42) and Suizu and Narita.43,37)

The first two articles treated the spin splittings in the quantum oscillations of the TMR in which the theory of Argyres,9) Adams and Holstein,12) etc. are modified. In their treatment, they considered, if the quantum oscillations arise from the impurity or acoustic phonon scattering, spin reversal scattering is negligible. That is, they only replaced the Landau level energy $(N + \frac{1}{2})\hbar\omega_c$ by $(N + \frac{1}{2} \pm \frac{\nu}{2})\hbar\omega_c$. However, though these theory could explain the positions of the spin splitting peaks, H_0^+ peak can not appear in the TMR, if the spin-flip scattering does not occur. So the case (i) given above can not be explained by their theory. On the other hand, the theory of Efros gave the explanation of the missing of H_0^+ peak in the LMR obseved in InSb,36) assuming that the probability of the spin reversal transition is very small. Though his assumption could well explain the missing of H_0^+ peak, the missing of H_N^- peaks in InSb,36) $Hg_{1-x}Cd_xTe$,37,43,95) $Pb_{1-x}Sn_xTe$,40) and so on in the LMR could not be explained. In addition, the appearance of the H_0^+ peak in the LMR of GaAs19) can not be explained. Thus the theory of Efros contradicts to the case (i), (ii), and (iii). However, for the case (ii), there exists possibility that the TMR component is mixed into the LMR, because of the eddy current due to the pulse magnet, of the inhomogeneity of the sample, and of the contact effect.

Recently, Suizu and Narita considered that the spin flip scattering plays a significant role in the quantum oscillations in the magnetoresistance of $Hg_{1-x}Cd_xTe$, in their theoretical treatment.37,43)

A. Spin-Flip Scattering

Because their experimental results upon $Hg_{1-x}Cd_xTe$ alloys show that the spin splitting oscillations of the TMR vividly differ from the LMR, the spin is considered to play a significant role in the scattering transitions. Thus considering that the strong spin-orbit interaction in such materials give rise to the spin flip scattering, because the large electronic g-values in these materials come from the strong spin-orbit interaction, they obtained the selection rules for the TMR and LMR. These selection rules can well explain the behavior of the spin effects in $Hg_{1-x}Cd_xTe$. Thus we consider their selection rules.

In $Pb_{1-x}Sn_xTe$ alloys, the constituent atoms, Pb, Sn, and Te have large atomic numbers. Especially, Pb has the largest atomic number of all, therefore the strong spin-orbit interaction in these alloys, particulary in alloys with large PbTe composition, the spin-orbit interaction may significantly affect the electronic properties of the crystal. Though we cannot discuss the spin-orbit energy in the alloy crystals directly from the atomic one, such a large valence spin-orbit splitting of the 6p-electron in Pb atom known as 0.0936 Ry.77) which is greater in magnitude about an order than the energy gap of about 0.013 Ry. of PbTe, suggests the existance of strong spin-orbit interactions in $Pb_{1-x}Sn_xTe$ alloys.

In addition, screening by the electron gas as well as the strong screening effect due to the anomalously large dielectric constant inherent in the small gap semiconductors largely reduce the Rutherford scattering in $Pb_{1-x}Sn_xTe$. When coulomb potential of an impurity atom is strongly screened, scattering due to the spin-orbit interaction will become dominant, because electrons can approach close to the impurity atom where the gradient $\partial U/\partial r$ is large without feeling the long range coulomb force. Thus the scatterin transition due to the spin-orbit interaction must be important process for the transport phenomena in the small gap semiconductors.

Therefore we consider the spin flip scattering due to the spin-orbit interaction, according to the treatment by Suizu and Narita.37) The derivation of the expression for the TMR and LMR given by Suizu and Narita is briefly given in Appendix C.

B. Selection Rules

The matrix elements of $\dot{z}$ and $\dot{X}$ appear in the expressions of $\sigma_\perp$ and $\sigma_\parallel$ given in Appendix C determine the possible interlevel transitions. Thus the matrix elements of $\dot{z}$ and $\dot{X}$ will lead to the selection rules for the scattering transitions of the TMR and LMR. If we assume that the transition with $\Delta N=1$, $\Delta s=0$ is the most probable, in other words, the other transitions are treated as the correction terms, the selection rules for the TMR and LMR can be obtained. These are

$$N\!\downarrow \; \rightleftarrows \; (N-1)\!\uparrow \;, \qquad \text{for the LMR}$$

and

$$N\!\uparrow \; \rightleftarrows \; (N-1)\!\uparrow \;,$$

$$N\!\downarrow \; \rightleftarrows \; (N-1)\!\downarrow \;,$$

$$N\!\uparrow \; \rightleftarrows \; N\!\downarrow \;, \qquad \text{for the TMR.}$$

These relations represent the spin flip scatterings due to the spin-orbit interaction. In addition, there exists the transition of $\Delta N=1$, $\Delta s=0$ which has already been considered by Argyres,9) Efros,42) and some other physicists.

However, in the narrow gap semiconductors such as $Pb_{1-x}Sn_xTe$, InSb, $Hg_{1-x}Cd_xTe$, and so on, the Bloch amplitudes are not pure spin functions. The eigenfunctions of the effective hamiltonian for $Pb_{1-x}Sn_xTe$ must be expressed as a linear combinations of the Landau levels with different quantum number N, and of the mixed conduction and valence states with the mixed spin states. These properties of the band wave functions will introduce new features into the scattering process, which will give different transport properties from the free electron case.

The wave functions for the Landau levels of the conduction and the valence bands of $Pb_{1-x}Sn_xTe$ are given by Adler et al.85) They are given in Appendix D. According to Roth and Argyres,[88)] the longitudinal magnetoconductivity is

$$\sigma_{zz} = \rho^{-1} = -\frac{e^2}{\Omega}\sum_{Nk\sigma} \frac{\partial f}{\partial E_{Nk\sigma}} \sum_{N'k'\sigma'} [\, W_{Nk\sigma,N'k'\sigma'}(\, 1-k_z'/k_z)\,]^{-1}, \qquad (\text{ VII.22 })$$

where

$$W_{Nk\sigma,N'k'\sigma'} = \frac{2\pi}{\hbar} < |<Nk\sigma|U|N'k'\sigma'>|^2 >_s \delta(\, E_{Nk\sigma} - E_{N'k'\sigma'}\,)$$

is the transition probability in the Born approximation. As we can see from eq.(VII.22), the scattering which gives rise to the oscillatory LMR is one which changes k_z. As we can see from Fig.36,a, for elastic scattering, such a scattering must change N or σ, and the scattering which does not change k_z connot contribute σ_{zz}, since $(\, 1-k_z'/k_z\,) = 0$ for $k_z = k_z'$. Then we will consider the scattering which changes k_z, N, or σ.in the band electron picture. Moreover the transitions which contribute the oscillatory phenomena through the singularity of the density of states at the bottom of the Landau level are such that $(\, k_z=0,N,\sigma\,)$ $\rightleftarrows (\, k_z \neq 0,N',\sigma'\,)$. As given in Appendix E, non-zero matrix elements of the scattering potential $U(\vec{r})$ can be known from the orthogonality of cell periodic functions $\psi^T_{\mu\sigma}$ and their coefficients $A^N_{\mu\sigma,\mu'\sigma'}$ which determine the size of matrix elements. Non-zero matrix elements are given in Table II. From the Table II, we can see that the probabilities of the transitions which changes k_z are,

$0\downarrow \rightleftarrows 0\uparrow$ --- Negligibly small

$0\downarrow \rightleftarrows 1\downarrow$, $0\uparrow \rightleftarrows 1\uparrow$ --- Large

$N\downarrow \rightleftarrows N'\downarrow$, $N\uparrow \rightleftarrows N'\uparrow$ --- Large

$N\downarrow \rightleftarrows N'\uparrow$, $N\uparrow \rightleftarrows N'\downarrow$ --- Small but increases with increasing k_z.

Thus, the probability of the spin-flip scattering is negligibly small for $N=N'=0$, and small but increases with increasing k_z for $N \neq 0$. The selection rules for the scattering transitions are given in Fig.37.

On the other hand, the transverse magnetoconductivity σ_{xx}, is given by the equation,[88)]

$$\sigma_{xx} = - \frac{e^2}{2\Omega} \sum_{\substack{Nk\sigma \\ N'k'\sigma'}} \frac{\partial f}{\partial E_{Nk\sigma}} W_{Nk\sigma,N'k'\sigma'} (X_k - X_{k'})^2, \qquad (\text{VII.23})$$

where X_k and $X_{k'}$ are the centers of the cyclotron motion. The TMR is expressed in terms of σ_{xx} as

$$\rho_{\perp} = \sigma_{xx} / (\sigma_{xx}^2 + \sigma_{yx}^2) ,$$

and for large Hall angle, ie., when $\sigma_{yx} \gg \sigma_{xx}$, this becomes

$$\rho_{\perp} \approx (H/nec)^2 \sigma_{xx}.$$

Thus, from eq.(VII.23), the scattering which contributes the oscillatory TMR is one which changes X_k, hence which changes k_x and k_y, since $(X_k - X_{k'})$ vanishes, if $X_k = X_{k'}$. For elastic scattering, the transitions $(k_x,k_y,k_z=0,N\sigma) \rightleftarrows (k'_x,k'_y,k_z=0,N\sigma)$, and $(k_x,k_y,k_z,N\sigma) \not\rightleftarrows (k'_x,k'_y,k'_z,N'\sigma')$, where $k_z \neq k'_z$ and $N\sigma \neq N'\sigma'$ will contribute the oscillatory magnetoresistance. Such transitions are illustrated in Fig.36,b. According to Adams and Holstein,[12)] for the TMR, when broadening is strong (ie. Γ/ζ is large, where $\Gamma = (\omega_c \tau)^{-1}$), the contribution of the intralevel transition to the oscillatory component (the term represented by R in eq.(II.9,a)) is negligible, however for the high field oscillation (ie. Γ/ζ is small) where only few oscillator states are occupied, the contribution of the intralevel transition becomes significant, and hence all the peaks may be observed whenever the Fermi level crosses the corresponding Landau levels for low quantum number in the TMR.

C. Discussion

In order to compare the present experimental results with the other results, we refered the previous works upon $Hg_{1-x}Cd_xTe$,$^{37)}$ InSb,$^{36)}$ and GaSb,$^{105)}$ which accurately exhibit the difference between the TMR and LMR, and are given in Figs.34 (a), (b), and (c). Fig.35 represents the diagrams for the selection rules given by Suizu and Narita.$^{36,43)}$ In the figure,34 (a) and (b) represent the diagrams for n-type $Pb_{1-x}Sn_xTe$ ($g>0$), (a) being the case $m_c^*|g|/2m > 1$, (b) being the case $m_c^*|g|/2m < 1$, and (c) represents the diagram for $Hg_{1-x}Cd_xTe$ ($g<0$, $m_c^*|g|/2m < 1$). We can easily understand from the diagrams that, if there exists upward arrow to a certain energy level, an oscillatory peak corresponding to this energy level may appear, and if not, peak cannot appear.

In the case of $Hg_{1-x}Cd_xTe$, it can be understood from Fig.35(c) that the H_0^+ oscillatory peak and the series of H_N^- peaks cannot appear in the LMR, however H_0^+ and the series of H_N^+ and H_N^- peaks can appear in the TMR. Moreover, from the number of upward arrows, we can discuss qualitatively the strength of the oscillatory peaks, if the transition probabilities of $N\uparrow \rightleftarrows (N-1)\uparrow$ and $N\downarrow \rightleftarrows (N-1)\downarrow$ are equal. From the above discussion, we can say qualitatively that the series of H_N^+ is stronger than H_N^- series in the TMR of $Hg_{1-x}Cd_xTe$, which is in satisfactory agreement with the previous experimental results upon $Hg_{1-x}Cd_xTe$.$^{35)}$

In the case of InSb and GaSb where $g<0$, the diagram in Fig.35 (c) is also applicable, and the previous experimental results, given in Fig.34 (b) and (c), are also consistent with the diagram.

On the other hand, for n-type $Pb_{1-x}Sn_xTe$ ($g>0$), similar diagrams are given for both the assumed cases, $\hbar\omega_c < g\mu_BH$ (Fig.35 (a)) and $\hbar\omega_c > g\mu_BH$ (Fig.35 (b)).

At first we consider the case $\hbar\omega_c > g\mu_BH$, that is, the Landau level separation is greater than the spin-Zeeman splitting. From Fig.35(b), we can see that the H_0^+ peak (the highest field peak in the TMR) and the series of H_N^+ peaks cannot appear, whereas the series of H_N^- peaks can appear in the LMR, and that the series of H_N^+ and H_N^- peaks can appear in the TMR, though the intensity of H_N^+ series is stronger than that of H_N^- series, considering the number of upward arrows.

Next, we consider the case, $\hbar\omega_c < g\mu_B H$. It can be seen from Fig.35(a) that H_1^- (in this case, the highest field peak in the TMR) and the series of H_N^- oscillatory peaks cannot appear though H_N^+ peaks including H_0^+ peak can appear in the LMR, and that the oscillatory peaks, H_N^- and H_N^+ series including H_0^+ peak can appear in the TMR. In this case, the intensity of H_N^+ series is stronger than that of H_N^- series, if we compare the number of upward arrows

If we compare the present experimental results with the above discussion, and if we restrict the discussion within the peak missing in the LMR, both energy level schemes are acceptable. However, if we discuss the intensity of oscillatory peaks, the present experimental results can be better explained by the latter case (Fig.35(a)), if the transition probabilities, $N\uparrow \rightleftarrows (N-1)\uparrow$ and $N\downarrow \rightleftarrows (N-1)\downarrow$, are equal.

On the other hand, in the actual band electron picture, according to the discussion by Éfros,[42)] the H_0^+ peak is missing, since the transition $0\uparrow \rightleftarrows 0\downarrow$ does not occur, whereas the H_1^- peak can appear in the LMR for both the conditions, $g\mu_B H > \hbar\omega_c$ and $g\mu_B H < \hbar\omega_c$, and all the peaks, H_0^+, H_1^-, H_1^+, --- can appear for low quantum numbers in the TMR as discussed in the preceding section. Then if $\hbar\omega_c > g\mu_B H$, the highest field peak (ie. H_0^+) is missing, however if $\hbar\omega_c < g\mu_B H$, the highest field peak (ie. H_1^-) appears though the second highest field peak (ie. H_0^+ in this case) is missing in the LMR. On the other hand, all the peaks (for low N) will be observed in the TMR for both the conditions, $g\mu_B H > \hbar\omega_c$ and $g\mu_B H < \hbar\omega_c$. Thus, in the band electron picture, since the H_0^+ peak cannot appear in the LMR, $\hbar\omega_c$ must be greater than $g\mu_B H$.

Moreover, if we take the spin-flip scattering by non-magnetic impurity potential (ie. spin independent), which is possible in the actual band electron picture, the amplitude of the higher field side peak of a pair peaks will be smaller, if the energy separation of the corresponding energy levels is small and their spins are different, since the density of states of each Landau levels have tailes toward higher energy side. Thus the assumption that $\hbar\omega_c > g\mu_B H$ is consistent with the present experimental results.

In addition, there is another experimental evidence that $\hbar\omega_c > g\mu_B H$: the magnetic field dependence of the laser emission wavelength reported bt Harman47) also suggests directly that $\hbar\omega_c > g\mu_B H$ for alloys with PbTe-side composition of the crossover.

Though the results of the measurements of electroreflectance for PbTe reported by Glosser et al.106) indicate that the highest valence band has the same parity as the upper two conduction bands and the lowest conduction band has the same parity as the lower two valence bands, being different from the so far accepted one (see Figs. 27 and 33), almost all the theoretical works upon the band structure, except for one calculated by Conklin et al.,77) support the so far accepted band ordering, where the spin splitting becomes smaller than the Landau level separation for alloys with the PbTe-side composition of the crossover as discussed in chapter VII.1.B.

For the scattering processes, as both the scattering due to the spin-orbit interaction (free electron picture) and the spin-flip scattering arises from the mixing of the different spin states of the actual band wave functions (band electron picture) can well interpret the present experimental results, we cannot discuss further which process is important in $Pb_{1-x}Sn_xTe$.

Though the introduction of the spin-orbit term in the perturbing Hamiltonian by Suizu and Narita37) seems to be particular and is lacking generality, the scatterer in almost all the materials where the spin effects were so far observed, are the vacancies of heavy elements, such as Te and Sb atoms. Thus the scatterer is common for almost all the materials.

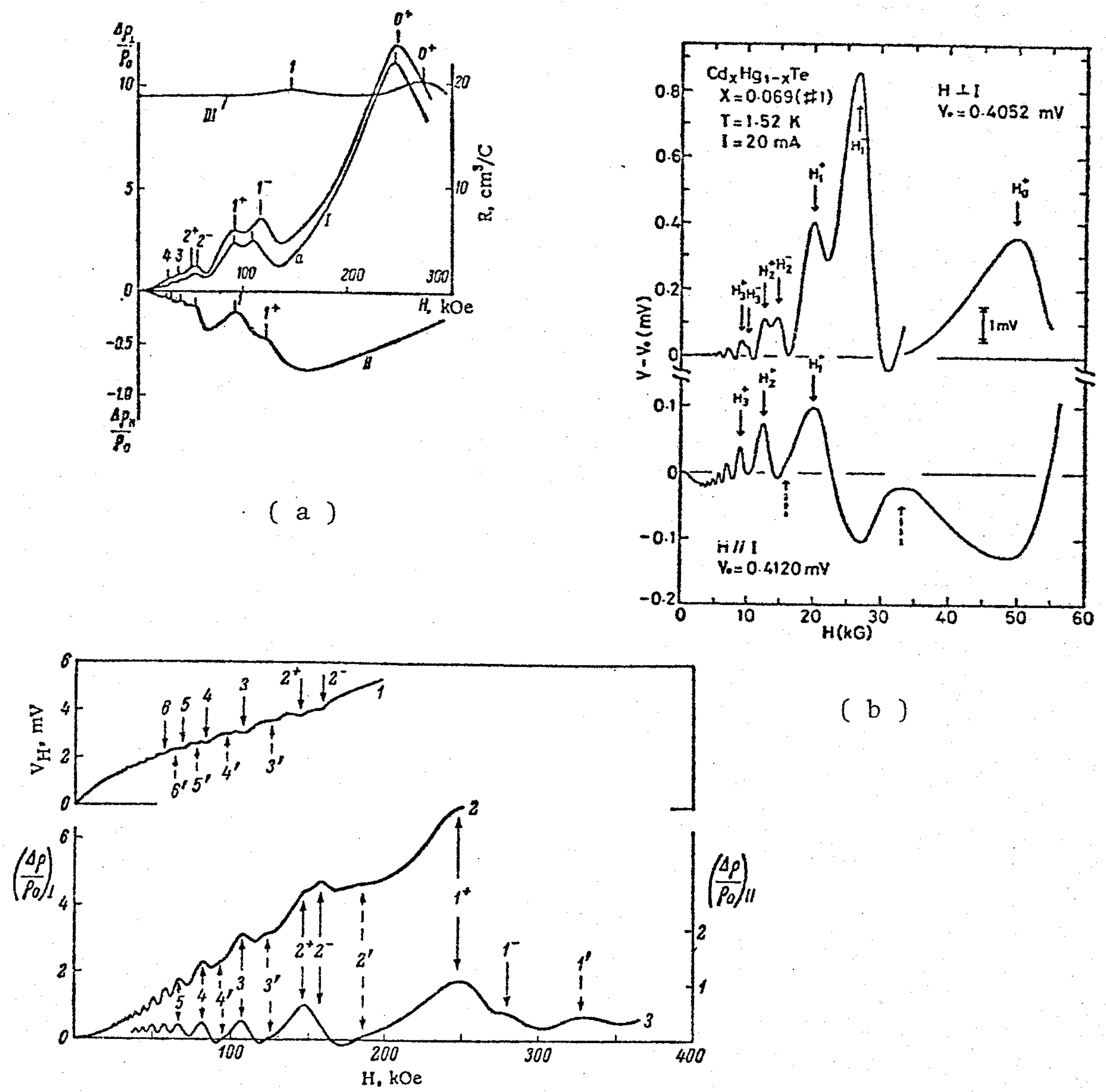

(a)

(b)

(c)

Fig.34 (a) Transverse magnetoresistance (I), longitudinal magnetoresistance (II), and Hall coefficient (III) for InSb with $n=1.66\times10^{17}$ cm^{-3}, as a function of magnetic field. After Amirkhanov and Bashrov.[36)]

(b) Transverse (upper part) and longitudinal (lower part) magnetoresistance for $Hg_{1-x}Cd_xTe$ with $x=0.069$ and $n=3.14\times10^{16}$ cm^{-3}, as a function of magnetic field. After Suizu and Narita.[37)]

(c) Transverse (upper part) and longitudinal (lower part) magnetoresistance for GaSb with $n=2.10\times10^{18}$ cm^{-3}, as a function of magnetic field. After Mashovets et al..[105)]

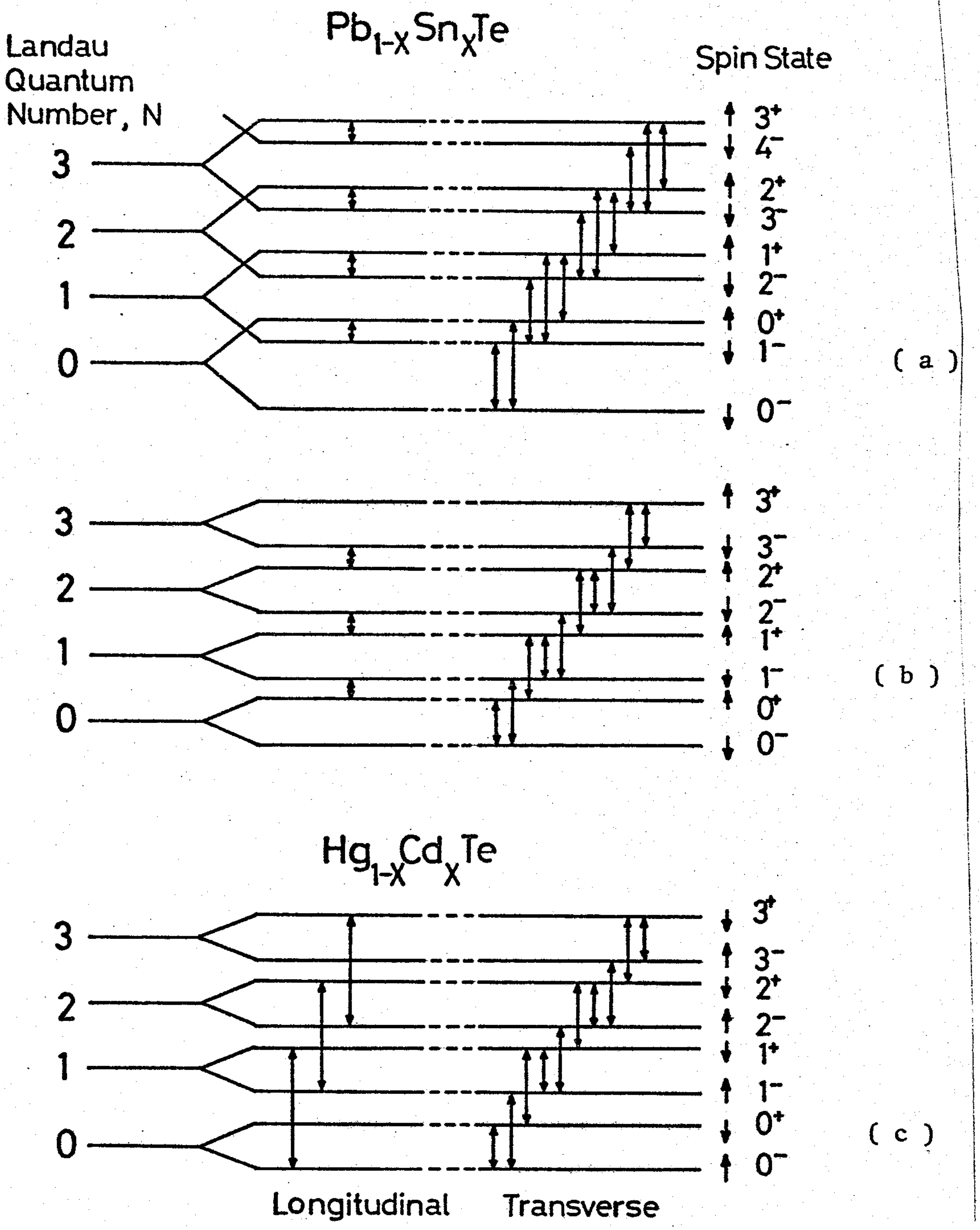

Fig.35 Schematic diagrams representing the selection rules for the scattering transitions between Landau sublevels in transverse and longitudinal magnetoresistances:

(a) Diagram for n-$Pb_{1-x}Sn_xTe$, when $m_c^*|g|/2m > 1$ ($g > 0$),

(b) Diagram for n-$Pb_{1-x}Sn_xTe$, when $m_c^*|g|/2m < 1$ ($g > 0$),

(c) Diagram for $Hg_{1-x}Cd_xTe$, with $m_c^*|g|/2m < 1$ ($g < 0$).

Table II. Coefficients of non-zero matrix elements appear in the scattering transitions, $(0,N,\sigma) \rightleftarrows (k_H,N',\sigma')$.

	$\hbar\omega_c > g\mu_B H$	$\hbar\omega_c < g\mu_B H$
$0\downarrow \rightleftarrows 0\uparrow$	$A^{0*}_{c\uparrow,c\downarrow}A^{0}_{c\downarrow,v\downarrow}$	$A^{0*}_{c\uparrow,v\downarrow}A^{0}_{c\downarrow,v\downarrow}$
$0\downarrow \rightleftarrows N'\downarrow$	$A^{0*}_{c\downarrow,v\downarrow}A^{N'}_{c\downarrow,c\downarrow}$	$A^{0*}_{c\downarrow,c\downarrow}A^{N'}_{c\downarrow,c\downarrow}$
$0\downarrow \rightleftarrows N'\uparrow$	$A^{0*}_{c\downarrow,c\downarrow}A^{N'}_{c\uparrow,c\uparrow}$	$A^{0*}_{c\downarrow,c\downarrow}A^{N'}_{c\uparrow,c\uparrow}$
$0\uparrow \rightleftarrows N'\uparrow$	$A^{0*}_{c\uparrow,c\uparrow}A^{N'}_{c\uparrow,c\uparrow} + A^{0*}_{c\uparrow,v\downarrow}A^{N'}_{c\uparrow,v\downarrow}$	same to the left
$0\uparrow \rightleftarrows N'\downarrow$	$A^{0*}_{c\uparrow,c\uparrow}A^{N'}_{c\downarrow,c\uparrow} + A^{0*}_{c\uparrow,v\downarrow}A^{N'}_{c\downarrow,v\downarrow}$	same to the left
$N\downarrow \rightleftarrows N'\downarrow$	$A^{N*}_{c\downarrow,c\downarrow}A^{N'}_{c\downarrow,c\downarrow} + A^{N*}_{c\downarrow,v\uparrow}A^{N'}_{c\downarrow,v\uparrow}$ (for $N \leqq N'$)	same to the left
$N\uparrow \rightleftarrows N'\uparrow$	$A^{N*}_{c\uparrow,c\uparrow}A^{N'}_{c\uparrow,c\uparrow} + A^{N*}_{c\uparrow,v\downarrow}A^{N'}_{c\uparrow,v\downarrow}$ (for $N \leqq N'$)	same to the left
$N\downarrow \rightleftarrows N'\uparrow$	$A^{N*}_{c\downarrow,c\downarrow}A^{N'}_{c\uparrow,c\downarrow} + A^{N*}_{c\downarrow,v\uparrow}A^{N'}_{c\uparrow,v\uparrow}$ (for $N \leqq N'$)	same to the left (for $N \leqq N'$) $A^{N*}_{c\uparrow,c\downarrow}A^{N'}_{c\downarrow,c\downarrow} + A^{N*}_{c\uparrow,v\uparrow}A^{N'}_{c\downarrow,v\uparrow}$ (for $N=N'-1$)
$N\uparrow \rightleftarrows N'\downarrow$	$A^{N*}_{c\uparrow,c\uparrow}A^{N'}_{c\downarrow,c\uparrow} + A^{N*}_{c\uparrow,v\downarrow}A^{N'}_{c\downarrow,v\downarrow}$ (for $N \leqq N'$)	same to the left (for $N \leqq N'$) $A^{N*}_{c\downarrow,c\uparrow}A^{N'}_{c\uparrow,c\uparrow} + A^{N*}_{c\downarrow,v\downarrow}A^{N'}_{c\uparrow,v\downarrow}$ (for $N=N'-1$)

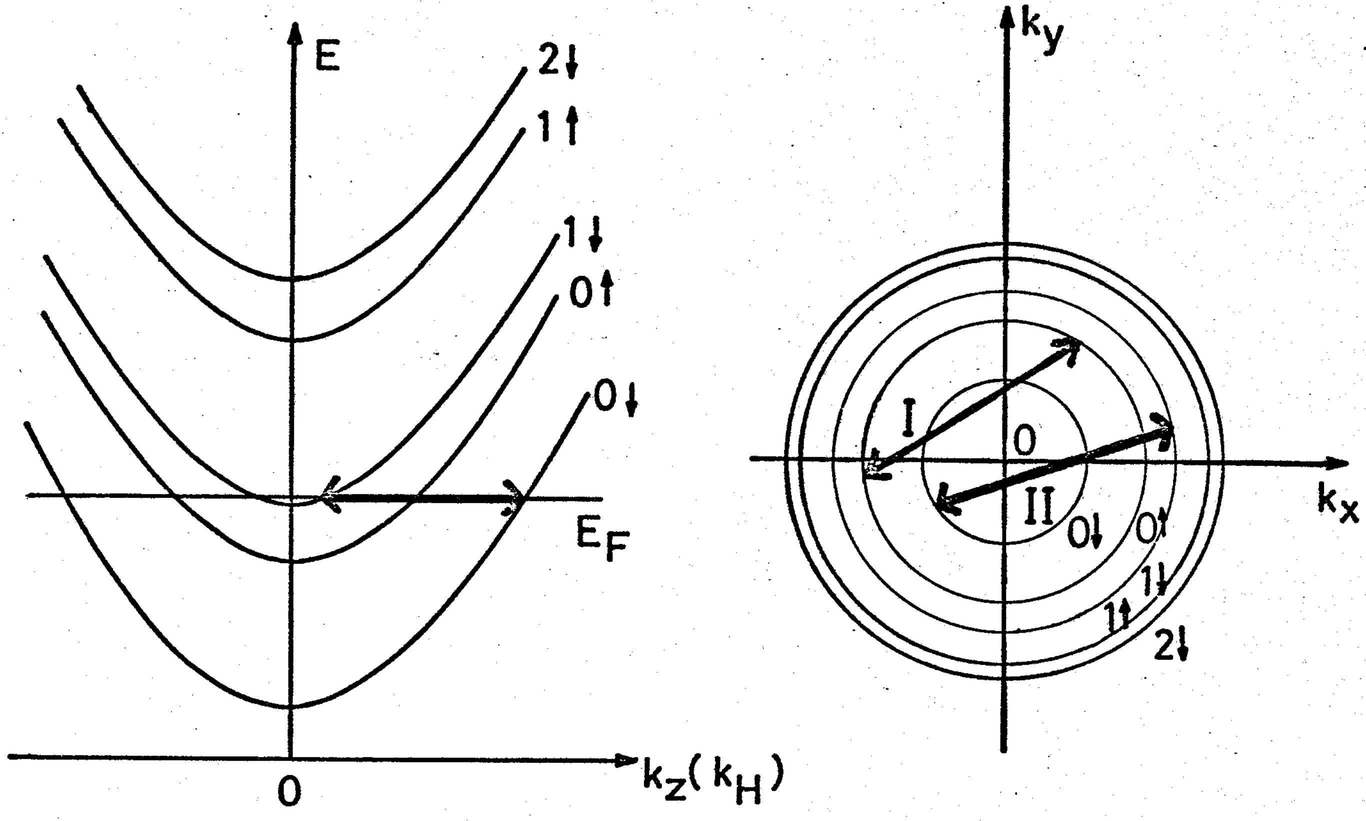

(a)

(b)

Fig.36 (a) Elastic scattering changing k_z, which gives rise to the longitudinal magnetoresistance.

(b) Elastic scattering changing k_x and k_y at $k_z \simeq 0$. I represents the transition which does not change quantum number N and spin, while II represents the transition which does not change spin but changes quantum number N.

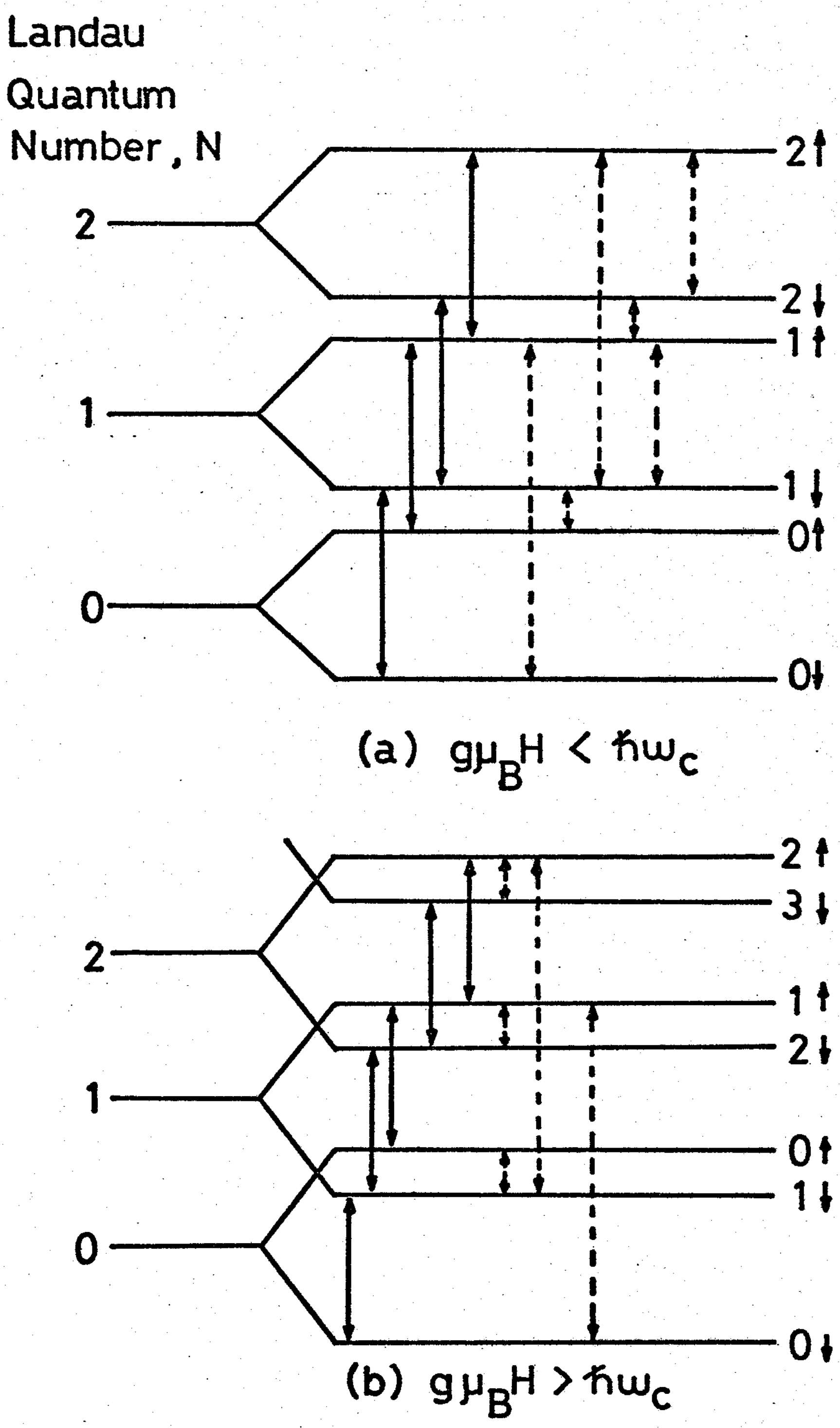

Fig.37 Possible interlevel transitions in the band electron picture for the LMR of n-type $Pb_{1-x}Sn_xTe$. (a) represents the case, when $g\mu_B H < \hbar\omega_c$, while (b) represents the case, when $g\mu_B H > \hbar\omega_c$. Solid lines indicate the transitions which does not change spin and dashed lines indicate the spin-flip scattering transitions. For simplicity, only $\Delta N=1$ cases are indicated for both type transitions

VIII. Summary and Conclusion

We have presented a detailed experimental study of the SdH effect on n-type $Pb_{1-x}Sn_xTe$ alloy crystals. For the first time in n-type material the informations concerning the conduction band edge structure such as the shape of the Fermi surface, effective mass, and effective g-value (or the spin splitting factor ν) have been obtained as a function of alloy composition. The shape of the Fermi surface was investigated through the measurements of the angular dependence of the extremal cross sections, which gave the prolate [111] ellipsoidal surface at least within the experimental error. Anisotropy constant K increases with decreasing energy gap. The spin splitting factor ν approaches to unity when the energy gap approaches to zero.

Though these results are considerably different from those obtained by Cuff et al.,55) the results obtained by Melngailis et al.39) on p-type $Pb_{1-x}Sn_xTe$, and the results obtained by Nii57) on n- and p-type PbTe, are closely similar to the present results on n-type materials. These facts that the properties of both the conduction and the valence bands are closely similar, seem to indicate that the $\vec{k}\cdot\vec{p}$ interaction between the quasi degenerate conduction and valence bands are important.

In fact, fitting the transverse ($P_\perp$) and the longitudinal ($P_\parallel$) momentum matrix elements to the two-band model gives satisfactory agreement with the present experimental results. Moreover, the energy gaps are obtained from the analysis in the two band model, which give the fair agreement with the previous experimental results on the laser emission47) and the photo-diode.48)

Though the analysis by the two-band model gives the fair agreement with the experimental results, the appearance of the spin splittings

indicates that there are interactions with the remote bands even though they are the second order effects. The spin splittings were observed in almost all the samples studied for the TMR, however in the LMR no spin splitting was observed. The difference of the spin effects between the TMR and LMR has been made accurate for the first time in this material, from the studies on the TMR and LMR in the quantum limit region.
The most striking feature of the spin effects is that the highest field oscillatory peak only observed in the TMR is completely missing in the LMR. This feature is different from the known feature of the LMR in some other narrow gap materials, such as InSb,36) $Hg_{1-x}Cd_xTe$,37,95) and so on, where two highest field peaks appear in the TMR are missing in the LMR, which is, so far as we know, the common to the narrow gap materials with the grey-tin type band structure. Moreover, for the lower field oscillation, high field side of the pair peaks in the TMR are weak and are completely missing in the LMR.

In order to interpret this anomalous features of the SdH oscillations, we refered the theory on the spin effect in the oscillatory magnetoresistance given by Suizu and Narita,37,43) and in terms of their selection rules the anomalous features of the LMR can well be interpreted. In addition, we have considered the spin-flip scattering transition by non-magnetic (independent of spin) impurities, which is possible in the band electron picture. The anomalous behavior of the LMR can also be well interpreted by the band electron picture.

From the discussion upon the peak missing, we have assigned the oscillatory peaks and reached the conclusion that the spin-Zeeman splitting is smaller than the Landau level separation for the materials with the composition of PbTe-side of the crossover.
Though we can interpret the present experimental results by considering

the spin-flip scattering in the band electron picture and the spin-flip scattering due to the spin-orbit interaction in the free electron picture, the problem for the peak intensity of the spin splitting pair peaks, especially in the LMR, remains somewhat obscure.

Thus to confirm the discussin upon the peak missing and the peak intensity, the experimental study on the spin effect of the oscillatory magnetoresistance for the alloys with the composition of SnTe-side of the crossover will be helpful. However the preparation of the materials with SnTe -side composition is very difficult, thus the future experimental study concerning the spin effect of the SdH oscillations in the quantum limit region of another materials as well as the theoretical study on the spin effect of the SdH oscillation where the spin-flip scattering, spin-orbit interaction, and the broadening are rigorously taken into account in the band electron picture are desired.

Appendix. A

A.1 When the sample is rotated in the (110) plane.

For pocket A,

$$\cos\alpha = \cos(\theta - \cos^{-1}\sqrt{2/3}) ,$$

and the period is

$$P(\theta) = (\frac{2e}{c})K^{-1/6}[1+(K-1)\cos^2(\theta-\cos^{-1}\sqrt{2/3})]^{1/2}(3\pi^2(n/4))^{-2/3} . \qquad (A.1)$$

For pocket B,

$$\cos\alpha = \cos(\theta + \cos^{-1}\sqrt{2/3}) ,$$

and the period is

$$P(\theta) = (\frac{2e}{c})K^{-1/6}[1+(K-1)\cos^2(\theta+\cos^{-1}\sqrt{2/3})]^{1/2}(3\pi^2(n/4))^{-2/3} . \qquad (A.2)$$

For pocket C,

$$\cos\alpha = 1/\sqrt{3}\,\sin\theta ,$$

and the period is

$$P(\theta) = (\frac{2e}{c})K^{-1/6}[1+\frac{(K-1)}{3}\sin^2\theta]^{1/2}(3\pi^2(n/4))^{-2/3} . \qquad (A.3)$$

A.2. When the sample is rotated in the (100) plane.

For pocket A,

$$\cos\alpha = 1/\sqrt{3}\,(\sin\theta + \cos\theta) ,$$

and the period is

$$P(\theta) = (\frac{2e}{c})K^{-1/6}[1+\frac{(K-1)}{3}(\sin\theta + \cos\theta)^2]^{1/2}(3\pi^2(n/4))^{-2/3} . \qquad (A.4)$$

For pocket B,

$$\cos\alpha = 1/\sqrt{3}\,(\sin\theta - \cos\theta) ,$$

and the period is

$$P(\theta) = (\frac{2e}{c})K^{-1/6}[1+\frac{(K-1)}{3}(\sin\theta - \cos\theta)^2]^{1/2}(3\pi^2(n/4))^{-2/3} . \qquad (A.5)$$

Appendix. B

When $\vec{H} = (0,0,H_z)$ and the gauge, $\vec{A} = \frac{1}{2}(\vec{H}\times\vec{r})$, is used,

$$\vec{k} = \frac{1}{\hbar}\left(P_x - \frac{ey}{2c} H_z ,\ P_y + \frac{ex}{2c} H_z ,\ P_z \right) . \qquad (\text{B-1})$$

The commutator of k becomes

$$\begin{aligned} &[k_x,k_x] = [k_y,k_y] = [k_z,k_z] = 0 \\ &[k_x,k_y] = -i eH_z/c\hbar \\ &[k_y,k_z] = [k_z,k_x] = 0 \quad . \end{aligned} \qquad (\text{B-2})$$

If we write $k^{\pm} = (k_x \pm i k_y)$,

$$[k^-,k^+] = \frac{2e}{c\hbar} H_z \ . \qquad (\text{B-3})$$

Then we introduce a number operator,

$$a^\dagger = \sqrt{\frac{c\hbar}{2eH_z}}\ k^+ \ , \qquad (\text{B-4.a})$$

$$a = \sqrt{\frac{c\hbar}{2eH_z}}\ k^- \ . \qquad (\text{B-4.b})$$

From eqs. (B-3) and (B-4.a) and (B-4.b) ,

$$[a,a^\dagger] = 1 \ . \qquad (\text{B-5})$$

Thus the effective 4 × 4 Hamiltonian becomes,

$$\begin{array}{cc} & \begin{array}{cccc} |L_6^-\uparrow\rangle & |L_6^+\downarrow\rangle & |L_6^-\downarrow\rangle & |L_6^+\uparrow\rangle \end{array} \\ \hat{H}_{\mathrm{eff}} = & \left(\begin{array}{cccc} \begin{array}{l} \frac{E_G}{2} + \hbar\tilde{\omega}_c(a^\dagger a + \frac{1}{2}) \\ +\mu_B(\cos^2\theta^- - \sin^2\theta^-)H_z \end{array} & (\frac{\hbar}{m})P_\perp \frac{2m\tilde{\omega}_c}{\hbar}\, a & 0 & 0 \\ (\frac{\hbar}{m})P_\perp \frac{2m\tilde{\omega}_c}{\hbar}\, a^\dagger & \begin{array}{l} -\frac{E_G}{2} + \hbar\tilde{\omega}_c(a^\dagger a + \frac{1}{2}) \\ -\mu_B(\cos^2\theta^+ - \sin^2\theta^+)H_z \end{array} & 0 & 0 \\ 0 & 0 & \begin{array}{l} \frac{E_G}{2} + \hbar\tilde{\omega}_c(a^\dagger a + \frac{1}{2}) \\ -\mu_B(\cos^2\theta^- - \sin^2\theta^-)H_z \end{array} & (\frac{\hbar}{m})P_\perp \frac{2m\tilde{\omega}_c}{\hbar}\, a^\dagger \\ 0 & 0 & (\frac{\hbar}{m})P_\perp \frac{2m\tilde{\omega}_c}{\hbar}\, a & \begin{array}{l} -\frac{E_G}{2} + \hbar\tilde{\omega}_c(a^\dagger a + \frac{1}{2}) \\ +\mu_B(\cos^2\theta^+ - \sin^2\theta^+)H_z \end{array} \end{array} \right) \end{array} , \qquad (\text{B-6})$$

where $\hbar\tilde{\omega}_c = \hbar \frac{eH_z}{mc}$.

Thus 4 × 4 matrix can be decoupled into 2 × 2 matrix.

The energy can be obtained exactly from two 2 × 2 secular equations.

Thus

$$E^{c}_{N,\sigma}= \hbar\tilde{\omega}_{c}(N + \tfrac{1}{2}) +\mu_{B}(\cos^{2}\theta^{-}-\sin^{2}\theta^{-}-\cos^{2}\theta^{+}+\sin^{2}\theta^{+})SH_{z}$$
$$+ \sqrt{[\tfrac{E_{G}}{2} +\mu_{B}(\cos^{2}\theta^{-}-\sin^{2}\theta^{-}+\cos^{2}\theta^{+}+\sin^{2}\theta^{+})SH_{z}]^{2}+ (\tfrac{\hbar}{m})^{2}P_{\perp}^{2}\,\tfrac{2m\tilde{\omega}_{c}}{\hbar}[(N+ \tfrac{1}{2})+S]} ,$$

(B-7.a)

$$E^{V}_{N,\sigma}= \hbar\tilde{\omega}_{c}(N + \tfrac{1}{2}) -\mu_{B}(\cos^{2}\theta^{-}-\sin^{2}\theta^{-}-\cos^{2}\theta^{+}+\sin^{2}\theta^{+})SH_{z}$$
$$- \sqrt{[\tfrac{E_{G}}{2} -\mu_{B}(\cos^{2}\theta^{-}-\sin^{2}\theta^{-}+\cos^{2}\theta^{+}-\sin^{2}\theta^{+})SH_{z}]^{2}+ (\tfrac{\hbar}{m})^{2}P_{\perp}^{2}\,\tfrac{2m\tilde{\omega}_{c}}{\hbar}[(N+ \tfrac{1}{2})-S]} ,$$

(B-7.b)

Where $S = \frac{1}{2}$ for $\sigma = \uparrow$, $S = -\frac{1}{2}$ for $\sigma = \downarrow$, N is the Landau quantum number, and C and V refer to the conduction and the valence band, respectively. The conduction band g-factor is obtained from the equation, $E^{c}_{N\uparrow}- E^{c}_{N\downarrow} = g^{c}\mu_{B}H_{z}$.

Thus, when H_z is very small and $E_{G} >> [(\cos^{2}\theta^{-}- \sin^{2}\theta^{-}) \pm (\cos^{2}\theta^{+}- \sin^{2}\theta^{+})]\mu_{B}H_{z}$ holds,

$$E^{c}_{N\uparrow} - E^{c}_{N\downarrow} \simeq\mu_{B}(\cos^{2}\theta^{-}-\sin^{2}\theta^{-}-\cos^{2}\theta^{+}+\sin^{2}\theta^{+})H_{z}$$
$$+[(\tfrac{E_{G}}{2}+\tfrac{\mu_{B}}{2}(\cos^{2}\theta^{-}-\sin^{2}\theta^{-}+\cos^{2}\theta^{+}+\sin^{2}\theta^{+})H_{z})$$
$$+ \frac{1}{2}\frac{(\frac{\hbar}{m})^{2}P_{\perp}^{2}\,\frac{m\tilde{\omega}_{c}}{\hbar}((N+1/2)+1/2)}{\frac{E_{G}}{2} +\frac{\mu_{B}}{2}(\cos^{2}\theta^{-}-\sin^{2}\theta^{-}+\cos^{2}\theta^{+}-\sin^{2}\theta^{+})H_{z}}]$$
$$-[(\tfrac{E_{G}}{2} -\tfrac{\mu_{B}}{2}(\cos^{2}\ ^{-}-\sin^{2}\ ^{-}+\cos^{2}\ ^{+}-\sin^{2}\ ^{+})H_{z})$$
$$+ \frac{1}{2}\frac{(\frac{\hbar}{m})^{2}P_{\perp}^{2}\,\frac{m\tilde{\omega}_{c}}{\hbar}((N+1/2)-1/2)}{\frac{E_{G}}{2} -\frac{\mu_{B}}{2}(\cos^{2}\theta -\sin^{2}\theta^{-}+\cos^{2}\theta^{+}-\sin^{2}\theta^{+})H_{z}}]$$

$$\simeq[2\mu_{B}(\cos^{2}\theta^{-}-\sin^{2}\theta^{-})+(\tfrac{\hbar}{m})^{2}P_{\perp}^{2}\,\tfrac{1}{E_{G}}(\tfrac{m\tilde{\omega}_{c}}{\hbar})] ,\qquad (B-8)$$

and

$$g^{c}_{1} = 2[(\cos^{2}\theta^{-}-\sin^{2}\theta^{-}) + \frac{2P_{\perp}^{2}}{mE_{G}}] .\qquad (B-9)$$

Appendix C

The Hamiltonian describing the motion of an electron in a periodic lattice potential under the static magnetic field is

$$H_o = \frac{\vec{P}^2}{2m} + \frac{\hbar}{4m^2c^2}\,\vec{\sigma}\cdot(\vec{\nabla}V\times\vec{P}) + \mu_B\vec{H}\cdot\vec{\sigma} + V(\vec{r}) \;, \qquad (\text{C-1})$$

where $\vec{P} = \vec{p} + \frac{e}{c}\vec{A}$, $\vec{p} = -i\hbar\vec{\nabla}$, $\vec{A} = (0,H_x,0)$ is the vector potential, $V(\vec{r})$ is the lattice potential, and μ_B is the Bohr magneton. In the effective mass approximation, this can be written

$$H_o = \frac{\vec{P}^2}{2m} + g\,\frac{\mu_B}{2}\,\vec{H}\cdot\vec{\sigma} \;.$$

where the free electrons in the conduction band comes close to the impurity atoms or lattice vacancy, possibly the Te atom vacancy, to get into the orbit of the scattering center, they are scattered. Here we consider the scattering is due to the spin-orbit interactions with the scattering centers, and treat this as a perturvation, which can be written as

$$H_{so} = \sum_j \frac{\hbar}{4m^{*2}c^2}\;U(\vec{r}-\vec{r}_j)\times\vec{P}\cdot\vec{\sigma} \;, \qquad (\text{C-2})$$

where $\vec{r}_j$ is the position of the scattering center, and $U(\vec{r}-\vec{r}_j)$ is their potential. For sinplicity, we consider that an electron is scattered by a scattering center due either to the spin-orbit interaction or to the usual coulomb interaction. Then the perturbation becomes

$$H' = \frac{\hbar}{4m^{*2}c^2}\,\vec{\nabla}U(\vec{r}-\vec{r}_o)\times\vec{P}\cdot\vec{\sigma} + W \;, \qquad (\text{C-3})$$

where $\vec{r}_o$ is the position of a scattering center, and W is the scattering potential. The total Hamiltonian is

$$\begin{aligned} H &= H_o + H' \\ &= \frac{\vec{P}^2}{2m^*} + \frac{1}{2}g\mu_B\vec{H}\cdot\vec{\sigma} + \frac{\hbar}{4m^{*2}c^2}\vec{\nabla}U\times\vec{P}\cdot\vec{\sigma} + W \;, \end{aligned} \qquad (\text{C-4})$$

Though we consider the transport phenomena, we neglect the term concerning the electric field required for the current flow.

If we choose the Landau gauge $\vec{A} = (0, H_x, 0)$ the equation of motion for the center of the cyclotron motion of an electron is

$$\dot{\vec{X}} = \frac{i}{\hbar}[H,\vec{X}] = \frac{\vec{P}}{m^*} - D\vec{\sigma} \times \vec{X} + \frac{i}{\hbar}[W,\vec{X}] \; , \qquad (\text{C-5})$$

where $\vec{X} = [x + k_y \frac{m^* \omega_c}{\hbar} , y, z]$ is the coordinate of the center of the cyclotron motion, and

$$D = - \frac{1}{4m^* c^2} \frac{1}{r - r_o} \frac{\partial U(\vec{r}-\vec{r}_o)}{\partial(\vec{r}-\vec{r}_o)} \; . \qquad (\text{C-6})$$

The eigen states corresponding to the conduction and the valence band of the unperturbed Hamiltonian H_o is the doubly degenerate Kramer's pairs given in Appendix B.(eqs.B.7,a and b). Though they are not pure spin up or down states but mixed states due to the strong spin-orbit interactions, their spin states are almost rather up or down states. Thus we approximate the wave functions of the conduction or valence band to be a pair of pure spin up and down state as

$$\Psi_N = C \exp[i(k_y y + k_z z)] \; \phi_N(X) S \quad , \qquad (\text{C-7})$$

where $S = \alpha(\uparrow)$ or $\beta(\downarrow)$, and ϕ_N is the harmonic oscillator wave function of the Landau quantum number N.

As we are concerned in the transverse and longitudinal magnetoresistances, we refer to the general formulae for the electronic conductivity in the presence of the magnetic field given by Kubo et al.107) we obtain

$$\sigma_{\parallel} = \frac{\pi\hbar e^2}{\Omega} \int_{-\infty}^{\infty} dE\left(- \frac{\partial f}{\partial E}\right) < Tr[\delta(E-H)\dot{z}\delta(E-H)\dot{z}] >_{sc} \qquad (\text{C-8})$$

and

$$\sigma_{\perp} = \frac{\pi he^2}{\Omega} \int_{-\infty}^{\infty} dE\left(- \frac{\partial f}{\partial E}\right) < Tr[\delta(E-H)\dot{X}\delta(E-H)\dot{X}] >_{sc} \; , \qquad (\text{C 9})$$

where $\langle \cdots \rangle_{sc}$ means the average for the scattering centers, and Ω is the unit volume. As we are treating the scattering Hamiltonian as the perturbation, the lowest order expressions for $\sigma_{\parallel}$ and $\sigma_{\perp}$ are given by substituting the total Hamiltoinan by the diagonal elements of the unperturbed Hamiltonian H_o in the above expressions. The unperturbed Hamiltonian H_o can be weitten as follows,

$$H_o = (N + \frac{1}{2})\hbar\omega_c \pm \frac{1}{2}|g|\mu_B H + \frac{P_z^2}{2m^*} \;, \qquad \text{(C-10)}$$

Appendix D.

In order to obtain the Landau level wave functions, Adler et al.[85)] carried out a two-step coordinate transformation, the first step being the scale change according to the relative sizes of $P_\perp$ and $P_\parallel$, the second step being a rotation to align the z-axis of the final coordinate system with the transformed magnetic field. In this case the eigenfunction for the transformed Hamiltonian is given by the following equation,

$$\psi^{N,k_H,k_y}_{\mu,\sigma} = \sum_{\mu',\sigma'} C^{N,k_H,k_y}_{\mu',\sigma'\mu,\sigma}(\vec{r})\ \psi^{T}_{\mu',\sigma'}(\vec{r}) \ , \qquad (\text{ D.1 })$$

where N is the Landau quantum number, k_H is the wave vector in the direction of the magnetic field, μ is the band index, σ is the spin index ($\sigma=1$ for spin up and $\sigma=0$ for spin down), and $\psi^T_{\mu',\sigma'}$ is the band edge Bloch state in the transformed coordinate system, which is given by the following equation,

$$\begin{pmatrix} \psi^T_{c\uparrow} \\ \psi^T_{c\downarrow} \\ \psi^T_{v\uparrow} \\ \psi^T_{v\downarrow} \end{pmatrix} = \begin{pmatrix} \cos\frac{\beta}{2} & \sin\frac{\beta}{2} & 0 & 0 \\ -\sin\frac{\beta}{2} & \cos\frac{\beta}{2} & 0 & 0 \\ 0 & & \cos\frac{\beta}{2} & \sin\frac{\beta}{2} \\ 0 & & -\sin\frac{\beta}{2} & \cos\frac{\beta}{2} \end{pmatrix} \begin{pmatrix} |L^-_6\uparrow\rangle \\ |L^-_6\downarrow\rangle \\ |L^+_6\uparrow\rangle \\ |L^+_6\downarrow\rangle \end{pmatrix} ,$$

where $\sin\beta=\lambda_x P_\perp P_\parallel / P^2_H$, $P^2_H = (\lambda^2_z P^4_\perp + \lambda^2_x P^2_\perp P^2_\parallel)^{1/2}$ for a magnetic field with direction cosines λ_x and λ_z, and $|L^-_6\uparrow\rangle$ etc. are given by eq.(VII.1). The transformed Bloch states are orthogonal, that is,

$$\int_{\text{cell}} \psi^{T^*}_{\mu',\sigma'}(\vec{r})\ \psi^T_{\mu,\sigma}(\vec{r})d\vec{r} = \delta_{\mu',\mu}\delta_{\sigma',\sigma} \ .$$

The form of the amplitude function $C(\vec{r})$ is given as follows:

$$C^{N,k_H,k_y}_{\mu\sigma,\mu'\sigma'}(\vec{r})=A^N_{\mu\sigma,\mu'\sigma'}(k_H)\ \phi_{N+\sigma-\sigma'}(u)\ e^{i(\ \eta k_H z' - k_y y\ )} \ ,$$

where $\phi_{N+\sigma-\sigma'}(u)$ is the harmonic oscillator wave function of order ($N+\sigma-\sigma'$), $u=x'/\xi + \xi(P_\perp/m)/k_y$, $\xi^2=\hbar c/eH$, $\eta=P^2_\perp P_\parallel / P^2_H$, $x'=\frac{\cos\beta}{P_\perp/m}x - \frac{\sin\beta}{P_\parallel/m} z$,

$z'= \frac{\sin\beta}{P_\perp/m} x + \frac{\cos\beta}{P_\parallel/m} z$, and $A^N_{\mu\sigma,\mu'\sigma'}(k_H)$ is the coefficients which are given by diagonalizing the transformed Hamiltonian.

In the transformed coordinate, the two-band Hamiltonian (B.6) becomes,

$$\hat{H}_t = \begin{pmatrix} \frac{E_G}{2} + \hbar\Omega^-(a^\dagger a + \frac{1}{2}) + \frac{\hbar^2 k_H^2}{2m_H^-} + \frac{1}{2} G^- \mu_B H & i\sqrt{E_G\hbar\Omega}\, a & 0 & \sqrt{\frac{E_G}{2M}}\,\hbar k_H \\ -i\sqrt{E_G\hbar\Omega}\, a^\dagger & -\frac{E_G}{2} + \hbar\Omega^+(a^\dagger a + \frac{1}{2}) + \frac{\hbar^2 k_H^2}{2m_H^+} - \frac{1}{2} G^+ \mu_B H & \sqrt{\frac{E_G}{2M}}\,\hbar k_H & 0 \\ 0 & -\sqrt{\frac{E_G}{2M}}\,\hbar k_H & \frac{E_G}{2} + \hbar\Omega^-(a^\dagger a + \frac{1}{2}) + \frac{\hbar^2 k_H^2}{2m_H^-} - \frac{1}{2} G^- \mu_B H & -i\sqrt{E_G\hbar\Omega}\, a^\dagger \\ \sqrt{\frac{E_G}{2M}}\,\hbar k_H & 0 & i\sqrt{E_G\hbar\Omega}\, a & -\frac{E_G}{2} + \hbar\Omega^+(a^\dagger a + \frac{1}{2}) + \frac{\hbar^2 k_H^2}{2m_H^+} + \frac{1}{2} G^+ \mu_B H \end{pmatrix}, \quad (D.2)$$

where $M = \frac{\lambda_x^2 E_G}{2P_\perp^2/m^2} + \frac{\lambda_z^2 E_G}{2P_\parallel^2/m^2} = \frac{E_G P_H^4}{P_\perp^4 P_\parallel^2}$, $m_H^\pm = \mp m/(\lambda_x^2 + \lambda_z^2)$, $\Omega = \frac{eH}{c}\frac{2P_H^2}{m^2 E_G}$,

$\Omega^\pm = \frac{eH}{mc}(\lambda_x^2 + \lambda_z^2)^{1/2}$, and $G^\pm = \frac{2}{P_H^2}[\lambda_z^2 P_\perp^2(\cos^2\theta^\pm - \sin^2\theta^\pm) \mp \lambda_x^2 P_\parallel P_\perp \cos^2\theta^\pm]$.

When $k_H = 0$, above 4x4 matrix can be decoupled into two 2x2 matrices. However when $k_H \neq 0$, $\psi_{\mu\sigma}^{N,k_H,k_y}$ must be expressed by the linear combinations of the band edge Bloch states with different N, and it is the $k_H \neq 0$ case that is important for the SdH effect. In addition, the coefficients $A^N_{\mu\sigma,\mu'\sigma'}$, which are important for the spin-flip scattering transition, are non-zero only when $k_H \neq 0$. Thus when $k_H \neq 0$, above matrix has eigenvector of the following form:

$$\begin{pmatrix} LC[\ \phi_{N-1}\ \psi_{\mu\sigma}^T] \\ LC[\ \phi_N\ \psi_{\mu\sigma}^T\ ] \\ LC[\ \phi_N\ \psi_{\mu\sigma}^T\ ] \\ LC[\ \phi_{N-1}\ \psi_{\mu\sigma}^T] \end{pmatrix},$$

where LC[$\phi_N \psi^T_{\mu\sigma}$] means the linear combination of harmonic oscillator function (order N) times $\psi^T_{\mu\sigma}$ for all the combinations of μ and σ. Thus, the conduction band wave functions are given by the following equations:

$$\psi^{N,k_H,k_y}_{c\uparrow} = |\, N,\vec{k},C\uparrow \,>$$

$$= e^{i(\,\eta k_H z + k_y y\,)}[\, A^N_{c\uparrow,c\uparrow}\phi_N\psi^T_{c\uparrow} + A^N_{c\uparrow,c\downarrow}\phi_{N+1}\psi^T_{c\downarrow} + A^N_{c\uparrow,v\uparrow}\phi_N\psi^T_{v\uparrow} + A^N_{c\uparrow,v\downarrow}\phi_{N+1}\psi^T_{v\downarrow}\,], \quad (\text{D.3,a})$$

$$\psi^{N,k_H,k_y}_{c\downarrow} = |\, N,\vec{k},C\downarrow \,>$$

$$= e^{i(\,\eta k_H z + k_y y\,)}[\, A^N_{c\downarrow,c\uparrow}\phi_{N-1}\psi^T_{c\uparrow} + A^N_{c\downarrow,c\downarrow}\phi_N\psi^T_{c\downarrow} + A^N_{c\downarrow,v\uparrow}\phi_{N-1}\psi^T_{v\uparrow} + A^N_{c\downarrow,v\downarrow}\phi_N\psi^T_{v\downarrow}\,]. \quad (\text{D.3,b})$$

In eq.(D.3,a), $A^N_{c\uparrow,c\downarrow}$ and $A^N_{c\uparrow,v\uparrow}$ are zero, when k_H=0, and in eq.(D.3,b), $A^N_{c\downarrow,c\uparrow}$ and $A^N_{c\downarrow,v\downarrow}$ are zero, when k_H=0, and these coefficients play important roles in the spin-flip scattering.

Appendix E

For the scattering by impurity potential

$$U(\vec{r}) = \sum_j u(\vec{r}-\vec{r}_j),$$

the transition probability in the Born approximation is

$$\frac{2\pi}{\hbar} < |< N',k',\mu'\sigma'|U(\vec{r})|N,k,\mu\sigma >|^2 >_s \delta(E_{N'k'\mu'\sigma'} - E_{Nk\mu\sigma}),$$

where $<--->_s$ denotes the average with respect to the scatterer's variables. When impurities are assumed to be distributed homogeneously in the crystal, above matrix element becomes,

$$< |< N'k'\mu'\sigma'|U|Nk\mu\sigma >|^2 >_s = \frac{n_i}{\Omega} \sum_{\vec{q}} |V(\vec{q})|^2 |< N'k'\mu'\sigma'|e^{i\vec{q}\cdot\vec{r}}|Nk\mu\sigma >|^2,$$

where n_i is the concentration of the scatterer, Ω is the volume of the crystal, and

$$V(\vec{q}) = \int u(\vec{r})\ e^{-i\vec{q}\cdot\vec{r}} d\vec{r}/\sqrt{\Omega}$$

is the Fourier transform of the scattering potential, and

$$U(\vec{r}) = \sum_{j\vec{q}}\sum V(\vec{q})\ e^{i\vec{q}\cdot(\vec{r}-\vec{r}_j)}/\sqrt{\Omega} .$$

If the impurity potential is approximated by δ-function, that is,

$$u(\vec{r}-\vec{r}_j) = a\delta(\vec{r}-\vec{r}_j),$$

where a is the strength of the δ-function, and in this case

$$V(\vec{q}) = a .$$

Using eqs.(D.3,a) and (D.3,b), the transition probability can be calculated. Thus,

$$< N'k'C'\sigma'|U|NkC\sigma >$$

$$= \frac{an_i}{\Omega} \sum_{\vec{q}} \sum_{\substack{\mu''\sigma'' \\ \mu'''\sigma'''}} \int_{\text{crystal}} e^{-i(K_y'y+k_z'z)} \phi_{N'+\sigma'-\sigma''} A^{N^*}_{c\sigma',\mu''\sigma''} \psi^{T^*}_{\mu''\sigma''} e^{i\vec{q}\cdot\vec{r}}\ e^{i(K_y''y+k_z''z)}$$

$$\times\ \phi_{N+\sigma-\sigma'''} A^{N}_{c\sigma,\mu'''\sigma'''} \psi^{T}_{\mu'''\sigma'''} d\vec{r} \quad ,$$

where $K_y = \eta k_y$. In the above equation, the integration over cell periodic part can be calculated independently, if the impurity potential is a slowly varing function over a unit cell. In this case, the integral can be broken into two parts and one of the term becomes,

$$\sum_{\vec{q}} \delta(K_y'-q_y-K_y)\, \delta(k_z'-q_z-k_z)\, J_{N'N}\,(q_x,K_y',K_y) \int_{\text{cell}} \psi^{T*}_{c\sigma''}\psi^{T}_{c\sigma}\, d\vec{r}\ , \qquad (\text{E.1})$$

where

$$J_{N'N}(q_x,K_y',K_y) = \int_{-\infty}^{\infty} \phi_N\,(x + 1^2K_y')\, e^{iq_xx}\, \phi_N(x+1^2K_y)\, dx\ ,$$

and $1^2K_y = \hbar K_y/m\omega_c$.

According to Argyres,$^{9)}$

$$\iint_{-\infty}^{\infty} |J_{N'N}(\pm q_x,\pm q_y+K_y,K_y)|^2\, dq_xdq_y = 2\pi/1^2\ . \qquad (\text{E.2})$$

In eq. (E.1), we can substitute $\sum_{\vec{q}}$ by integral, thus letting $K_y' = K_y + q_y$ in eq. (E.2), we have,

$$\sum_{\vec{q}} \delta(K_y'-q_y-K_y)\, \delta(k_z'-q_z-k_z)|\, J_{N'N}(q_x,q_y+K_y,k_z)\ |^2 |\int_{\text{cell}} \psi^{T*}_{\mu'\sigma''}\psi^{T}_{\mu\sigma}\ d\vec{r}|^2$$

$$= \frac{\Omega}{8\pi^3} \int_{-\infty}^{\infty} dq_z\delta(k_z'-q_z-k_z) \iint_{-\infty}^{\infty} dq_xdq_y|\ J_{N'N}(q_x,q_y+K_y,K_y)\ |^2\ \delta_{\mu'\sigma''}\, \delta_{\mu\sigma}$$

$$= \frac{\Omega}{8\pi^3}\ \delta_{k_z'k_z}\frac{2\pi}{1^2}\, \delta_{\mu'\sigma'',\mu\sigma}\ . \qquad (\text{E.3})$$

Thus the scattering transitions can occur from state N to arbitrary N′ states unless the cell periodic parts are not equal to zero.

References

1) L. Shubnikov and W. J. de Haas: Leiden Commun. 207a,c,d,210a (1930)

2) W. J. de Haas and P. M. van Alphen: Leiden Commun. 208d, 212a (1930) and 220d (1933)

3) L. D. Landau: Z. Physik. 64, 629 (1930)

4) R. Peierls: Z. Physik. 80, 763 (1933)

5) S. Titeica: Ann. Physik. 22, 129 (1933)

6) B. Davydov and I. Pomeranchuk: J. Phys. USSR 2, 147 (1940)

7) G. E. Zil'ber: Soviet Phys. JETP 2, 650 (1955)

8) I. M. Lifshitz: J. Phys. Chem. Solids 4, 11 (1958)

9) P. N. Argyres: J. Phys. Chem. Solids 4, 19 (1958); Phys. Rev. 109, 1115 (1958)

10) P. N. Argyres and L. M. Roth: J. Phys. Chem. Solids 12, 89 (1959)

11) R. Kubo, H. Hasegawa, and N. Hashitsume: Phys. Rev. Letters 1, 279 (1958); J. Phys. Soc. Japan 14, 56 (1959)

12) E. N. Adams and T. D. Holstein: J. Phys. Chem. Solids 10, 254 (1959)

13) A. H. Kahn and H. P. R. Frederikse: Solid State Physics, edited by F. Seitz and D. Turnbull (Academic Press, New York, 1959), Vol.9, p.257

14) Y. Kanai and W. Sasaki: J. Phys. Soc. Japan 11, 1017 (1956)

15) H. P. R. Frederikse and W. R. Hosler: Phys. Rev. 110, 880 (1958)

16) R. J. Sladek: Phys. Rev. 110, 817 (1958)

17) H. P. R. Frederikse and W. R. Hosler: Phys. Rev. 110, 880 (1958)

18) R. W. Stark: Phys. Rev. 135, A1698 (1964)

19) S. Askénazy, J. Léotin, J-P. Ulmet: Solid State Commun. 7, 1355 (1969)

20) E. D. Hinkley and A. W. Ewald: Phys. Rev. 134, A1261 (1964)

21) C. R. Whitsett: Phys. Rev. 138, A 829 (1965)

22) R. A. Stradling and G. A. Antcliffe: Proc. Int. Conf. Physics of Semiconductors, Kyoto (1966); J. Phys. Soc. Japan Suppl. 21, 374 (1966)

23) M. Yamamoto and T. Fukuroi, J. Phys. Soc. Japan 21, 2428 (1966)

24) S. H. Groves, R. N. Brown, and C. R. Pidgeon: Phys. Rev. 161, 779 (1967)

25) M. Yamamoto: J. Phys. Soc. Japan 24, 73 (1968)

26) W. Giriat: Proc. Int. Conf. of II-VI Semicon. Compounds, (1967) p.1058; Phys. Letters 24A, 515 (1967)

27) L. M. Falicov and R. W. Stark: Prog. LT. Phys. 5, 235 (1967)

28) R. B. Dingle: Proc. Roy. Soc. A211, 517 (1952)

29) Kh. I. Amirkhanov, R. I. Bashirov, and Yu. Ė. Zakiev: Soviet Phys.-Solid State 5, 340 (1963)

30) M. S. Bresler, R. V. Parfenėv, and S. S. Shalyt: Soviet Phys.-Solid State 7, 1025 (1965)

31) S. T. Pavlov, R. V. Parfenėv, Yu. A. Firsov, and S. S. Shalyt: Soviet Phys.-JETP. 21, 1049 (1965)

32) L. M. Bliek, G. Landwehr, and M. V. Ortenberg: Proc. Int. Conf. Physics of Semiconductors, Moscow (1968) p.710

33) I. M. Tsidil'kovskii and A. I. Ponomarev: Proc. Int. Conf. of II-VI Semicon. Compounds, (1967) p.1103

34) A. I. Ponomarev and I. M. Tsidil'kovskii: Soviet Phys.-Semiconductors 1, 1375 (1968)

35) G. A. Antcliffe and R. A. Stradling: Phys. Letters 20, 119 (1966)

36) Kh. I. Amirkhanov and R. I. Bashirov: Soviet Phys.-Solid State 8, 1739 (1967)

37) K. Suizu and S. Narita: Solid State Commun. 10, 627 (1972); Phys. Letters 43A, 353 (1973)

38) J. R. Burke, B. Houston, and H. T. Savage: Phys. Rev. B2, 1977 (1970)

39) I. Melngailis, T. C. Harman, J. G. Mavroides, and J. O. Dimmock: Phys. Rev. B3, 370 (1971)

40) S. Narita and Y. Takafuji: Solid State Commun. 20, 357 (1976)

41) L. Ė. Gurevich and A. L. Ėfros: Soviet Phys.-JETP. 16, 402 (1963)

42) A. L. Ėfros: Soviet Phys.-Solid State 7, 1206 (1965)

43) S. Narita and K. Suizu: Progr. Theor. Phys. Suppl. 57, 187 (1975)

44) J. O. Dimmock, I. Melngailis, and A. J. Strauss: Phys. Rev. Letters 16, 1193 (1966)

45) J. F. Butler: Solid State Commun. 7, 909 (1969)

46) A. R. Calawa, J. O. Dimmock, T. C. Harman, and I. Melngailis: Phys. Rev. Letters 23, 7 (1969)

47) T. C. Harman: Proc. Conf. Physics of Semimetals and Narrow Gap Semiconductors, edited by D. L. Carter and R. T. Bate (Pergamon Press, New York, 1970), p.363

48) I. Melngailis and T. C. Harman, Semiconductors and Semimetals, edited by R. K. Willardson and A. C. Beer (Academic Press, New York, 1970) Vol.5, p.111

49) H. Kawamura, S. Takano, S. Hotta, S. Nishi, Y. Kato, K.L.I. Kobayashi, and K.F. Komatsubara: Proc. Int. Conf. Physics of Semiconductors, Stuttgart (1974) p.551

50) H. Kawamura, K. Murase, S. Nishikawa, S. Nishi, and S. Katayama: Solid State Commun. 17, 55 (1975)

51) Y. Kanai, and K. Shohno: Japan. J. Appl. Phys. 2, 6 (1963)

52) J. R. Dixson and R. F. Bis: Phys. Rev. 176, 942 (1968)

53) To be published

54) P.J. Stiles, E. Burstein, and D.N. Langenberg: Phys. Rev. Letters 6, 667 (1961); J. Appl. Phys. Suppl. 32, 2174 (1961)

55) K.F. Cuff, M.R. Ellett, C.D. Kuglin, and L.R. Williams: Proc. Int. Conf. Phys. Semiconductors, Exeter (1962) p.316; Proc. Int. Conf. Semiconductors, Paris (1964) p.677

56) P. J. Stiles, E. Burstein and D. N. Langenberg: Proc. Int. Conf. Phys. Semiconductors, Exeter (1962) p.577; Phys. Rev. Letters 9 257 (1962)

57) R. Nii: J. Phys. Soc. Japan 18, 456 (1963); ibid. 19, 58 (1964)

58) W. Shilz: J. Phys. Chem. Solids 30, 893 (1969)

59) T. E. Thompson, P. R. Aron, B. S. Chandrasekhar, and D. N. Langenberg: Proc. Conf. Physics of Semimetals and Narrow Gap Semiconductors, edited by D. L. Carter and R. T. Bate (Pergamon Press, New York, 1970), p.331; Phys. Rev. B4, 518 (1971)

60) C. K. N. Patel and R. E. Slusher: Phys. Rev. 177, 1200 (1969)

61) J. F. Butler and A. R. Calawa: Phys. Quantum Electronics, edited by P. L. Kelley, B. Lax, and P. E. Tannenwald (McGraw-Hill, New York, 1966), p.458

62) R. Burke, J. D. Jensen, and B. Houston: Proc. Conf. Physics of Semimetals and Narrow Gap Semiconductors, edited by D. L. Carter and R. T. Bate (Pergamon Press, New York, 1970), p.393

63) I. Melngailis, J. A. Kaflas, and T. C. Harmen: Proc. Conf. Physics of Semimetals and Narrow Gap Semiconductors, edited by D. L. Carter and R. T. Bate (Pergamon Press, New York, 1970), p.407

64) B. Ellis and T. S. Moss: Proc. 3rd. Photocon. Conf. (1967) p.211

65) R. A. Stradling: Int. Conf. Appl. of High Magnetic Fields in Semiconductor Physics, Würzburg (1974) P.257; Proc. Int. Conf. Physics of Semiconductors, Cardiff (1974) p.531

66) J. R. Burke,Jr., B. Houston, H. T. Savage, J. Babiskin, and P. G. Siebenmann: Proc. Int. Conf. Physics of Semiconductors, Kyoto, (1966) [J. Phys. Soc. Japan Suppl. 21, 384 (1966)]; Phys. Rev. Letters 14, 360 (1965)

67) H. T. Savage , B. Houston, and J. R. Burke,Jr.: Phys. Rev. B6, 2292 (1972)

68) J. O. Dimmock and G. B. Wright: Proc. Int. Conf. Physics of Semiconductors, Paris (1964) p.77; Phys. Rev. 135A, 821 (1964)

69) R. Tsu, W. E. Haward, and L. Esaki: Phys. Rev. 172,779 (1968)

70) S. D. Senturia, A. C. Smith, C. R. Hewes, M. S. Adler, J. A. Hofmann, and D. L. Sagalyn: Proc. Conf. Physics of Semimetals and Narrow Gap Semiconductors, edited by D. L. Carter and R. T. Bate (Pergamon Press, New York, 1970), p.333

71) M. S. Adler, C. R. Hewes, and S. D. Senturia: Phys. Rev. B7, 5195 (1973)

72) M. Iizumi, Y. Hamaguchi, K. F. Komatsubara, and Y. Kato: J. Phys. Soc. Japan 38, 443 (1975); Proc. Conf, Physics of Semiconductors, Stuttgart (1974) p.602

73) S. Katayama: Solid State Commun. 19, 381 (1976)

74) S. Watarai and T. Matsubara: Prog. Theor. Phys. 53, 1214 (1975)

75) A. Natori: J. Phys. Soc. Japan 40, 163 (1976)

76) V. L. Volkov, V. I. Litvinov, V. M. Baginskii, and K. D. Tovstyuk: Solid State Commun. 20, 807 (1976)

77) J. B. Conklin, Jr., L. E. Johnson, and G. W. Pratt, Jr.: Phys. Rev. 137, A1282 (1965)

78) F. Herman, R. L. Kortum, I. B. Ortenburger, and J-P. Van Dyke: Jour. de Phys. [Suppl. N^0 11-12] 29, C4-62 (1968)

79) R. L. Bernick and L. Kleinman: Solid State Commun. 8, 569 (1970)

80) Y. W. Tsang and M. L. Cohen: Phys. Rev. 180, 823 (1969); Phys. Rev. Letters 29A, 236 (1969)

81) M. L. Cohen and Y. W. Tsang: Proc. Conf. Physics of Semimetals and Narrow Gap Semiconductors, edited by D. L. Carter and R. T. Bate (Pergamon Press, New York, 1970), p.303

82) H. Overhof and U. Rössler: Phys. Stat. Solidi 37, 691 (1970)

83) D. L. Mitchell and R. F. Wallis: Phys. Rev. 151, 581 (1966)

84) J. O. Dimmock: Proc. Conf. Physics of Semimetals and Narrow Gap Semiconductors, edited by D. L. Carter and R. T. Bate (Pergamon Press, New York, 1970),p.319

85) M. S. Adler, C. R. Hewes, and S. D. Senturia: Phys. Rev. B7, 5186 (1973)

86) I. Melngailis: Jour. de Phys. [Suppl. N^0 11-12] 29, C4-84 (1968)

87) L. Onsager: Phil. Mag. 43, 1006 (1952)

88) L. M. Roth and P. N. Argyres: Semiconductors and Semimetals, edited by R. K. Willardson and A. C. Beer (Academic Press, New York, 1966), Vol.1, p.159

89) R. Courant and D. Hilbert: Method of Mathematical Physics, (Wiley, New York, 1953), Vol.1, p.77

90) T. C. Harman: J. Nonmetals 1, 183 (1973)

91) J. W. Wagner and R. K. Willardson: Trans. AIME 242, 366 (1968)

92) J. F. Butler and T. C. Harman: Appl. Phys. Letters 12, 347 (1968)

93) A. R. Calawa, T. C. Harman, M. Finn, and P. Youtz: Trans. AIME 242, 374 (1968)

94) J. Bloem: Philips Res. Rept. 11, 273 (1956); J. Bloem and F.A.Kroger: Z. Physik Chem. 7, 1 (1956)

95) N. Ohashi and K. Igaki: Trans. Japan. Instit. Metals 5, 94 (1964)

96) R. F. Brebrick and E. Gubner: J. Chem. Phys. 36, 1283 (1962)

97) G. A. Antcliffe: Phys. Rev. B2, 345 (1970)

98) R. I. Bashirov, R. M. Gadzhieva, and E. M. Khanzhina: Soviet Phys.-Semiconductors 2, 840 (1969)

99) J. S. Dhillon and D. Shoenberg: Phil. Trans. A248, 1 (1955)

100) M. H. Cohen and E. I. Blount: Phil. Mag. 5, 115 (1960)

101) J. M. Luttinger and W. Kohn: Phys. Rev. 97, 869 (1955)

102) G. W. Pratt, Jr., and L. G. Ferreira: Proc. Int. Conf. Physics of Semiconductors, Paris (1964) p.69

103) A. S. Saleh and H. Y. Fan: Phys. Rev. B5, 3972 (1972)

104) S. Nishikawa, K. Murase, and H. Kawamura: 31st. meeting of the Physical Society of Japan, April. (1976)

105) D. V. Mashovets, R. V. Parfen'ev, and V. S. Vekshina: Soviet Phys.-Solid State 10, 2700 (1969)

106) R. Glosser, J. Kinoshita, and B. Rennex: Phys. Rev. Letters 33, 1027 (1974)

107) R. Kubo, S. J. Miyake, and N. Hashitsume: Solid State Physics, edited by F. Seitz and D. Turnbull (Academic Press, New York, 1965), Vol.17, p.269